



Defense Threat Reduction Agency
8725 John J. Kingman Road, MS
6201 Fort Belvoir, VA 22060-6201



DTRA-TR-13-7

TECHNICAL REPORT

Control of Grain Boundaries and Defects in Nano-Engineered Transparent Scintillator Ceramics

Approved for public release; distribution is unlimited.

March 2013

HDTRA1-07-1-0009

R.S. Feigelson et al.

Prepared by:
Geballe Laboratory for
Advanced Materials
476 Lomita Mall
Stanford University
Stanford, CA 94305

DESTRUCTION NOTICE:

Destroy this report when it is no longer needed.
Do not return to sender.

PLEASE NOTIFY THE DEFENSE THREAT REDUCTION
AGENCY, ATTN: DTRIAC/ J-3 ONIUI , 8725 JOHN J. KINGMAN ROAD,
MS-6201, FT BELVOIR, VA 22060-6201, IF YOUR ADDRESS
IS INCORRECT, IF YOU WISH THAT IT BE DELETED FROM THE
DISTRIBUTION LIST, OR IF THE ADDRESSEE IS NO
LONGER EMPLOYED BY YOUR ORGANIZATION.

REPORT DOCUMENTATION PAGE				Form Approved OMB No. 0704-0188	
Public reporting burden for this collection of information is estimated to average 1 hour per response, including the time for reviewing instructions, searching existing data sources, gathering and maintaining the data needed, and completing and reviewing this collection of information. Send comments regarding this burden estimate or any other aspect of this collection of information, including suggestions for reducing this burden to Department of Defense, Washington Headquarters Services, Directorate for Information Operations and Reports (0704-0188), 1215 Jefferson Davis Highway, Suite 1204, Arlington, VA 22202-4302. Respondents should be aware that notwithstanding any other provision of law, no person shall be subject to any penalty for failing to comply with a collection of information if it does not display a currently valid OMB control number. PLEASE DO NOT RETURN YOUR FORM TO THE ABOVE ADDRESS.					
1. REPORT DATE (DD-MM-YYYY) 00-03-2013		2. REPORT TYPE Technical		3. DATES COVERED (From - To) 11/15/06-3/14/12	
4. TITLE AND SUBTITLE Control of Grain Boundaries and Defects in Nano-Engineered Transparent Scintillator Ceramics				5a. CONTRACT NUMBER	
				5b. GRANT NUMBER HDTRA1-07-1-0009	
				5c. PROGRAM ELEMENT NUMBER	
6. AUTHOR(S) R.S. Feigelson (P.I.), R. Gaume, and S.R. Podowitz				5d. PROJECT NUMBER	
				5e. TASK NUMBER	
				5f. WORK UNIT NUMBER	
7. PERFORMING ORGANIZATION NAME(S) AND ADDRESS(ES) Geballe Laboratory for Advanced Materials 476 Lomita Mall Stanford University Stanford, CA 94305-4088				8. PERFORMING ORGANIZATION REPORT NUMBER	
9. SPONSORING / MONITORING AGENCY NAME(S) AND ADDRESS(ES) Defense Threat Reduction Agency 8725 John J. Kingman Rd. Fort Belvoir, VA 22060 PM/D. Petersen				10. SPONSOR/MONITOR'S ACRONYM(S) DTRA	
				11. SPONSOR/MONITOR'S REPORT NUMBER(S) DTRA-TR-13-7	
12. DISTRIBUTION / AVAILABILITY STATEMENT Approved for public release; distribution is unlimited.					
13. SUPPLEMENTARY NOTES					
14. ABSTRACT This research program focused mainly on the relationship between macro-scale defects on the scintillator properties of optical ceramics. The former includes grain boundaries, porosity and solid phase inclusions, and the latter, lattice imperfections. The following important results were found: 1) Oxygen defects in hot pressed Eu-doped yttrium oxide ceramics dwarf the influence of grain boundary defects on scintillator light yield (5 to 250 micron grain size range). A direct relationship was found between the in-diffusion of oxygen during annealing and the decrease in the number of charge carrier traps. This oxygen up-take resulted in an increased in light yield. 2) Two novel micro-scale scintillation characterization techniques were developed. 3) Grain boundary recombination in Eu-doped yttrium oxide ceramics (grain sizes>~30 microns) was found to be minimal. Transmission electron microscopy showed that these ceramics had abrupt boundaries, 4) In vacuum sintered Ce-doped yttrium aluminum garnet ceramics, a relationship was found between cation non-stoichiometry, anti-site defects, and light yield. 5) in translucent Eu-doped strontium iodide ceramics produced by hot pressing, a relationship between transparency, grain texture and scintillation properties was identified.					
15. SUBJECT TERMS Inorganic scintillator, transparent ceramics, grain-boundary, defects, microstructure, europium, cerium, yttrium oxide					
16. SECURITY CLASSIFICATION OF:			17. LIMITATION OF ABSTRACT UU	18. NUMBER OF PAGES 127	19a. NAME OF RESPONSIBLE PERSON David Petersen
a. REPORT Unclassified	b. ABSTRACT Unclassified	c. THIS PAGE Unclassified			19b. TELEPHONE NUMBER (include area code) 703-767-3164

CONVERSION TABLE

Conversion Factors for U.S. Customary to metric (SI) units of measurement.

MULTIPLY → BY → TO GET
TO GET ← BY ← DIVIDE

angstrom	1.000 000 x E -10	meters (m)
atmosphere (normal)	1.013 25 x E +2	kilo pascal (kPa)
bar	1.000 000 x E +2	kilo pascal (kPa)
barn	1.000 000 x E -28	meter ² (m ²)
British thermal unit (thermochemical)	1.054 350 x E +3	joule (J)
calorie (thermochemical)	4.184 000	joule (J)
cal (thermochemical/cm ²)	4.184 000 x E -2	mega joule/m ² (MJ/m ²)
curie	3.700 000 x E +1	*giga bacquerel (GBq)
degree (angle)	1.745 329 x E -2	radian (rad)
degree Fahrenheit	$t_k = (t^{\circ}f + 459.67)/1.8$	degree kelvin (K)
electron volt	1.602 19 x E -19	joule (J)
erg	1.000 000 x E -7	joule (J)
erg/second	1.000 000 x E -7	watt (W)
foot	3.048 000 x E -1	meter (m)
foot-pound-force	1.355 818	joule (J)
gallon (U.S. liquid)	3.785 412 x E -3	meter ³ (m ³)
inch	2.540 000 x E -2	meter (m)
jerk	1.000 000 x E +9	joule (J)
joule/kilogram (J/kg) radiation dose absorbed	1.000 000	Gray (Gy)
kilotons	4.183	terajoules
kip (1000 lbf)	4.448 222 x E +3	newton (N)
kip/inch ² (ksi)	6.894 757 x E +3	kilo pascal (kPa)
ktap	1.000 000 x E +2	newton-second/m ² (N-s/m ²)
micron	1.000 000 x E -6	meter (m)
mil	2.540 000 x E -5	meter (m)
mile (international)	1.609 344 x E +3	meter (m)
ounce	2.834 952 x E -2	kilogram (kg)
pound-force (lbs avoirdupois)	4.448 222	newton (N)
pound-force inch	1.129 848 x E -1	newton-meter (N-m)
pound-force/inch	1.751 268 x E +2	newton/meter (N/m)
pound-force/foot ²	4.788 026 x E -2	kilo pascal (kPa)
pound-force/inch ² (psi)	6.894 757	kilo pascal (kPa)
pound-mass (lbm avoirdupois)	4.535 924 x E -1	kilogram (kg)
pound-mass-foot ² (moment of inertia)	4.214 011 x E -2	kilogram-meter ² (kg-m ²)
pound-mass/foot ³	1.601 846 x E +1	kilogram-meter ³ (kg/m ³)
rad (radiation dose absorbed)	1.000 000 x E -2	**Gray (Gy)
roentgen	2.579 760 x E -4	coulomb/kilogram (C/kg)
shake	1.000 000 x E -8	second (s)
slug	1.459 390 x E +1	kilogram (kg)
torr (mm Hg, 0° C)	1.333 22 x E -1	kilo pascal (kPa)

*The bacquerel (Bq) is the SI unit of radioactivity; 1 Bq = 1 event/s.

**The Gray (GY) is the SI unit of absorbed radiation.

TABLE OF CONTENTS

1. Executive Summary	4
2. Introduction	10
3. Technical Approach	14
4. Scientific Results	17
4.1. <i>Eu:Y₂O₃ Ceramics: Sintering to High Optical Transparency and Optimizing Scintillation vs. Grain Size and Processing Parameters</i>	17
4.2 <i>Micro-scale Scintillation Characterization Across Grain Boundaries in Ceramic Scintillators</i>	55
4.3. <i>Eu:(Gd,Lu)₂O₃ Transparent Ceramic Sintering</i>	71
4.4. <i>Ce-doped Alkaline Earth and Rare Earth Hafnates Ceramics Sintering and Scintillation Properties</i>	77
4.5. <i>Ce:Y₃Al₅O₁₂ (Ce:YAG) Ceramics: Sintering and Effect of Cation Non-Stoichiometry on Scintillation in Ce:YAG Transparent Ceramics</i>	92
4.6. <i>SrI₂ and Eu:SrI₂ Ceramics: Effect of Grain Texturing on Optical Transmission in Translucent SrI₂ and Eu:SrI₂ Ceramics and Scintillation Properties</i>	97
5. Deliverables	
5.1. <i>DTRA annual reports</i>	110
5.2. <i>Refereed journal publications</i>	110
5.3. <i>Inventions</i>	110
5.4. <i>Theses</i>	110
5.5. <i>Presentations</i>	111
6. Personnel Supported	113
7. Interactions/Transitions	113
8. Honors/Awards	114
9. Quad Chart	115
10. References	116

1. Executive Summary

Introduction

The need for high efficiency and low cost materials for such detector systems is a primary concern for the practical deployment of large-scale equipment throughout the country and elsewhere. Most materials of relevance for these applications have been made from single crystals. These are generally expensive to prepare and have problems with size, uniformity and activator ion concentration. Recently, attention in the detector community has been drawn towards the area of optical ceramics-ceramic materials that are highly transparent and have been under study for high-power laser applications. These materials do not undergo component segregation during processing as do single crystals, and can, in general, be more heavily doped, produced in near-net shapes and scaled up to large sizes more readily than single crystal components.

Program Objectives

This research program involved the use of several model material systems and had the following goals: 1. Study the effect of ceramic microstructure and defects, such as grain boundaries, and pores on the conversion-migration-recombination processes involved in the scintillation mechanism. 2. Developing an understanding and control of the lattice and grain boundary defects generated by ceramic sintering additives. 3. Develop a quantitative relationship between processing parameters, defect structure, and scintillation performance in transparent ceramics. 4. Demonstrate improved scintillator performance with control of ceramic microstructure and composition.

The first phase of our investigations involved a relatively simple binary compound $\text{Eu:Y}_2\text{O}_3$. We developed procedures for preparing highly transparent ceramic samples and studied the relationship between processing conditions, transparency and some scintillator properties. We also looked at the role of rare-earth dopant sintering aids on Y_2O_3 densification and the effect of grain size and oxygen non-stoichiometry on the scintillation properties of $\text{Eu:Y}_2\text{O}_3$.

In the second phase of this program, we prepared transparent ceramics of more complex scintillator materials (ternary oxide compounds containing two cations) i.e. Ce:BaHfO_3 , Ce:SrHfO_3 , $\text{Ce:La}_2\text{Hf}_2\text{O}_7$, $\text{Ce:Lu}_2\text{Hf}_2\text{O}_7$ and $\text{Ce:Y}_3\text{Al}_5\text{O}_{12}$ (YAG). Some of their scintillator properties were measured. Most of the hafnates, cubic and non-cubic, lacked attractive properties in spite of literature reports to the contrary and so we shifted our efforts to the more interesting cubic compound Ce:YAG , which became a model system for studying the effect of oxygen and cation non-stoichiometry on scintillation performance.

During the last phase of our program we studied methods for preparing transparent ceramics of SrI_2 , a new and exciting scintillator material with a non-cubic structure and a light yield of $\sim 100,000$ photons/MeV, when doped with Eu, and excellent energy resolution [1,2]. We developed techniques for producing highly translucent SrI_2 , determined the role of Grain Texturing on Optical Transmission and measured its scintillation properties as a function of processing conditions. During this period we also developed (using $\text{Eu:Y}_2\text{O}_3$ and Ce:YAG ceramics), an important new technique for probing scintillation properties on a micro-scale to determine scintillation emission losses at and near grain boundaries.

Major Accomplishments

1. Convincing evidence was found that processing conditions strongly affect the light yield of highly transparent $\text{Eu:Y}_2\text{O}_3$ and Ce:YAG scintillator ceramics due to both cation and oxygen stoichiometry. However, unlike initial expectations, above a minimum grain size, the grain boundaries had a limited effect on light yield (in hot-pressed $\text{Eu:Y}_2\text{O}_3$ samples). These findings showed that the processing conditions that lead to optimized transparency were not necessarily those conditions that optimized light yield. Although a relationship with grain size was observed, this dependence originated from the in-diffusion of oxygen through grain boundaries and into grains, decreasing the concentration of deep charge carrier traps. Therefore, extensive processing studies on scintillator ceramics must not only focus on maximizing optical transparency, as is often the case, but be aimed at understanding the relationship between processing and defect chemistry that may lead to charge carrier losses and light absorption. For $\text{Eu:Y}_2\text{O}_3$, it was clearly not sufficient to limit the volumetric concentration of grain boundaries in order to achieve higher levels of radiative recombination.
2. Using highly transparent $\text{Eu:Y}_2\text{O}_3$ and Ce:YAG ceramic materials, it was demonstrated for the first time that X-ray radioluminescence microscopy (XRLM) can be used to directly visualize the scintillation emission near grain boundaries in transparent ceramics (see Figure 1 for schematic of setup and illustration of measurement). When coupled with chemical and structural analysis on the grain boundaries, which in certain cases may be taken simultaneously with XRLM imaging, the XRLM method was found to be a powerful technique that can be used to study the origin of grain boundary effects on bulk luminosity and scintillation. It was also shown that emission profiles measured by this method can be used to calculate charge carrier transport properties in both optoelectronic semiconductors (e.g. GaAs) as well as our inorganic, insulating scintillator materials (e.g. $\text{Eu:Y}_2\text{O}_3$, Ce:YAG).

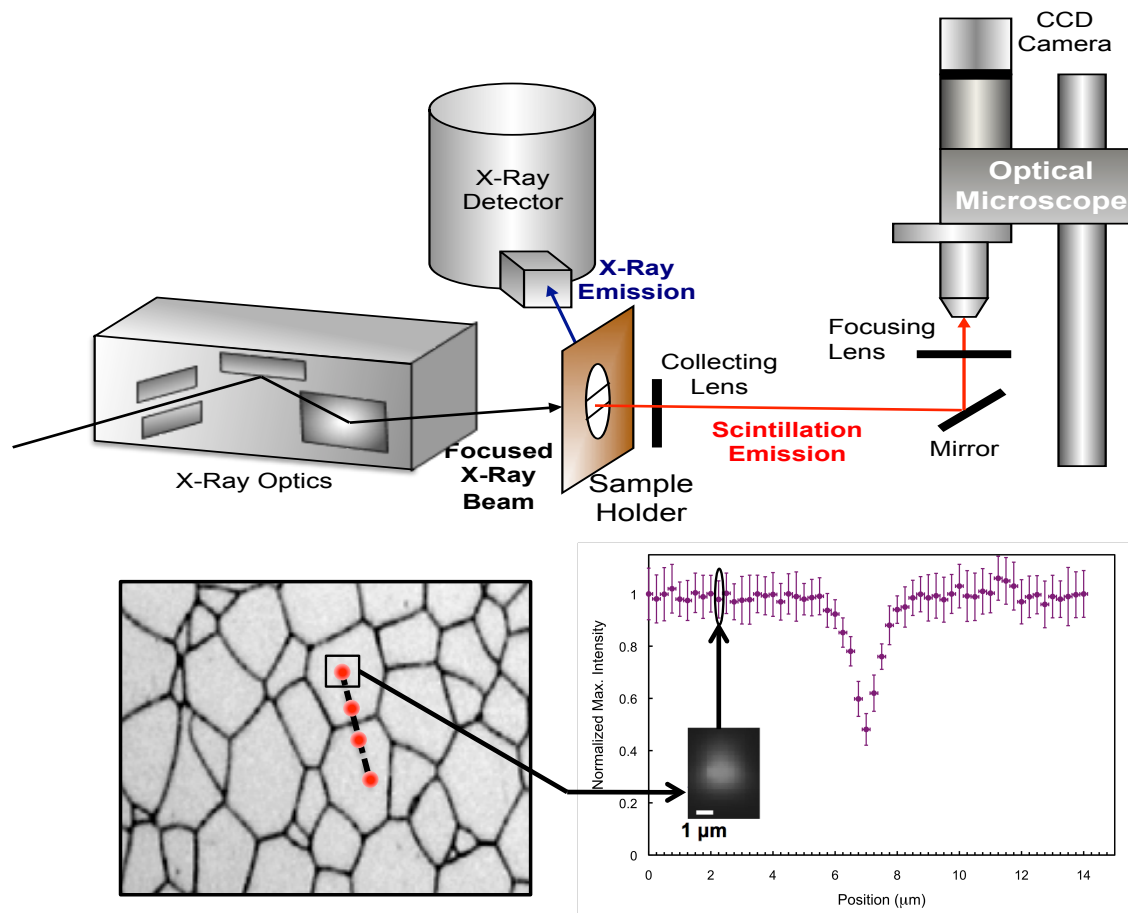


Figure 1: Schematic of XRLM setup and illustration of a measurement in a ceramic scintillator. A typical grain structure is shown, along with the emission from a spot under steady-state, focused X-ray excitation and the XRL intensity from spots measured along a line crossing a grain boundary.

3. Determined that the XRLM method can readily be extended to other luminescent materials, particularly insulators, to characterize the effect of grain boundaries and other structural defects on emission under high-flux X-ray irradiation. Simultaneously coupling XRLM with data from other X-ray analytical techniques, such as X-ray absorption spectroscopy, X-ray microdiffraction, and pulsed X-ray excitation, would make XRLM an even more versatile tool. XRLM may be of particular use for characterizing the effect of chemical segregation and secondary phase formation on scintillation in ceramics of complex garnet solid solutions with promising scintillator properties.
4. Translucent Eu:SrI_2 ceramics were made for the first time by sintering in a hot-press at relatively low temperatures. The optical transmission produced using our most successful sintering procedure was high enough due to grain alignment to produce a photopick with a measured light yield of 25% of

single-crystals and 55% of Tl:NaI. As these ceramics have been shown to be easily textured (grain oriented) during pressure sintering, it may be possible to reach higher levels of grain orientation by pressing under higher pressures, while maintaining the moderate temperatures used in this study. Hence higher light yields might be anticipated for SrI_2 ceramics at reduced costs over single crystal material. This study has also shown the potential for using hot uniaxial pressing to induce texturing in other halide ceramic having fewer slip systems than potassium bromide (KBr), which can be pressed to transparency at room temperature.

Technology Implementation

The results discovered in this research program suggest a number of accessible criteria by which interesting scintillator materials may be evaluated as potential candidates for high-performance ceramic elements in radiation detectors. These include:

1. **Grain boundary defects and their effect on charge carrier trapping and non-radiative recombination.** Evaluating these properties may be aided by XRLM analysis and bulk scintillation characterization techniques coupled with parametric processing studies. Atomistic and first-principles models of grain boundary electronic states also may inform the study of grain boundaries and scintillation performance. Atomistic modeling of grain boundaries in other classes of materials has been used with some success in predicting properties, such as with MgO and HfO_2 [3-6].
2. **Charge carrier diffusion constants within the bulk of the material.** Results from the XRLM studies on $\text{Eu:Y}_2\text{O}_3$ and Ce:YAG suggest that low charge carrier diffusion constants decrease the attenuation of light yield, likely because charge carriers diffuse over a shorter path, and therefore have a higher probability of recombining at a site within the bulk of the grains. XRLM and cathodoluminescence techniques may aid in determine these properties, and thus evaluating if some materials are more sensitive to boundaries than others.
3. **Stoichiometry control throughout ceramic processing.** Parametric ceramic processing studies would provide useful information on the relationship between stoichiometry and scintillator properties and lead to optimization of performance.
4. **Evaluating the degree of birefringence in non-cubic scintillator materials.** Studying available processing routes to induce grain texturing can lead to ceramics with acceptable performance compared with single crystals and at lower cost. In addition to SrI_2 , other scintillator materials recently characterized in powder form, such as $\text{Eu:Ba}_2\text{CsI}_5$ [7], $\text{Eu:Ba}_2\text{CsBr}_5$ [8] and

Eu:BaBrI [9], may be good candidates for transparent ceramic sintering, because of their predicted low birefringence [10].

5. Choosing suitable activator ions or scintillation-promoting dopants.

These can enhance the concentration of the point defects that control the rate of ceramic densification, and lead to enhanced scintillator performance by improving ceramic transparency. While sintering Eu:Y₂O₃ to high levels of transparency, it was found that Eu served both as a sintering aid by controlling the defect chemistry of the system and as an activator ion. It was also found that other rare-earth dopants, including dopants exclusively isovalent to Y³⁺, enhanced densification. Predictive studies on the site preference and the most energetically favorable defect mechanism for dopant incorporation into the host lattices of bixbyite, garnet and perovskite structures [11-15] have been used to understand the preference of the activator ion for particular cation sites in the lattices, which affects the activator ion emission. Similar chemical and bonding energetics information could also be used to understand the effects of rare-earth doping on densification in these materials.

While the above parameters may require more in-depth characterization, they offer a more expansive view of the class of materials that are potentially of interest for transparent ceramic fabrication. The potential for low-cost, large-scale fabrication of scintillator ceramics still make ceramics an attractive alternative to single-crystals, but more extensive studies into the effects of processing parameters on both scintillation and transparency will further inform the development of ceramic bodies with higher levels of scintillator performance and transparency.

Refereed Journal Publications, Theses, and Inventions

Stephen R. Podowitz, Romain Gaume, and Robert S. Feigelson, "Effect of Europium Concentration on Densification of Transparent Eu:Y₂O₃ Scintillator Ceramics using Hot Pressing." *J. Am Ceram. Soc.*, **93** 82-88 (2010).

Stephen R. Podowitz, Romain M. Gaume, Wesley T. Hong, Atlal Laouar, and Robert S. Feigelson. "Fabrication and Properties of Translucent SrI₂ and Eu:SrI₂ Scintillator Ceramics." *IEEE Trans. Nucl. Sci.*, **57** 3827 (2010).

Romain M. Gaume and Lydia M. Joubert. "Airtight Container for the Transfer of Atmosphere Sensitive Materials into Vacuum Operated Characterization Instruments." *Rev. Sci. Instrum.*, **82**[12] 123705 (2011).

Stephen R. Podowitz. Romain M. Gaume, and Robert S. Feigelson. "Probing Grain Boundaries in Ceramic Scintillators using X-Ray Radioluminescence Microscopy." *J. Appl. Phys.*, **111**[1] 013520 (2012).

Stephen R. Podowitz, Stephen M. Hanrahan, Edith Bourret-Courchesne, Nancy C. Giles, Romain M. Gaume, Robert S. Feigelson. "Effect of Grain Boundaries and Oxygen Stoichiometry on Light Yield and Charge Carrier Trapping in Eu:Y₂O₃ Transparent Ceramics" to be submitted shortly to *J. Appl. Phys.*

Patent Disclosure: R. Gaume, *Airtight container for the transfer of atmosphere sensitive materials to characterization instruments*. Stanford University Ref No. 10-327.

Stephen R. Podowitz. *The Effect of Grain Boundaries on Scintillation in Rare-Earth Doped Transparent Ceramics*. Ph.D. Dissertation, Stanford University, Stanford, CA (2011). Full text available at <http://purl.stanford.edu/mc738ct2500>.

Personnel Supported

Dr. Robert S. Feigelson, PI
Dr. Stephen R. Podowitz, Ph.D. Graduate Student
Dr. Romain Gaume, Research Associate
Ye He, Ph.D. Graduate Student
Atlal Laour, M.S. Visiting Graduate Student
Jessica Rabeau, M.S. Visiting Graduate Student
Wesley Hong, Undergraduate Student
Clarissa Gutierrez, Undergraduate Student
Alice Che, Undergraduate Student
Ludwig Galambos, Engineering Technician

2. Introduction

Materials are an important component of radiation detector devices. The need for high efficiency and low cost materials for such detector systems is a primary concern for the practical deployment of large-scale equipment throughout the country and elsewhere. Most materials of relevance for these applications have been made from single crystals. These are generally expensive to prepare and have problems with size, uniformity and activator ion concentration. Recently, attention in the detector community has been drawn towards the area of optical ceramics-ceramic materials that are highly transparent and have been under study for high-power laser applications. These materials do not undergo component segregation during processing as do single crystals, can, in general, be more heavily doped, produced in near-net shapes and scaled up to large sizes more readily than single crystal components.

Scintillator transparency and efficient wall reflectivity are critical issues when spatial resolution and photodiode protection (from direct hits by transmitted neutrons and gamma rays) require material with high thickness-to-width ratio. In a transparent ceramic, like in other scintillator materials (single crystal or glass), a scintillation photon isotropically emitted from a luminescent center, can undergo many interactions before it encounters the output face, which is coupled to a photodetector. For example, internal scattering will increase the path-length and make the material more sensitive to potential radiation traps. This consideration becomes crucial in scintillator geometries where the photon path-length is long and bulky detectors are required.

The transparency of ceramics and their performance in scintillator applications has been limited by a number of factors including crystalline defects, grain boundary effects and index of refraction variations. These include randomly oriented grains, residual porosity and secondary phases. With respect to grain boundaries, they must be kept smaller than $\sim 1/100^{\text{th}}$ of a wavelength to insure that they do not scatter light. The pore density and size distribution must be also kept within demanding limits: a 0.5 cm thick sample with a pore fraction as low as 10 ppm has an attenuation coefficient on the order of 0.2 cm^{-1} . Another important issue is related to index variations caused by local variations in stoichiometry. This can be induced during some powder production procedures. There are also other very specific issues raised by the use of ceramics as scintillator hosts. The scintillation process depends crucially on the local environment of the activator ions in the crystal lattice, as well as the propensity for electrons or holes to become trapped at other defect sites (the latter creating additional levels in the forbidden gap). It has been claimed that even coarse grained transparent ceramics, with grain sizes on the order of a few tens of microns and grain boundary thicknesses of about 2 nm, may generate enough interface related states to modify the average bulk characteristics of charge carrier transport. This eventually degrades the scintillation response and/or overall efficiency parameters. In applications that involve rapid and

repetitive acquisition of imaging data at high framing rates, such as tomographic imaging, afterglow may limit the potential of certain scintillation detectors. If the afterglow does not dissipate in the time available between successive frames, enough of the previous image may remain to cloud the next one being acquired.

Deep and shallow traps in scintillator materials have been identified and are known to be influenced by strains and the proximity to grain boundaries. Partially filled anionic crystal sub-lattices such as the ones encountered in rare-earth oxides with the bixbyite structure preclude the formation of anionic interstitial Frenkel defects that generate deep hole-traps in the bulk (color centers). Surface states at grain boundaries are thought to form shallow traps since they exhibit neither radiation damage nor saturation effects. It may not be necessary to remove all traps to suppress afterglow as it is currently thought sufficient to simply eliminate the deepest ones. Whether this can be done in a controlled manner, either by altering the grain morphology or by introducing differently charged species, needs to be investigated.

While materials with non-cubic crystal structures such as sapphire and spinel have been made into highly translucent ceramics, to date, only cubic phases have been prepared as highly transparent ceramic materials since optical isotropy precludes any refractive index discontinuities at the grain boundaries, thus eliminating light scattering from the randomly oriented individual crystallites. The absence of scattering assures that light emitted in the scintillation process will be transmitted faithfully through the medium to the photo-detector that must ultimately record the signal. The absence of scatter-induced lateral spreading makes it possible, in principle, to achieve greatly improved sharpness and image resolution. As one might expect, very few such materials have been fully developed for practical detection applications. Transparent ceramics of optically isotropic materials such as garnets (ex. $\text{Ce}^{3+}:\text{Y}_3\text{Al}_5\text{O}_{12}$), rare-earth oxides (ex. $\text{Pr}^{3+}:(\text{Gd}_{(1-x)}\text{Y}_x)_2\text{O}_3$), and newer materials such as the alkaline-earth hafnates etc. have recently been demonstrated with some success. However, transparency, even in these cubic materials is not guaranteed because the multi-step ceramic process is complicated. In addition, the fabrication of these ceramics to an optical-grade is not yet reproducible and the mechanisms that prevail in their densification have yet to be fully understood. As a consequence, scintillation performances are still largely process and material dependent.

In the place of hard scientific facts obtained via careful analysis, various mythologies have grown-up concerning what processing parameters are most likely to achieve the highest transparency and hence low optical losses and improved efficiency, light yield and afterglow characteristics. Even after more than 40 years, fabricating an optically transparent ceramic, which is done by removing pores and precipitates, is still a very challenging process.

Since ceramic materials hold great promise to improve the cost and performance of radiation detection devices, it has become increasingly more important that we understand how the various stages in the ceramic processing (such as particle size

and shape, particle packing morphology, interstitial gas removal and grain orientation) contribute to defects within grains and at their boundaries.

Program Objectives

Scintillator ceramics have the potential to be microstructure engineered to produce near-net shapes and scaled-up to large sizes more readily and at lower cost than single crystals. In addition, synthesis processes provide an opportunity to achieve more uniform control of additive concentrations. However, the fabrication of high optical-grade ceramics is not yet reproducible, and the mechanisms that control their densification have yet to be fully understood. Even more important, the role of grain boundaries and other lattice defects on the performance of ceramic scintillators is largely unknown. As a consequence, ceramic scintillator performance is still largely process and material dependent.

This research program involved the use of several model material systems and had the following goals:

1. Study the effect of ceramic microstructure and defects, such as grain boundaries, and pores on the conversion-migration-recombination processes involved in the scintillation mechanism.
2. Developing an understanding and control of the lattice and grain boundary defects generated by ceramic sintering additives.
3. Develop, with the use of model material systems, a quantitative relationship between processing parameters, defect structure, and scintillation performance in transparent ceramics.
4. Demonstrate improved scintillator performance with control of ceramic microstructure and composition.

The following subjects were studied:

A. Binary Cubic Compounds

- I. Development of techniques to prepare transparent $\text{Eu:Y}_2\text{O}_3$ and $\text{Eu:}(\text{Lu}_x\text{Gd}_{1-x})_2\text{O}_3$
- II. Role of rare-earth dopant sintering aids on Y_2O_3 densification
- III. Effect of grain size and oxygen non-stoichiometry on the scintillation properties of $\text{Eu:Y}_2\text{O}_3$

B. Ce-doped Ternary Oxide Compounds

- I. Development of techniques for preparing transparent ceramics of Ce:BaHfO_3 , Ce:SrHfO_3 , $\text{Ce:La}_2\text{Hf}_2\text{O}_7$, $\text{Ce:Lu}_2\text{Hf}_2\text{O}_7$ and $\text{Ce:Y}_3\text{Al}_5\text{O}_{12}$ (YAG)
- II. Scintillation properties measurements of Ce-doped hafnates

- III. Effect of oxygen and cation non-stoichiometry on the scintillation performance of transparent YAG ceramics

C. Micro-scale Scintillation Characterization Across Grain Boundaries in:

- I. Eu:Y₂O₃
- II. Ce:YAG

D. Eu:SrI₂

- I. Development of techniques for preparing of highly translucent SrI₂
- II. Determining the role of grain Texturing on optical transmission
- III. Measurement of the scintillation properties of Eu:SrI₂

3. Technical Approach

Objectives

The basic goal of this program was to study the role of grain boundaries and other lattice defects on the scintillation properties of high density, high optical quality ceramics. Ceramics potentially offer certain cost and other performance benefits over single crystals. The main differences between the two types of materials are the presence of randomly oriented single crystal grains in the ceramic, grain boundaries, residual porosity and a difference in component segregation during sample preparation. The boundaries can lead to optical scattering and act as trapping sites to reduce light yield, decay time, etc. It is therefore very important to learn how these various lattice imperfections, in particular grain boundaries, impact a ceramic's scintillator performance. To successfully carry out this research program it was critical that techniques be developed to prepare ceramic materials with both high optical transparency and measureable scintillator properties. The selection of the model material systems used in this study had to be based on these general criteria. Since transparency in non-cubic phases is affected by birefringence induced light scattering at grain boundaries, we chose to begin our studies with a simple cubic binary compound and then graduate to more complex multi-cation cubic materials and finally a study of both the preparation and properties non-cubic ceramics. As time progressed during this program we became aware of developments on new scintillator materials and in collaboration with various outside groups incorporated these materials into our program.

Ceramic Powder Preparation

Preparing a high density ceramic sample begins with the use of appropriate powders with respect to purity, particle size, distribution, shape, etc. They are sometimes used directly from commercial sources, or chemically prepared in the laboratory. Often grinding or ball milling are used to mix the various component powders such as dopants and/or compound constituents. The powders are then compacted in a cold press (uniaxial or isostatic) to a modest density and then sintered in a furnace by one of a variety of methods. The powders are often analyzed to quantify their physical and chemical properties by x-ray diffraction and various microscopy methods.

In our study of $\text{Eu:Y}_2\text{O}_3$ ceramics we explored 3 different methods of powder synthesis 1) reactive sintering of commercial Eu_2O_3 and Y_2O_3 powders, 2) a core-shell process whereby Eu_2O_3 is precipitated onto Y_2O_3 powder in suspension and 3) chemical co-precipitation of both species. The best results, very adequate for our experimental purposes, were obtained with the first method. XRD analysis was used to gauge the completeness of the reaction and differential thermal analysis was used to determine decomposition and reaction temperatures.

Sintering

There are a variety of methods suitable for preparing dense ceramic materials, but only a few that have been successfully applied to the preparation of optically transparent samples. Two of these, hot pressing and vacuum sintering, were chosen for this program. Coupled with post-sintering processes such as hot isostatic pressing and annealing under stoichiometry altering atmospheres (at various temperatures and soak times), we successfully obtained the high quality samples used in this study.

One of the important methods for inducing high densification rates and greater ceramic transparency is the use of sintering aids. These materials vary depending upon the host lattice and have often been shown to influence the scintillator properties in a negative way. Based on sintering aid mechanisms postulated in the literature, we first looked at the possibility of using the activator ion as the sintering aid, thereby minimizing the effects of foreign species on light yield, decay time, etc.

In this era of nanotechnology, starting powders preparation has become an important topic in the ceramics field. The advantages of working with nano-powders include reduced sintering times and temperatures and the potential for co-doping uniformly during the precipitation process. While this avenue was extensively explored with certain of the materials studied in this program, the use of mixed micron-sized oxide powders from commercial sources was found adequate in most cases for our studies.

Characterization

One of the key components of this study involved varying the defect type and concentration in our model materials and determining their effect on the scintillator properties, particularly light output under gamma irradiation. To accomplish this goal, we used an extensive suite of characterization tools available here at Stanford or in other laboratories. Both macro-scale and micro-scale characterization techniques were used to determine the influence of grain boundaries on light output.

By changing the sintering conditions i.e. temperature, time and/or pressure we were able to manipulate the ceramic microstructure. These processing variables lead to differing grain size, grain boundary geometries, pore size, sample density and to some extent chemical composition. By annealing the oxide materials in an air atmosphere we were also able to effect changes in stoichiometry and the redistribution of other point defects associated with oxygen vacancies. By controlling grain size and boundary volume along with minimizing the influence of scattering centers on optical quality (i.e. making very transparent ceramics) the

effect of grain boundaries on scintillator properties within our model materials could be revealed.

For most characterization measurements, samples had to be carefully polished and either thermally or chemically etched to reveal the microstructural details. Both optical and scanning electron microscopy was employed for this purpose. Transmission electron microscopy was used to gain an atomistic view in the grain boundary region. Grain misorientation, alignment and lattice distortion in the grains near the boundary could be observed with this latter method. X-ray diffraction analysis was used for both structural and compositional analysis of some selected ceramic samples. Various other techniques were used during the course of this investigation to characterize the physical, optical and compositional properties of the samples produced, including Auger analysis, optical absorption spectroscopy, confocal microscopy, electron spin resonance (West Virginia University), NMR, pulsed x-ray emission spectroscopy (Lawrence Berkeley Laboratory), x-ray radioluminescence spectroscopy and XLRM- x-ray radioluminescence microscopy (SLAC-Stanford Synchrotron Radiation Lightsource), luminescence decay and CLTI-cathodoluminescence transport imaging (Naval Postgraduate School-Monterey, CA).

Highlights of the research are given in Section 4.

4. Scientific Results

4.1. *Eu:Y₂O₃ Ceramics: Sintering to High Optical Transparency and Optimizing Scintillation vs. Grain Size and Processing Parameters*

Highlights:

- *Special techniques were studied for preparing transparent ceramics of **Eu:Y₂O₃** from powders synthesized through various chemical means. Each preparative technique presented a trade-off between chemical homogeneity (i.e., Eu, Y) and optical transparency.*
- *The highest transparency **Eu:Y₂O₃** ceramics were prepared using mixed oxide powders that were ball milled and sintered through a step-wise application of temperature and pressure up to 1580°C and 40MPa. Optical transparency nearly reached that of a water-clear single crystal.*
- *Europium was found to act as a solid state sintering aid in **Eu:Y₂O₃** by enhancing the concentration of yttrium interstitials, which control the rate of diffusion mechanisms through which **Y₂O₃** densified. This permitted the production of highly transparent ceramics without introducing foreign species that can have a negative impact on scintillator performance.*
- *Other rare-earth dopants (both isovalent and aliovalent to Y³⁺) also acted as sintering aids in **Y₂O₃**, and their relative enhancement of diffusion was found to correlate with their chemical properties and defect chemistry, as opposed to an enhancement in migration energy of cations. Therefore, the diffusion mechanism that controls densification and the effect inclusion of additives has on the thermodynamics of defect formation will help to identify additives that will benefit the densification of ceramics.*
- *Observed a strong effect on ceramic light yield from processing conditions and oxygen stoichiometry. At the same time, above a minimum grain size, grain boundaries were found to have limited effect in **Eu:Y₂O₃** samples. These findings showed that the processing conditions that optimized transparency were not necessarily those conditions that optimized light yield.*
- *Although a relationship between light yield and grain size was observed, this dependence originated from the in-diffusion of oxygen through grain boundaries and into grains, decreasing the concentration of deep charge carrier traps.*

Experimental Details:

Ceramic Sintering

Ceramics were sintered from either: (1) “mixed oxide” (MO) powders of commercial Y_2O_3 and Eu_2O_3 (2) “precipitated” Eu_2O_3 nanopowders (NP) mixed with commercial Y_2O_3 , or (3) “co-precipitated” (CP) $\text{Eu}:\text{Y}_2\text{O}_3$ nanopowders. Green bodies of each of these powders were formed into 1-inch rounds by die pressing at 11.3 MPa to thicknesses between 8.0 and 8.5 mm. Green bodies were sintered by uniaxial hot-pressing, using two different temperature and pressure profiles: (1) a step-wise (SW) program (e.g., Figure 2(a)) and (2) a single-step (SS) program (e.g., Figure 2(b)). Although the majority of samples were translucent after hot-pressing, residual porosity in these ceramics was further decreased by hot-isostatic pressing (HIPing) under 200 MPa in a pressurized argon vessel at 1700°C for 2 hours. These samples were finally annealed in air to both oxidize the Eu that was reduced during hot-pressing ($\text{Eu}^{2+} \rightarrow \text{Eu}^{3+}$) and to re-introduce oxygen lost during sintering (restoring stoichiometry).

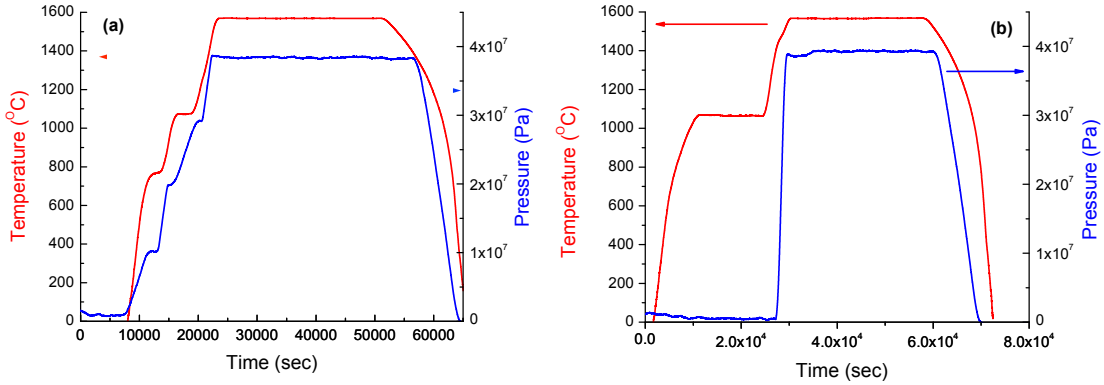


Figure 2: Example sintering profiles for (a) step-wise and (b) single-step programs.

Ceramic densification was monitored during hot-pressing by recording the displacement of the graphite plunger in the hot-press furnace (see schematic in Figure 3). The thermal and mechanical responses of the plungers over the course of the sintering program were calibrated in order to extract densification data from the plunger displacement. The thermal expansion, stiffness, and thermal diffusion of the graphite die set and graphite foil spacers were determined to the second-order (Table 1), and used to subtract out the background displacement, according to the relationship:

$$\frac{\Delta l}{l_0} = \alpha(T_m - T_{m0}) + \beta(T_m - T_{m0})^2 - \frac{\sigma}{Y_0} - \alpha\tau T_m \frac{dT_m}{dt} + \frac{1}{Y_0^2} \frac{dY}{dT} T_m \sigma - \frac{\tau}{Y_0^2} \frac{dY}{dT} \frac{dT_m}{dt} T_m \sigma \quad (1)$$

where $\frac{\Delta l}{l_0}$ is the dimensional change of the graphite plungers during hot pressing, T_m is the temperature measured by the pyrometer at the edge of the die case, σ is the applied stress, t is time, α and β are the first- and second-order thermal expansion coefficients of the graphite, Y_0 is its Young's modulus, and τ is the characteristic time for thermal diffusion from the outside to the inside of the die.

The following coefficients were used to determine the background:

$$\begin{aligned} A &= \alpha l_0 & B &= \beta l_0 & C &= \frac{l_0}{Y_0} \\ D &= \alpha \tau l_0 & E &= \frac{l_0}{Y_0^2} \frac{dY}{dT} & F &= \frac{\tau l_0}{Y_0^2} \frac{dY}{dT} \end{aligned} \quad (2)$$

Table 1: Graphite Die Thermal and Stress Coefficients

Coefficient	Value
A	1.59E-3 mm·K
B	5E-9 mm
C	3.4E-8 mm·Pa ⁻¹
D	5.5E-5 mm·K·s ⁻¹
E	1E-11 mm·Pa ⁻¹ K ⁻¹
F	7E-12 mm·s·Pa ⁻¹ K ⁻¹

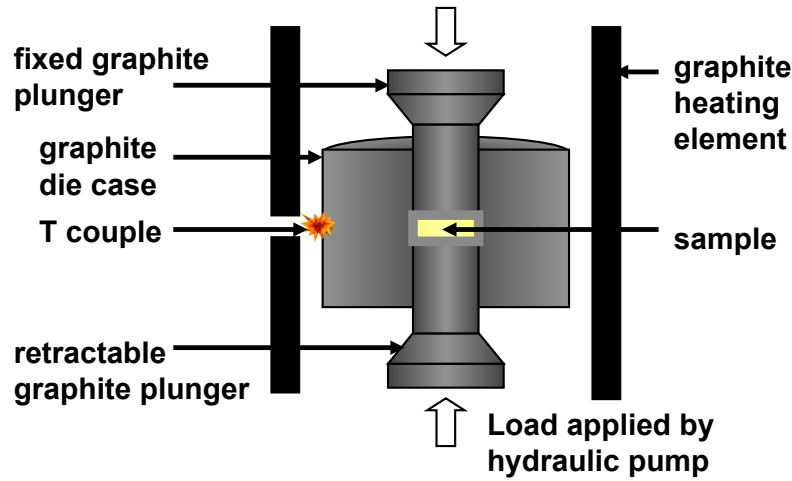


Figure 3: Schematic of graphite hot press.

Sintering from Different Starting Powders Produced through Various Methods

The principal goal of the Eu:Y₂O₃ sintering studies was to develop a process that could produce highly-transparent ceramics with different grain sizes and point defect concentrations. The role of these variables on scintillator performance could then be evaluated using a variety of characterization techniques. A number of previously successful routes for preparing transparent rare-earth oxide bixbyite ceramics were first identified [1-24]. From among them, hot-pressing was chosen as being the most viable. Starting powders for hot pressing were synthesized by a number of techniques in order to assess the effects of both chemical homogeneity and increased driving forces for inter-particle diffusion on sintering dynamics and ceramic properties.

Two types of starting material were used in these studies: (1) pre-reacted (Eu,Y)₂O₃ and (2) mixed Eu₂O₃ and Y₂O₃ powders. Figure 4 shows scanning electron microscopy (SEM) images of powders used as starting materials for the ceramics shown in Figure 3.9. The X-ray diffraction (XRD) results on the NP powders showed the presence of both Y₂O₃ and Eu₂O₃, while the CP powders contained only the cubic Y₂O₃ bixbyite structure (compare XRD patterns in Figure 5). While all the three synthesis methods described in the previous section produced transparent ceramics (as seen in Figure 6), the lowest optical attenuation was obtained using the mixed oxide (MO) method. However, sintering ceramics from powders produced by the other two methods also had some advantages. For example, in our initial studies on the MO and NP processes, Eu was found to be more homogeneously dispersed in the NP ceramics. Red particulates, which were hundreds of micrometers in size, were observed under an optical microscope in the MO ceramics, but not in NP ceramics (see Figure 7). This phase was found to be highly Eu-rich. However, when MO powders were ball milled rather than mixed with a mortar and pestle before sintering, these particulates were not observed. Initially, we avoided ball milling powders in order to prevent Zr contamination from the balls, but we ultimately found <5 ppm of Zr in ball milled powders as measured by inductively coupled plasma mass spectrometric (ICP-MS) analysis.

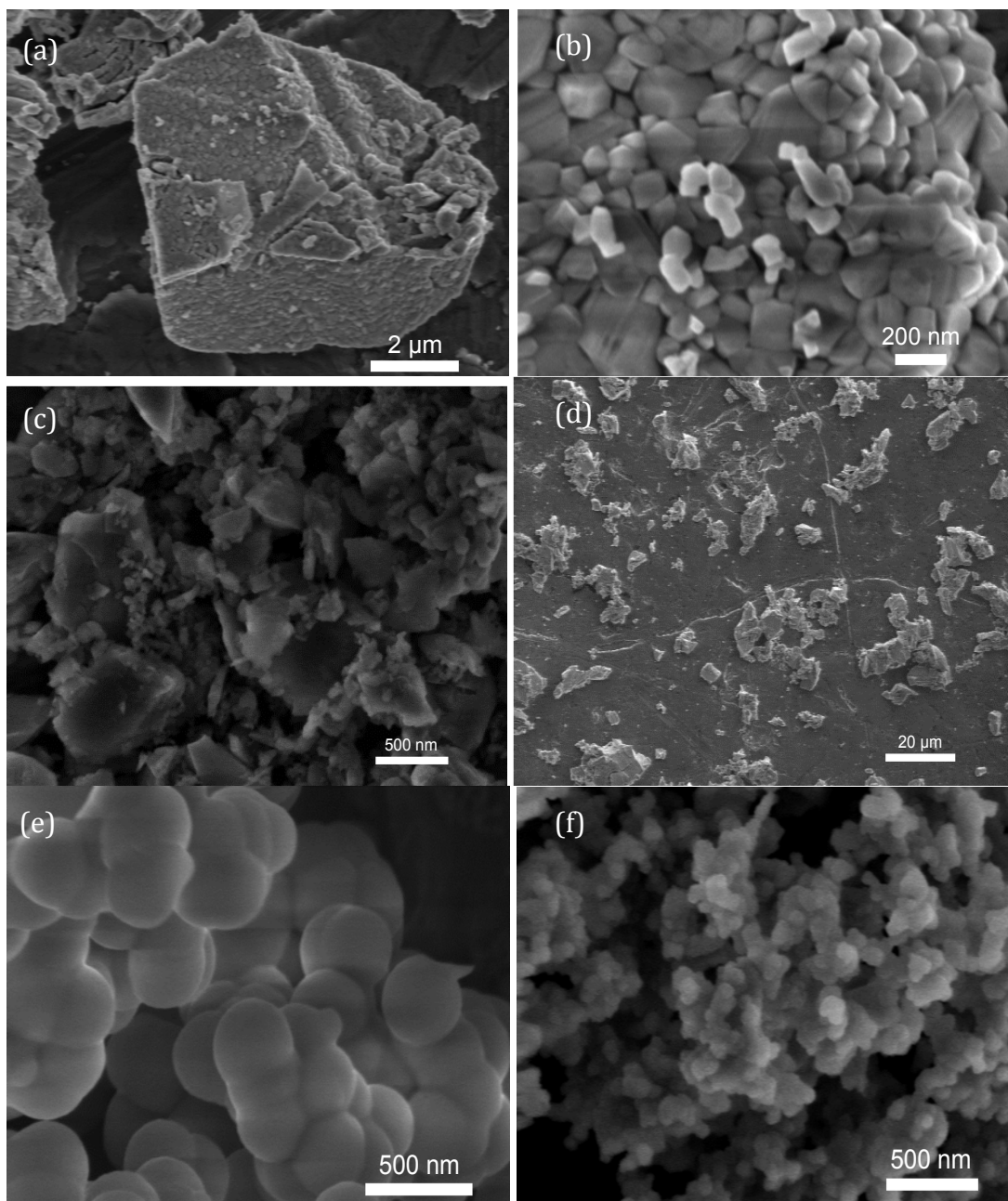


Figure 4: Scanning electron microscopy (SEM) images of commercial powders of (a) Y_2O_3 and (b) Eu_2O_3 , NP powders showing (c) Y_2O_3 particles, (d) close-up of particle in (c) with Eu_2O_3 particles on surface, and CP powders produced with $[\text{RE}^{3+}]$ and $[\text{Urea}]/[\text{RE}^{3+}]$ of (e) 0.05M and 20 and (f) 0.5M and 20.

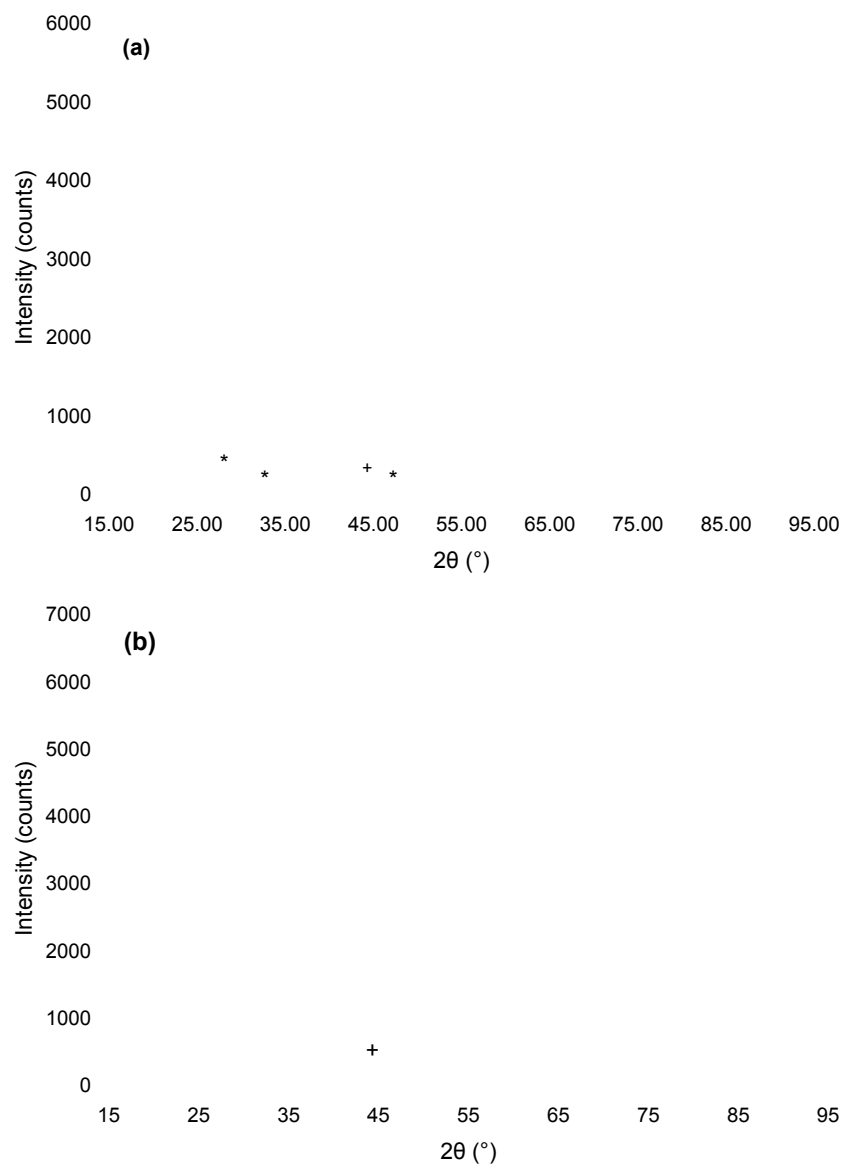


Figure 5: Typical X-ray diffraction (XRD) patterns of (a) NP and (b) CP powders. * denotes cubic Eu_2O_3 peaks, and + denotes an aluminum peak from the sample stage. All other peaks can be assigned to the cubic Y_2O_3 crystal structure.

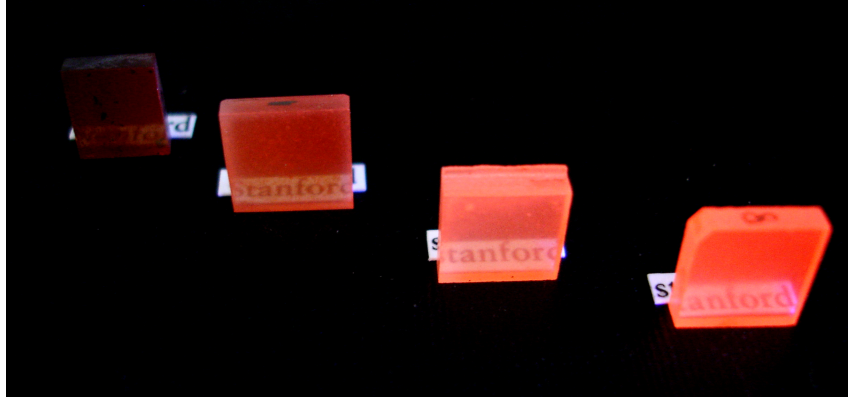


Figure 6: Picture of (from left to right) unannealed MO, and annealed CP, NP, and MO ceramics under 282 nm ultraviolet irradiation.

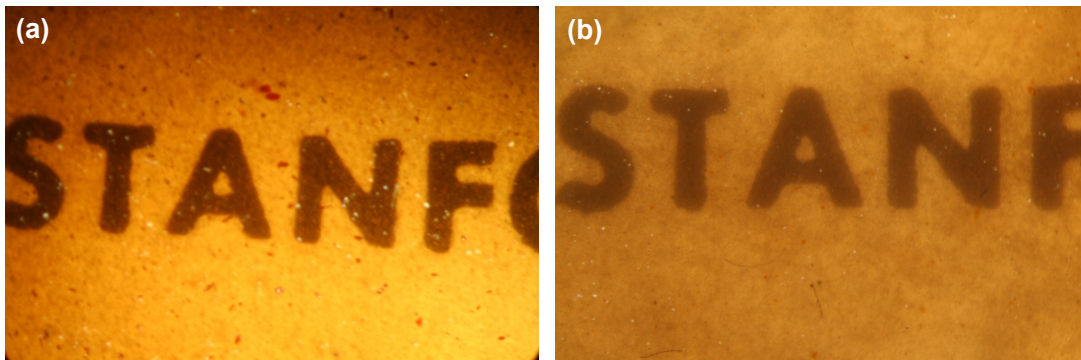


Figure 7: Optical micrographs of (a) MO and (b) NP ceramics, showing red particulates in (a) and their absence in (b).

On the nano-scale, particulates of an Eu-rich phase were also observed at grain boundaries in NP ceramics (see Figure 8). While yttrium oxide has a single cubic crystal structure, europium oxide can exist in one of four phases. The most oxygen-rich phase, Eu_2O_3 , crystallizes in both the bixbyite cubic structure and a monoclinic structure. When Eu is completely reduced to its divalent phase, it forms an oxide with a cubic rocksalt structure. An orthorhombic intermediate phase, Eu_3O_4 , also exists with a 2:1 ratio of Eu^{3+} to Eu^{2+} . Interplanar spacings between the diffraction planes shown in Figure 8(b) were calculated from Bragg's Law. Values for the interplanar spacing are given in Table 2. The most likely candidate for the structure of the particulates was found to be Eu_3O_4 . In fact, some of the earliest reports on Eu_3O_4 showed that it could be produced by hot pressing in a graphite die [1].

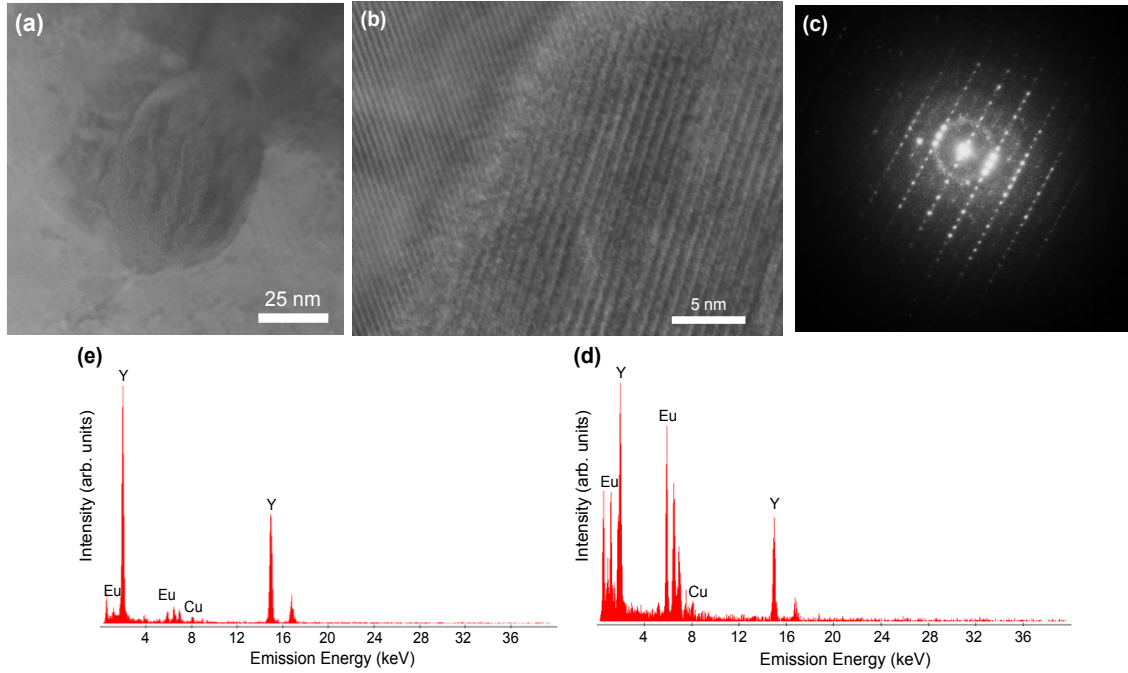


Figure 8: Transmission electron microscopy (TEM) analysis of a particulate at a grain boundary in an NP ceramic: (a) TEM image of particulate, (b) TEM image of lattice fringes in the particulate and surrounding cubic-phase grain, (c) image of selected area electron diffraction pattern, and electron dispersive spectroscopy (EDS) X-ray spectra of (d) the Eu-rich particulate and (e) an adjacent grain. The observed Cu emission originated from the Cu sample mount.

Table 2: Lattice Parameters and Interplanar Spacing of Europium Oxides

Europium Oxide Lattice Parameters						
Material	Structure	a (Å)	b (Å)	c (Å)	α (°)	Ref.
Eu ₂ O ₃	cubic	10.859	---	---	90	[26]
Eu ₂ O ₃	monoclinic	14.108	3.608	8.810	100.12	[27]
Eu ₃ O ₄	orthorhombic	10.085	12.054	3.502	90	[1]
EuO	cubic	5.143	---	---	90	[28]
Calculated Interplanar Spacing of Eu-Rich Particulates						
3.511 Å		14.267 Å		Eu ₃ O ₄	orthorhombic	(110)

Analysis of the microstructures of sintered ceramics showed that these particles may have caused grain boundary pinning, leading to smaller grain sizes. While the initial size of the Y₂O₃ particles was the same for both MO and NP starting powders, the final grain sizes of ceramics sintered from these powders were consistently smaller in NP ceramics (Figure 9(a)). Small insoluble particulates may pin grain boundaries. Grain boundary pinning has in many instances been shown to lead to

increased final density by decreasing the mobility of grain boundaries, thereby preventing pore-boundary separation [29]. In our experiments, prior to air annealing, NP ceramics did appear more transparent than MO ceramics. However, following annealing, NP ceramics were found to have larger optical attenuation coefficients than MO ceramics processed under identical conditions (Figure 9(b)). The only exception was for sintering above 1700°C, where grain boundary pinning in the NP ceramics prevented the abnormal grain growth observed in the MO ceramics.

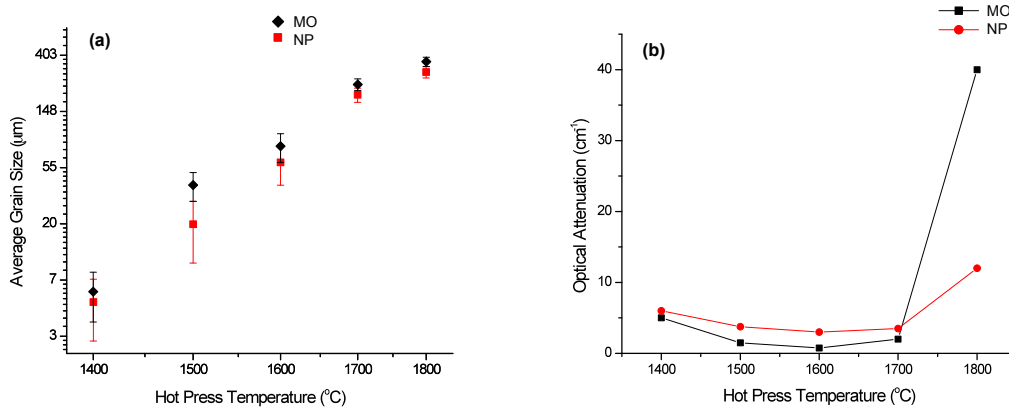


Figure 9: (a) Grain size and (b) optical attenuation after HIPing and annealing of MO and NP ceramics hot pressed at different temperatures.

The decrease in transparency of NP ceramics after air annealing appears to have been related to the in-diffusion of Eu from the grain boundaries into the bulk of the grains. Fluorescence scanning confocal micrographs of the Eu³⁺ emission showed a higher concentration of Eu at the grain boundaries than in the grains in unannealed samples (Figure 10(a)). After annealing the same ceramic, Eu was no longer segregated at the boundaries (Figure 10(b)). At the same time, pores were found to have grown in size and, in some cases, became separated from the boundaries. The microstructural changes at the boundaries, due to the incorporation of Eu into the grains after oxidation, may have caused void growth and coalescence, which degrade optical transparency.

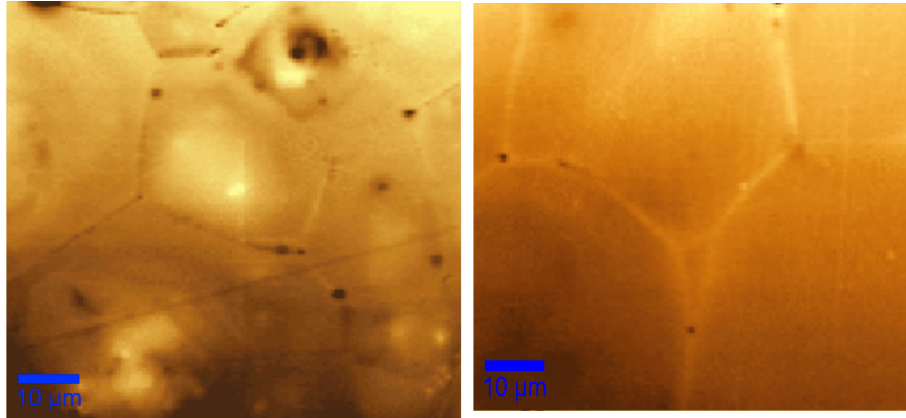


Figure 10: Fluorescence scanning confocal microscopy images of 611 nm Eu^{3+} emission at a depth of 10 μm below the surface for the same NP ceramic: (a) unannealed and (b) air annealed. The ceramic was hot pressed using a step-wise sintering program up to 1700°C for a soak time of 8 hrs, HIPed at 1700°C for 2 hrs, and air annealed at 1200°C for 6 hrs.

Ceramics sintered from CP powders were also found to have lower optical quality than the MO ceramics (see transmission spectrum in Figure 11). CP samples were found to be gray even after aggressive air annealing (1200°C for 48 hours). Because of the lower optical transmission of CP and NP samples, the samples used for the scintillation studies discussed later in this section and in Section 4.2 were fabricated by the MO method with ball-milled powders.

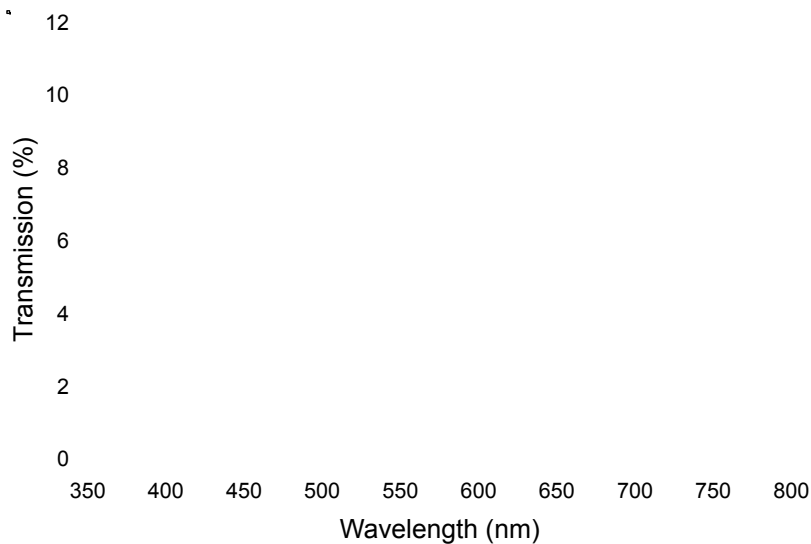


Figure 11: Optical transmission of 5 at.% $\text{Eu}:\text{Y}_2\text{O}_3$ ceramic made from CP powders. Compare to absorption spectrum of annealed MO ceramic in Figure 15(a).

Sintering with Various Temperature and Pressure Profiles



Figure 12: A 5 at.% Eu:Y₂O₃ transparent ceramic (optical attenuation 0.14 cm⁻¹) produced by the MO method and sintered using the step-wise program.

The highest optical transparency was reached in mixed oxide ceramics sintered through a step-wise application of pressure and temperature up to 40 MPa and 1580°C (Figure 12). A step-wise technique for sintering Y₂O₃ was previously suggested by Majima, et al. [30], who sintered their material with LiF. Their step-wise procedure was used in order to allow the LiF liquid phase that forms above 848°C to volatilize before the pore networks closed to the atmosphere, while at the same time, allowing the ceramics to sinter to optical transparency. In our study, no liquid phase was formed, but higher transparency was still observed. This is somewhat counterintuitive, because traditionally fast-firing is used to obtain high-density ceramics by quickly reaching a temperature at which densifying mechanisms are favored over non-densifying ones. However, by using the single-step program, a large ceramic shrinkage was observed during the pressure ramp (Figure 13(a)), while very little shrinkage of the sample was observed during the pressure ramps in the step-wise program (Figure 13(b)). Because of the relatively low sinterability of the large particles of the commercial powders, our MO ceramics did not reach final-stage sintering ($\sim 92\%$) until nearly at soak temperature. Below these densities, pressure may cause particle rearrangement by breaking the necks that have formed between grains. The resulting particulates can essentially behave as large hard agglomerates, leading to asymmetrical pore shrinkage [31,32]. This mechanism may account for the superior transparency obtained through step-wise over single-step sintering.

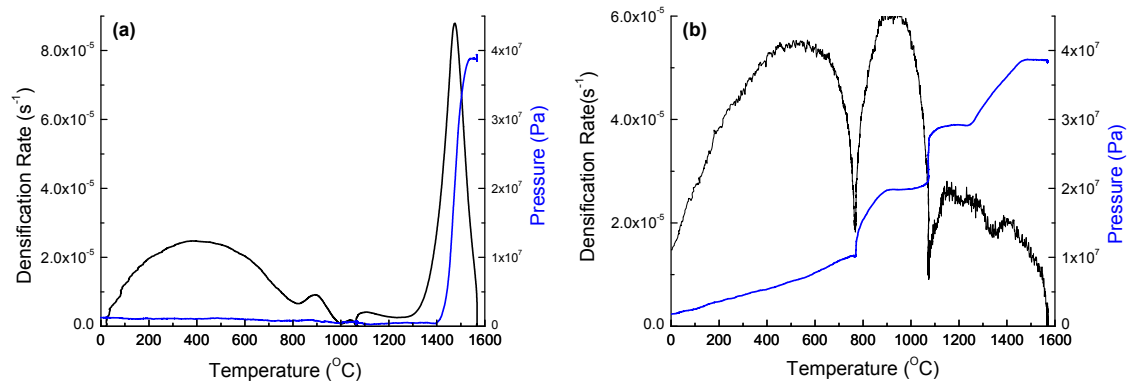


Figure 13: Densification rates of Eu:Y₂O₃ hot pressed with (a) non-step and (b) step-wise temperature and pressure profiles.

Rare-Earth Dopant Sintering Aids in Y₂O₃

Effect of Europium Concentration on the Densification of Transparent Eu:Y₂O₃ Ceramics

Because foreign elements previously used to enhance transparency in high-density ceramics can have a deleterious effect on scintillator performance [33], a study of alternative solutions was pursued. Based on some preliminary work in this laboratory suggesting that Nd doping in Y₂O₃ laser ceramics enhanced densification over pure Y₂O₃ a study of the effects of Eu concentration on ceramic densification, ceramics was initiated.

Samples were sintered from starting powders that contained either 0, 0.05, 0.5, 2, or 5 at.% Eu³⁺. A modified sintering program was implemented to simplify the analysis. This program included a high-temperature ramp at constant pressure and a pressure ramp at constant, high temperature. After a dwell at 1150°C to outgas the samples, a pressure of 10 MPa was applied to the samples, followed by a temperature ramp at 8°C/min to 1580°C. After a 30 min dwell at constant temperature and pressure, the pressure was ramped at 0.4 MPa/min to 40 MPa. These samples were then soaked at maximum temperature and pressure for 8 hours to develop their optical transparency. A set of ceramics was also quenched at three different points on the pressure ramp (0, 25, and 40 MPa), in order to study the kinetics of densification and grain growth.

Although unquenched samples were translucent after hot-pressing, residual porosity in these ceramics was further decreased by hot-isostatic pressing (HIPing) at 200 MPa under pressurized argon at 1700°C for 2 hours. These samples were

then annealed in air at 1100°C to both oxidize Eu^{2+} to Eu^{3+} and to re-introduce oxygen lost during sintering to restore stoichiometry.

The optical transparency of the ceramics prepared in this study was found to increase with increasing Eu concentration (Figure 14). Optical losses were primarily due to scattering from submicrometer porosity (Figure 14(inset)). Near the Eu^{3+} emission wavelength, the optical attenuation of these samples varies between 7.15 cm^{-1} and 1.20 cm^{-1} . This trend between transparency and Eu concentration indicates the positive effect that Eu doping has on the elimination of porosity in Y_2O_3 .

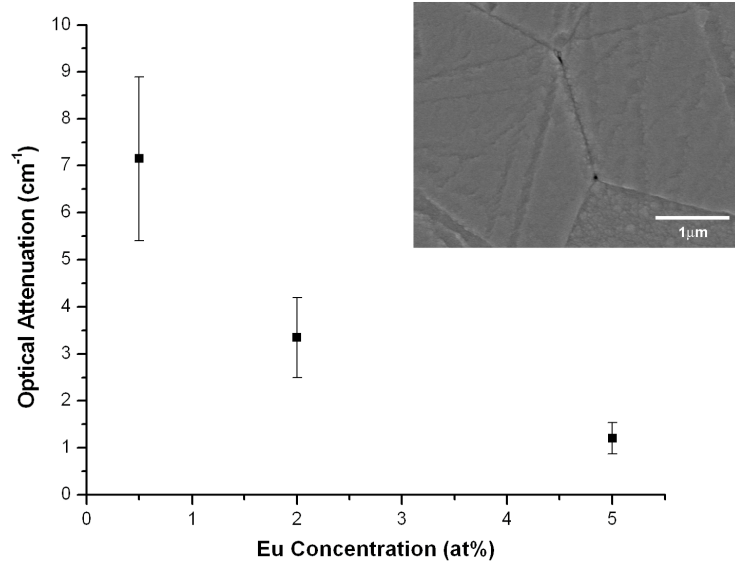


Figure 14: Variation of in-line optical attenuation at 633 nm with Eu concentration. (inset) Scanning electron micrograph of a 0.05 at.% $\text{Eu}:\text{Y}_2\text{O}_3$ after an 8-hr soak at 1580°C in the hot press, showing submicrometer porosity.

In addition to the Eu^{3+} absorption peaks and the characteristic host band edge beginning at 292 nm [34], unannealed samples showed a large optical attenuation in the visible region (Figure 15(a)). While this attenuation cannot be attributed to scattering alone, the defect responsible for the broad-band absorption could not be easily identified. The contributions of Eu^{2+} and oxygen defects formed in the reducing environment during hot-pressing and the higher-energy excitations of Eu^{3+} cannot be easily deconvoluted in this region of the spectrum [35,36]. However, the observed emission band centered at 404 nm in the emission spectrum of the unannealed sample shown in Figure 15(b) confirms the presence of Eu^{2+} in unannealed samples [35,37,38]. This emission was absent in spectra of air-annealed samples, while the $^5\text{D} \rightarrow ^4\text{F}$ transition peaks of Eu^{3+} were prominent in spectra from both samples (Figure 15(b)). This partial reduction of Eu to its divalent state was a common feature of all unannealed samples that had been hot-pressed under the conditions discussed in this study.

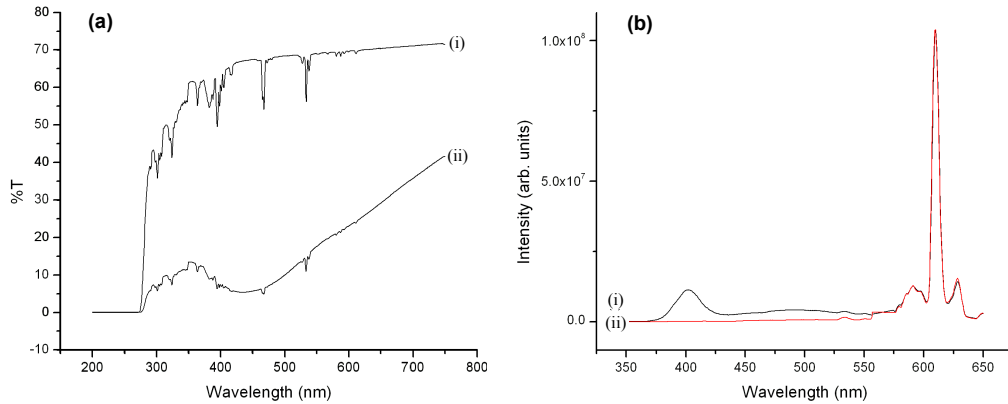


Figure 15: (a) Optical transmission and (b) emission ($\lambda_{\text{exc}} = 282 \text{ nm}$) spectra of (i) annealed and (ii) unannealed 5 at.% Eu:Y₂O₃. The Fresnel limit for transmission through two smooth parallel surfaces of undoped Y₂O₃ is 81.6% at 600 nm and 78.8% at 400 nm [39]. The emission intensity of unannealed sample magnified by $\times 3.21$ so that the strongest Eu³⁺ emission peaks corresponding to the ⁵D₀—⁷F₂ transition are displayed with equal intensities for both spectra.

In order to investigate the relationship between transparency and Eu concentration, we examined the differences in densification rate and grain growth by which these dissimilar levels of transparency were reached. Figure 16 shows the evolution of grain size and relative density for ceramics of varied Eu concentrations sintered under identical processing conditions. The grain size and density are shown to increase with increasing Eu concentration. Average grain sizes for these ceramics are given in Figure 17. Similar enhancements of Y₂O₃ grain growth and density were observed previously in conjunction with incremental increases in concentration of divalent dopants in solid solution [40,41]. This behavior suggests that a drag force from either solute segregation or secondary phases does not significantly impede grain boundary mobility. Figure 18 shows a TEM image of a representative grain boundary in 5 at.% Eu:Y₂O₃, confirming the absence of secondary phases at the boundaries in this system.

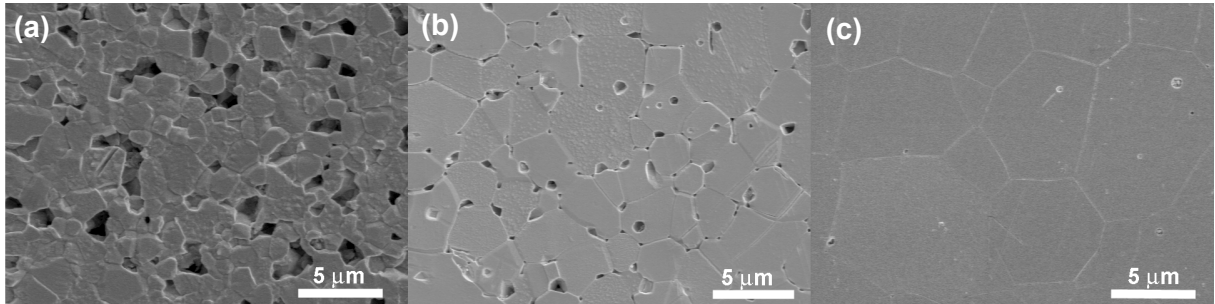


Figure 16: Scanning electron micrographs of (a) undoped, (b) 0.5 at.%, and (c) 5 at.% Eu:Y₂O₃ ceramics. The pictured microstructures are of hot-pressed ceramics sintered at 1580°C for 1 hr and under a pressure ramped up to 25 MPa (without hot isostatic pressing or annealing).

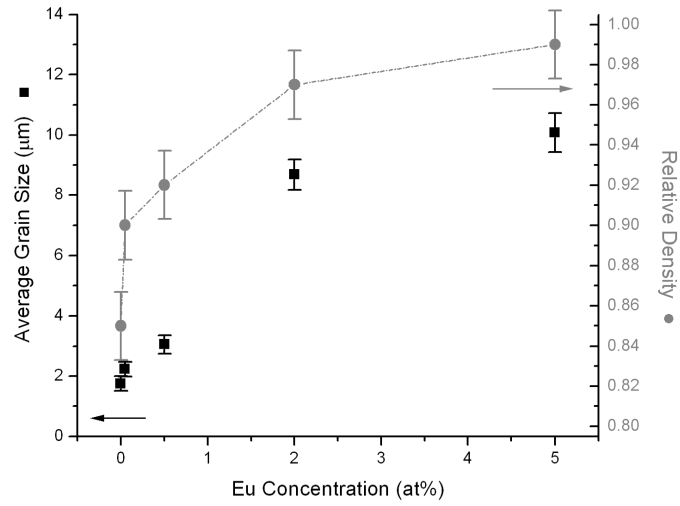


Figure 17: Variation of average grain size (n) with Eu concentration for ceramics processed under identical conditions, and variation of the final relative density of ceramics (●) with Eu concentration, after hot pressing at 1580°C up to 25 MPa.

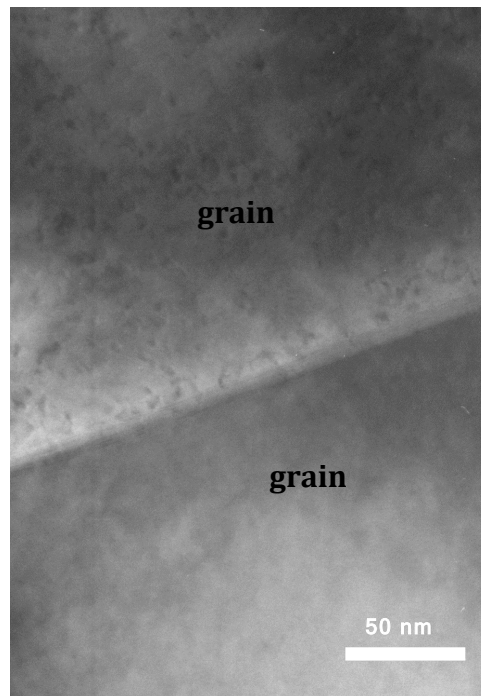


Figure 18: TEM image of typical grain boundary in Eu:Y₂O₃ ceramic, showing an absence of a Eu-rich secondary phase at the boundary.

To study any changes to the mass transport kinetics during densification as a function of dopant concentration, linear strain rates were monitored during hot-pressing. Strain rates were found to decrease monotonically with increasing concentration (Figure 19). The strain rate of a densifying ceramic will continually decrease below its maximum value, as the ceramic approaches its end-point density and the kinetics for densification slows due to reduction of both the effective stress and the driving force for pore shrinkage [42,43]. Because the strain rates of these samples were observed at concomitant points in the program, at which grain sizes and densities vary between samples (Figure 17), the observed strain rates will vary in proportion to these microstructural parameters. The changes in grain size were found to only be dependent on density, and therefore the densification rate decreases with increasing density in the range considered here. This decrease is reflected in the trend in ceramic strain rate with Eu concentration presented in Figure 19.

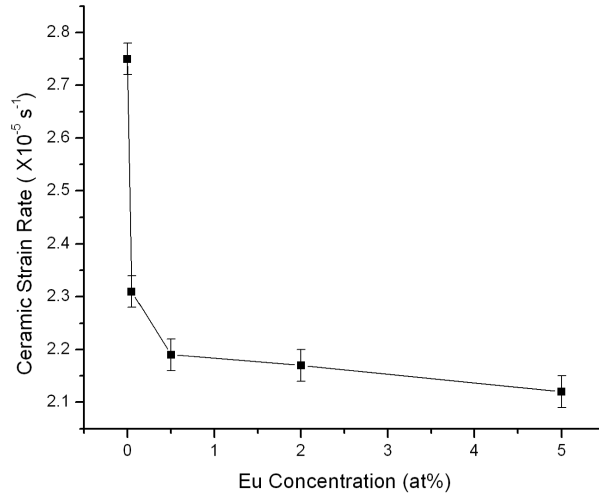


Figure 19: Variation of ceramic strain rate with Eu concentration of ceramics processed under identical. The strain rates reported were measured at 1580°C and 25 MPa.

In order to elucidate the relationship by which the densification kinetics vary with Eu concentration in Y_2O_3 , the analytical sintering models developed by Coble [44] and Helle, et al. [45] were utilized. Grain-boundary diffusion has been reported to dominate mass transport during the densification of Y_2O_3 ceramics having grain sizes of 1 and 10 μm [46,47]. Therefore, an analytical model for grain-boundary diffusion-controlled densification was considered here. For final stage densification, strain rate ($\dot{\epsilon}$) during hot-pressing may be described by the analytically derived equation [44]:

$$\dot{\epsilon} \approx \frac{1}{\rho} \frac{d\rho}{dt} = \frac{15}{2} \left(\frac{D_{gb} \delta_{gb} \Omega}{G^3 kT} \right) \left(\phi P + \frac{2\gamma_{sv}}{r} \right) \quad (3)$$

where D_{gb} and Ω are the grain-boundary diffusion and atomic volume of the rate-controlling species for densification at the temperature (T) and pressure (P) considered, δ_{gb} is the grain boundary thickness, G is the average grain size, and $2\gamma/r$ is the sintering stress, which is dependent on the surface energy and pore radius. Because the driving force for densification under applied pressure (25 MPa) dominates over the sintering stress (the sintering stress $2\gamma/r$ can be estimated to be on the order of 2 MPa), the sintering stress could be neglected for diffusion constant calculations. The stress intensification factor (Φ) for densification by diffusional flow derived by Helle, et al. [45] is given by

$$\frac{(1 - \rho_0)^2}{\rho(\rho - \rho_0)^2}, \text{ for relative densities up to 0.9}$$

$$\frac{(1 - \rho)^{1/2}}{\rho}, \text{ above 0.9.} \quad (4)$$

Using Eqns. 3 and 4 and the strain rates and grain sizes reported in Figure 17(a) and Figure 19, the evolution of diffusivity with Eu concentration was derived for a constant temperature and pressure (Figure 20). The grain-boundary diffusion constant was found to be dramatically dependent on Eu-doping concentration, varying three orders of magnitude over the investigated concentrations. Thus, Eu-doping was found to enhance diffusion-controlled densification.

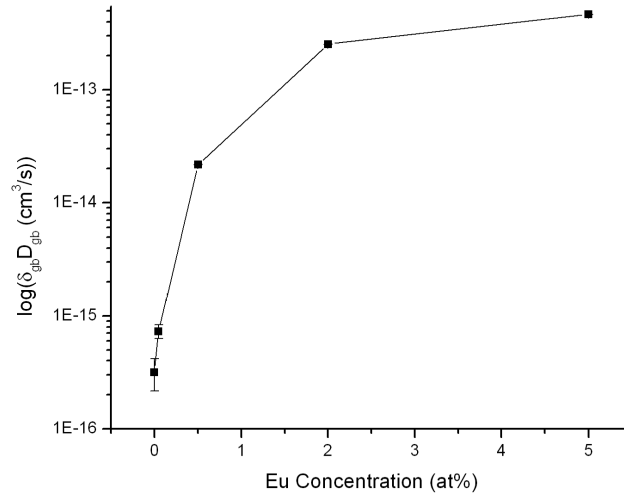


Figure 20: Variation of calculated effective diffusion constants with Eu concentration. $\delta_{gb}D_{gb}$ calculated from experimentally derived ceramic strain rates, grain sizes, and densities.

In order to investigate the effect of introducing Eu in its divalent state at the start of the sintering process, Eu:Y₂O₃ ceramics were formed by reactive sintering with EuO

as a starting material. Samples were fabricated with doping-levels of 0.05 and 1 at.% Eu. These samples were sintered with the same temperature-pressure program as $\text{Eu}_2\text{O}_3\text{:Y}_2\text{O}_3$ samples, and quenched during the pressure ramp for grain-size measurements.

This companion study, carried out with EuO as a Eu^{2+} source, showed that for a 0.05 at.% Eu: Y_2O_3 sample, formed from mixed EuO and Y_2O_3 green bodies, the grain size and density were greater than those of 0.05 at.% Eu samples produced by mixing with Eu_2O_3 (Figure 21(a)). Calculated diffusivity was found to be ~ 6 times greater than in samples of 0.05 at.% Eu from an Eu_2O_3 source. When doping levels reached 1 at.%, however, grain growth was inhibited (Figure 21(b)), with average grain sizes smaller than that of both 0.5 at.% Eu made from Eu_2O_3 and 0.05 at.% from EuO.

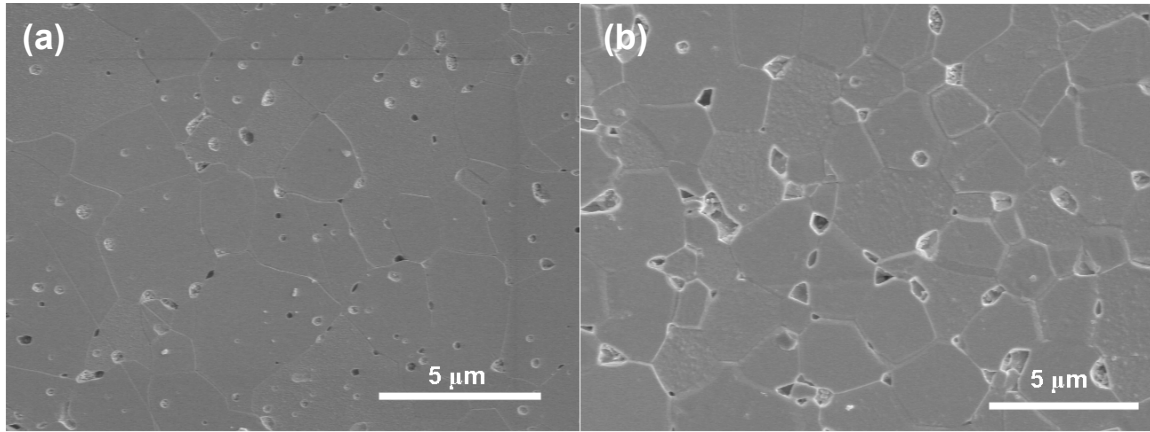


Figure 21: Scanning electron micrographs of (a) 0.05 at.% and (b) 1 at.% Eu: Y_2O_3 sintered from mixed EuO and Y_2O_3 green bodies.

The observed enhancement of diffusivity with addition of EuO as a Eu source for reactive sintering provides additional verification that the presence of Eu^{2+} enhances diffusivity in Y_2O_3 . Further investigation of the early stages of sintering and the oxygen equilibrium between EuO and Y_2O_3 is needed to fully understand the relationship between the results obtained for 0.05 at.% versus 1 at.% doping. It may indicate a transition between densification mechanisms. However, the diffusion enhancement observed for a low concentration of Eu (introduced as EuO), when compared with the limited enhancements to diffusivity previously reported for the doping of Y_2O_3 with isovalent rare-earths [46], supports the choice of a point defect chemistry approach based on the valence state of Eu to evaluate sintering in this system.

Because Eu^{2+} was present in solid solution with Y_2O_3 after hot-pressing, we investigated the reduction of Eu as a causal mechanism for diffusion enhancement. At high enough Eu concentrations, Eu^{2+} will dictate the charge neutrality of the sys-

tem, and therefore control the equilibrium point defect concentrations. While dopants have been widely reported to influence diffusion processes by modifying the point defect concentrations of the host lattice [48], solid state sintering aids have also been shown to operate through a number of other mechanisms, including:

1. a change in the energy of pore surfaces, leading to a difference in the driving force for point defect diffusion away from pores [46].
2. lattice distortion that alters the energy required to create a transient activated complex at a saddle point within the potential energy surface along a diffusion path [49].
3. a difference in bond ionicity between the cationic species of the host compound and dopant ions, leading to a change in the migration energy of point defects [50].

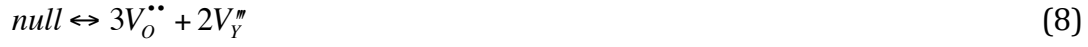
The effect of Eu_2O_3 on Y_2O_3 sintering from each of these thermodynamic changes is discussed in great detail in a publication derived from this work [51]. The analysis that is presented in the article justifies the use of the point defect chemistry model to interpret the way in which Eu operates as a sintering aid.

In another set of experiments, thermo-mechanical analysis was performed while heating Y_2O_3 samples. It was carried out under varied oxygen partial pressures. This study was used to verify the dominance of yttrium interstitial diffusion on the densification of Y_2O_3 [46,47,52,53] (see Figure 22). The densification rates of these undoped ceramic samples were monitored, while sintering in Ar- O_2 atmospheres. Grain sizes were measured on these samples, which were quickly cooled to room temperature. The calculated diffusion coefficients were found to have a negative log-linear relationship with a slope of 0.27 ± 0.04 . Because the concentration of yttrium interstitials in Y_2O_3 is proportional to the oxygen partial pressure to the -1/4 power (compare Figure 22 to Eqns. 5 and 6), yttrium interstitials were found to be the rate-limiting diffusion mechanism for densification in this study as well.

$$[Y_i^{\bullet\bullet\bullet}] = \left(\frac{K_F}{8} \right) \left(\frac{K_{O_2}^{(R)}}{K_S} \right)^{1/2} p_{O_2}^{-1/4} \quad (n\text{-type, reducing environment}) \quad (5)$$

$$[Y_i^{\bullet\bullet\bullet}] = \left(\frac{8K_F(K_{AF})^{3/2}}{(K_S K_{O_2}^{(O)})^{1/2}} \right) p_{O_2}^{-1/4} \quad (p\text{-type, oxidizing environment}) \quad (6)$$

where K_F , K_{AF} , and K_S are the mass action constants for cation Frenkel, Schottky, and anion Frenkel defect formation (reactions defined in Eqns. 7-9). $K_{O_2}^{(R)}$ and $K_{O_2}^{(O)}$ are the reduction and oxidation constants for the reactions in Eqns. A.II.8 and A.II.9. p_{O_2} is the oxygen partial pressure in the sintering atmosphere.



in a reducing environment:



in an oxidizing environment:



Changes to yttrium interstitial concentrations impact ceramic densification by altering the effective diffusivity of the material. The incorporation of Eu^{2+} into Y_2O_3 introduces a proportional concentration of oxygen vacancies, which in turn affects the equilibrium yttrium interstitial concentration according to the defect equilibrium of the system (Eqns. 7 and 8). We adopted a charge neutrality condition controlled by $Eu_Y^{'}$ concentration (Eqn. 12) [54], because the Eu doping concentration was, in our experiments, far higher than the intrinsic oxygen vacancy concentration—only $\sim 5 \times 10^{-7}$ in Y_2O_3 at a low oxygen partial pressure of 10^{-12} [46].



From the defect equations and the charge neutrality condition postulated here, and with binding energy for dopant-vacancy complexes being negligible compared with the thermal energy, we derived a relation between yttrium interstitial concentration and the concentration of divalent Eu substitutional defects given by:

$$[Y_i^{\bullet\bullet\bullet}] = \frac{K_F}{K_S^{1/2}} \left(\frac{[Eu_Y^{' }]}{2} \right)^{3/2} \quad (13)$$

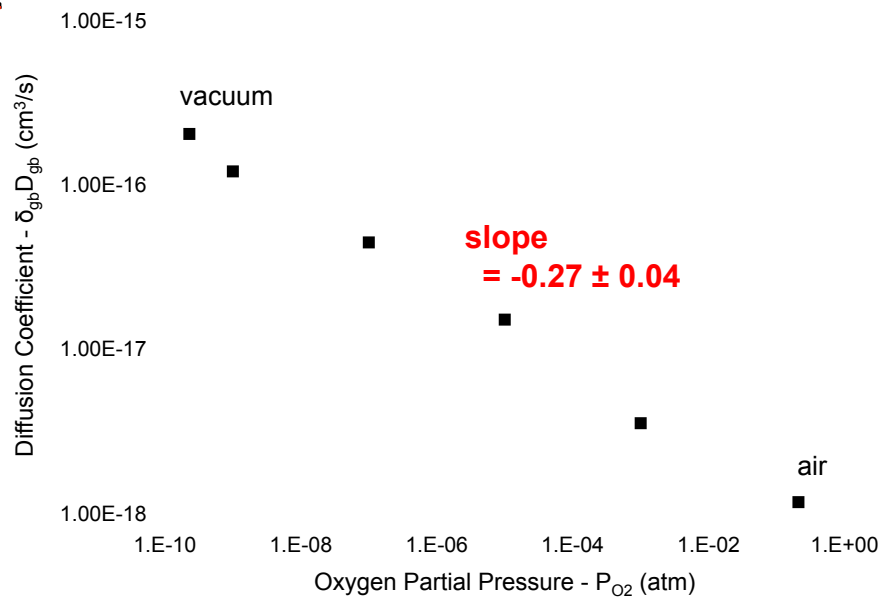


Figure 22: Grain boundary diffusion constants for undoped Y_2O_3 sintered in atmospheres with different oxygen partial pressures. Diffusion constants were calculated from ceramic densification data. The slope of $\sim -1/4$ is consistent with yttrium interstitial diffusion as the rate-limiting diffusion mechanism.

In general, for an interstitial-controlled diffusion mechanism, as is the case for the diffusion-controlled densification of Y_2O_3 considered here, the effective diffusion constant of the material is linearly proportional to the interstitial concentration, as is restated in Eqn. 14. Eqns. 14 and 15 also express the relationship between grain boundary diffusivity and self-diffusion of point defects and the atomistic properties on which self-diffusion depends.

$$D_{gb} = X_{def,gb} D_0 \exp(-\Delta G / kT) \quad (14)$$

$$D_0 = f a^2 z \nu_0 \quad (15)$$

where $X_{def,gb}$ is the mole fraction of grain boundary diffusion-controlling defects, D_0 is the temperature-independent prefactor of the self-diffusion coefficient, ΔG is the activation energy for diffusion. f is the correlation coefficient between sequential jump directions, a is the jump distance, z is the number of sites adjacent to the defect, and ν_0 is the jump attempt frequency. The dependence of these parameters on interstitial ion concentration in Y_2O_3 is discussed in a publication based on this work [51], which concludes that the grain-boundary diffusion constant of $Eu:Y_2O_3$ will be linearly proportional to $[Y_i^{***}]$ and proportional to $[Eu_Y']$ to the $3/2$ power.

The exact concentration of Eu^{2+} in our ceramics could not be measured, because of the absence of data on the oscillator strength of Eu^{2+} in Y_2O_3 and the difficulty of

differentiating ionic states of a low concentration dopant ion in polycrystalline materials. Therefore, we defined a relationship between the overall concentration of Eu introduced into the samples at the start of sintering (i.e., [Eu]) and diffusion coefficients. With the high reduction potential of Eu^{3+} in Y_2O_3 (compared to other defect creation processes in a reducing environment) [55], higher-order dependencies of $[\text{Eu}_y']$ on total Eu concentration may be neglected, and $[\text{Y}_i^{***}]$ can be directly associated with the initial Eu doping concentration.

Grain-boundary diffusion constants are plotted against total Eu doping concentrations in Figure 23. A log-linear relationship was observed, having a power-law relation of 1.46 ± 0.08 . This is in good agreement with the expected value of 1.5 (see Eqn. 13).

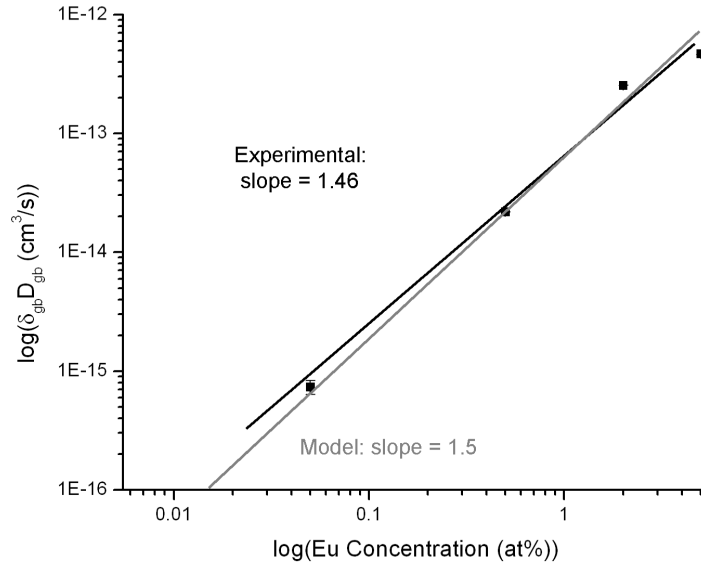


Figure 23: Experimental effective diffusion constant versus Eu concentration with log-linear fit and slope predicted by defect chemistry diffusional flow sintering model.

In summary, based on the strong agreement between experimentally-derived diffusion data and the defect chemistry model proposed here, the reduction of Eu during hot-pressing appears to control the changes in diffusivity observed between samples with varied Eu doping concentration. When coupled with the observations that end-point density was reached sooner for higher Eu concentrations (and higher yet when using Eu^{2+} in the starting material instead of Eu^{3+}), and that the ultimate transparency increased with increased Eu concentration, it was clear that Eu acts as a solid-state sintering aid in Y_2O_3 through changes to the ionic diffusivity of the ceramic system.

Densification of Rare-Earth Doped Y_2O_3 Ceramics

While the previous section showed that Eu serves as a sintering aid when partially reduced in the hot-pressing environment, others have reported increased transparency in bixbyite optical ceramics by co-doping with isovalent rare-earths, particularly Gd [56-58]. A study of the grain growth kinetics in isovalent rare-earth doped Y_2O_3 ceramics also showed enhanced grain boundary mobility during sintering in air [46]. In these cases, the final ceramic density cannot be explained by the reduction of an ionic species that controls the point defect chemistry of the system. Improvements in densification upon doping with isovalent ions that form solid solutions with their matrix compound have previously been attributed to either solute drag [59,60] or increased ionicity of bonding with anions [50]. However, isovalent dopants may also modify equilibrium point defect concentrations of the host material [61-65], thereby changing its diffusivity.

In this part of the study, the densification of Y_2O_3 using five different rare-earth oxide dopants (Sc_2O_3 , Eu_2O_3 , Gd_2O_3 , Yb_2O_3 , and Lu_2O_3) was investigated. When fully-oxidized, they are isovalent with Y^{3+} . Sintering studies were carried out in both a vacuum and air atmosphere. Two of these dopants (Eu and Yb) are multivalent and adopt a 2+-valency in oxygen-deficient environments. Thermal mechanical analysis was used to measure the contraction of the ceramics during sintering. The dependence of grain size on sintering temperature and time was also measured. Effective diffusion coefficients were calculated from these densification rates and grain sizes, according to a similar method as was described in the previous section.

The calculated grain boundary diffusion coefficients are presented in Figure 24. Three distinct regimes were observed: (1) ceramics with rare-earth dopants sintered in air, (2) ceramics with isovalent rare-earth dopants (Sc, Lu, Gd, undoped) sintered in vacuum, (3) ceramics with 2+/3+-multivalent rare-earth dopants (Yb, Eu) sintered in vacuum. The enhanced densification of Y_2O_3 doped with Yb sintered in vacuum may be attributed to the same effect observed for Eu-doped samples. The higher calculated diffusion coefficients for ceramics sintered in vacuum compared to those sintered in air may also be attributed to a higher concentration of oxygen vacancies and therefore yttrium interstitials, as discussed in the previous section.

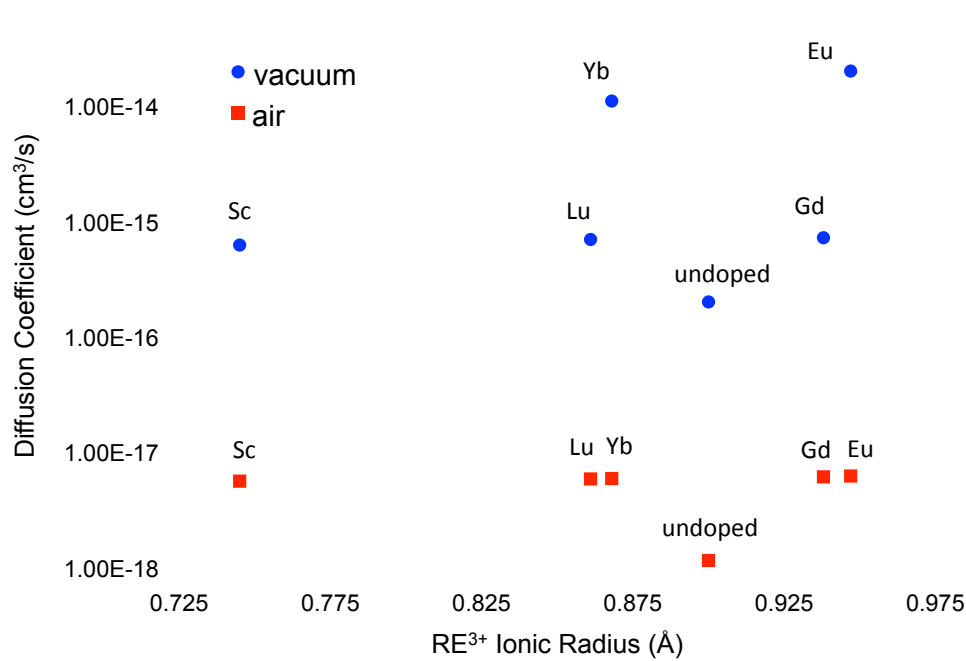


Figure 24: Experimental effective diffusion constants of rare-earth doped Y_2O_3 sintered in either vacuum (•) or air (■) compared to dopant ionic radii in their 3+-valency states with a 6-fold coordination.

As discussed in the previous section, solid state sintering aid effects have been variously attributed to: (1) an increase in the defect concentration, (2) an increase ionicity of bonding leading to increased ease of defect migration, and (3) a decrease in the mobility of grain boundaries due to solute drag. Because the grain size increased for all doped samples, compared to the undoped samples, solute drag on the grain boundaries did not appear to have occurred in the doped ceramics. Therefore, we compared calculated diffusivities to chemical properties of the dopant ions that are related to the other two effects, in order to identify which parameters were most significant to calculated diffusivities.

Figure 25 compares the calculated diffusion coefficients of ceramics sintered in air with different rare-earth ion chemical properties, such as ionic radii, the energy levels of the 5d orbitals of isolated ions with respect to the conduction band minimum (CBM) of Y_2O_3 , the electronegativities with respect to that of oxygen ($\chi_0 - \chi_{\text{RE}}$ —related to the bond ionicity [66,67]), and the calculated cation Frenkel defect formation energies. We have considered properties that affect the structure of the crystal lattice (lattice distortion and creation of point defects) and those that affect the bonding of ions and define their ionic character.

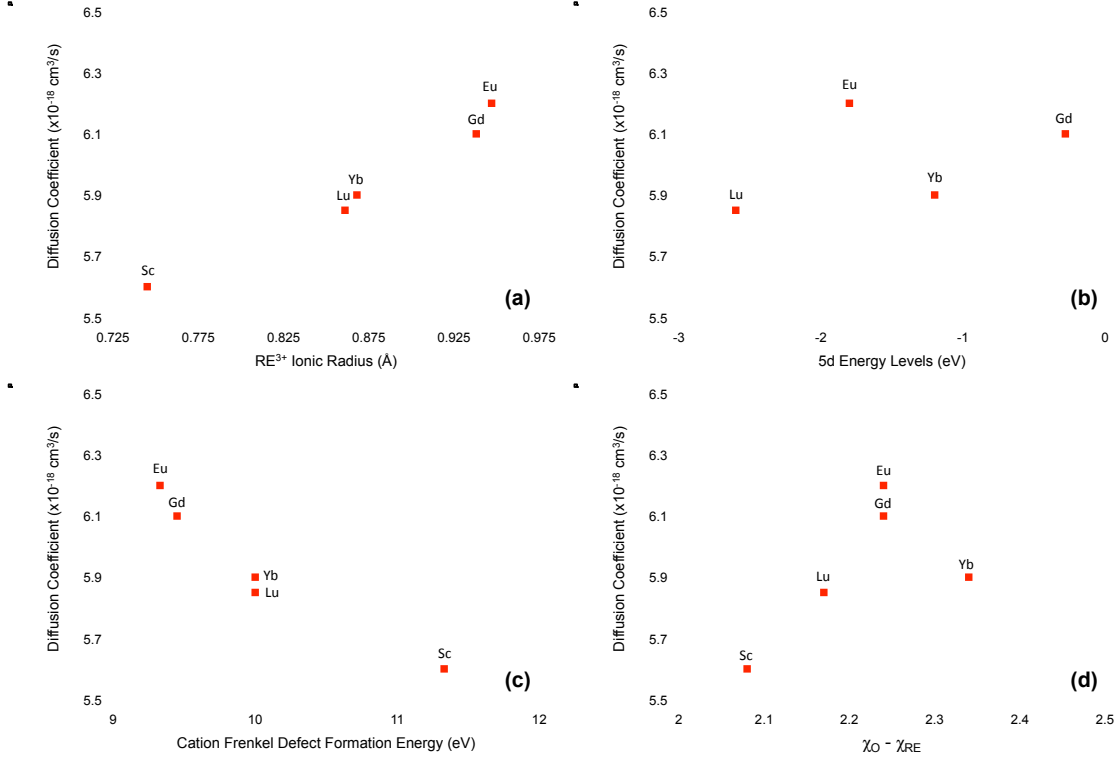


Figure 25: Experimental effective diffusion constants of 1 at.% rare-earth doped Y_2O_3 sintered in air compared to different rare-earth chemical properties, including (a) ionic radii, (b) energy levels of 5d orbitals, (c) cation Frenkel defect energy in pure rare-earth sesquioxide, and (d) electronegativity.

In Figure 25(a) and (c), there is a relationship between diffusion coefficients for densification and both ionic radii and the formation energies of cation Frenkel defects in the pure sesquioxides of the dopant ions. We did not observe a relationship between effective grain boundary diffusion coefficients and bond ionicity, however (see Figure 25(b) and (d)). For an asymmetric lattice distortion, the dopant radius is linearly proportional to the volume change in the lattice, and therefore exponentially proportional to the yttrium interstitial defect concentration, according to the relationship [68,69]:

$$X \approx X_0 \exp\left(\frac{-\sigma \Delta V_F}{kT}\right) \quad (16)$$

where X_0 is the initial concentration of defects in a stress-free system, σ is the internal stress field near the defect from the dopant, and ΔV_F is the relaxation volume of the defect.

Therefore, the relationships in Figure 25 are consistent with a model for a solid state sintering aid that acts to either affect or control the defect chemistry of the system, and thereby enhances its ceramic densification. It also shows that the migration energy, which is in part related to the bond ionicity [50], is not the most significant

driver of enhanced densification even for isovalent dopants, as was discussed in the previous section for Eu.

Thus, other rare-earth ions, including those that were both isovalent and aliovalent, were also found to act as sintering aids in Y_2O_3 . We observed a relationship between calculated grain boundary diffusion coefficients and valence state, ionic radius and cation Frenkel defect formation energy. At the same time, the sintering action of these additives could not be attributed to bond ionicity, as has been previously suggested by other studies of additives in Al_2O_3 . Therefore, to identify additives that may benefit the densification of ceramics, the diffusion mechanism that controls densification and the effect that inclusion of additives has on the thermodynamics of defect formation are particularly important. Further investigation on the effects of multivalencies and the interaction between dopants and host lattice defects will advance efforts to optimize ceramic processing for improved optical performance.

Scintillation Characterization

Effect of Grain Size and Processing on Light Yield in Eu:Y₂O₃ Transparent Ceramics

Sets of transparent 5 at.% Eu-doped ceramics were processed under varied conditions in order to control particular materials parameters. These ceramics were sintered step- wise from mixed oxide powders, HIPed, and air annealed, using the optimized step-wise process discussed earlier. Grain size was varied between 5 and 250 μm by varying the hot-pressing temperature at which ceramics were sintered (between 1400°C and 1700°C). In order to investigate the effect of a temperature treatment on light yield, ceramics hot-pressed under identical conditions (at 1500°C) were HIPed at varied temperature between 1500°C and 1800°C for 2 hours. Finally, a set of ceramics was hot-pressed and HIPed under identical conditions and then air annealed at 1150°C for different lengths of time between 0 and 96 hours. This was in order to produce different overall oxygen concentrations in the ceramics. Table 3 lists the processing conditions for the samples characterized in this study.

Table 3: Processing Conditions for Eu:Y₂O₃ Ceramics

Sample	HP Temp. (°C)	HIP Temp. (°C)	Anneal Temp. (°C)	Anneal Time (hrs.)
1A*	1400	1700	1150	16
2A*	1500	1700	1150	16
3A	1550	1700	1150	16
4A*	1600	1700	1150	16
5A	1650	1700	1150	16
6A*	1700	1700	1150	16

1B	1400	1700	1150	48
2B	1500	1700	1150	48
3B	1550	1700	1150	48
4B	1600	1700	1150	48
5B	1650	1700	1150	48
6B	1700	1700	1150	48
1C	1400	1700	1150	96
2C	1500	1700	1150	96
3C	1550	1700	1150	96
4C	1600	1700	1150	96
5C	1650	1700	1150	96
6C	1700	1700	1150	96
1D	1500	1500	1150	16
2D	1500	1600	1150	16
3D	1500	1700	1150	16
4D	1500	1800	1150	16
1E	1600	--	--	0
2E	1600	1700	--	0
3E	1600	1700	1150	8
4E	1600	1700	1150	16
5E	1600	1700	1150	24
6E	1600	1700	1150	36
7E	1600	1700	1150	48
8E	1600	1700	1150	72
9E	1600	1700	1150	96
1F	1700	--	--	0
2F	1700	1700	--	0
3F	1700	1700	1150	8
4F	1700	1700	1150	16
5F	1700	1700	1150	24
6F	1700	1700	1150	36
7F	1700	1700	1150	48
8F	1700	1700	1150	72
9F	1700	1700	1150	96
1G	1600	1700	1050	16
2G	1600	1700	1100	16
3G	1600	1700	1150	16
4G	1600	1700	1200	16
5G	1600	1700	1250	16
6G	1600	1700	1300	16

Integrated X-ray Radioluminescence Intensity

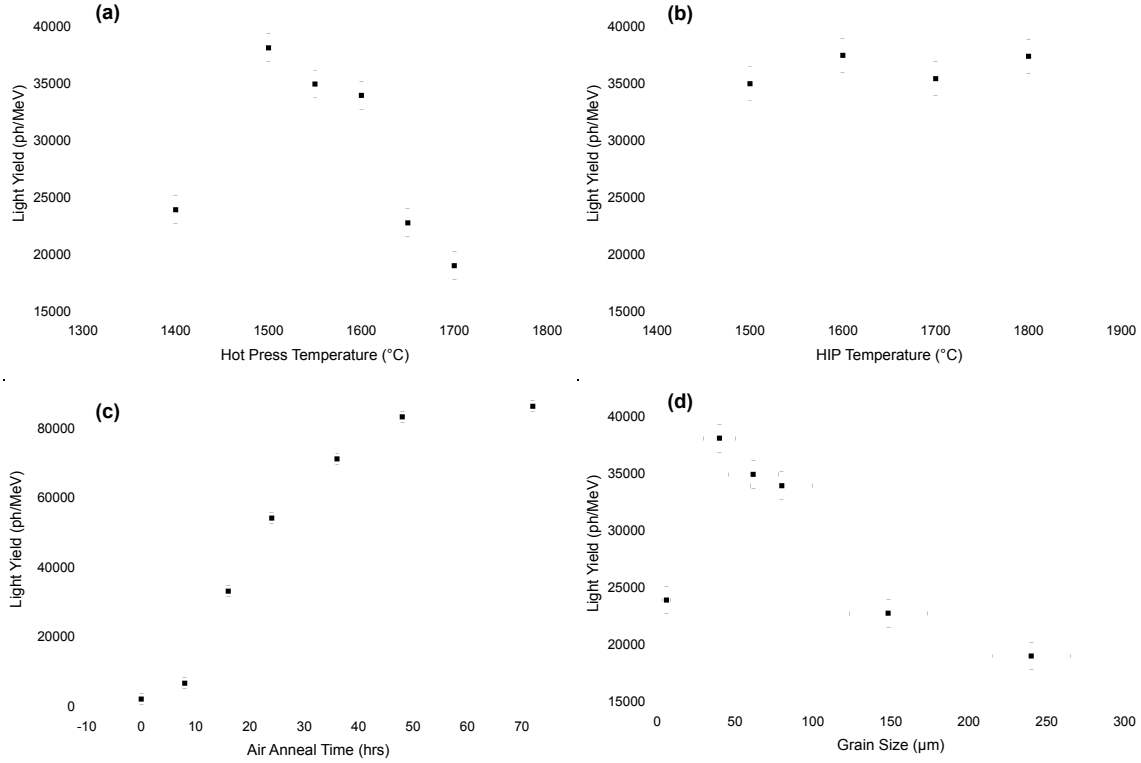


Figure 26: XRL intensity of ceramics (a) hot-pressed at varied temperatures, (b) HIPed at varied temperatures, (c) air annealed for varied times, and (d) with different grain sizes obtained through hot-pressing at varied temperature.

Figure 26 shows the light yield of the Eu:Y₂O₃ ceramics as a function of (1) hot-press temperature, (2) HIP temperature, (3) air anneal time, and (4) grain size. Two significant trends were observed: (1) light yield decreased with increasing grain size, against previously reported trends [2], and (2) the effect of air annealing time dominated over grain size variation in the range studied here. It should be noted that the four variables presented in Figure 26 on which light yield was dependent may not be independent of each other. In particular, hot-press temperature was used to vary grain size.

In order to interpret the results in Figure 26, we first identified which scintillation regimes were affected by the varied processing parameters. Although the conversion regime is significant to the scintillation process, it should not be affected by microstructure and defects, so additional characterization focused on the migration and recombination regimes, as well as the collection of light after it was produced in the material.

Optical characterization was carried out on the set of four samples with varied grain size obtained through hot-pressing at 1400, 1500, 1600, and 1700°C. In-line optical transmission of samples varied between 43 and 77% at 611 nm (Figure 27(a));

nevertheless, all samples were still highly transparent (see Figure 28). The Eu^{3+} emission peaks in the XRL spectra were not shifted with respect to each other, while the Eu^{3+} absorption peaks were red-shifted in the transmission spectra of the less-transmissive samples (Figure 27(b)). If optical scattering were to have caused the differences in measured light yield between samples, a blue shift in the detected emission peaks would be observed. Since no such shift is present—although optical transmission varied between the set of samples with varied grain size—the variations in light yield observed for these samples did not originate from differences in light collection. This is not surprising because the differences in optical transmission were not large in an absolute sense, and the light collection optics on the XRL detection system were wide. Samples produced using different HIP temperatures and air annealing times (except for the unannealed sample) did not vary in optical transmission.

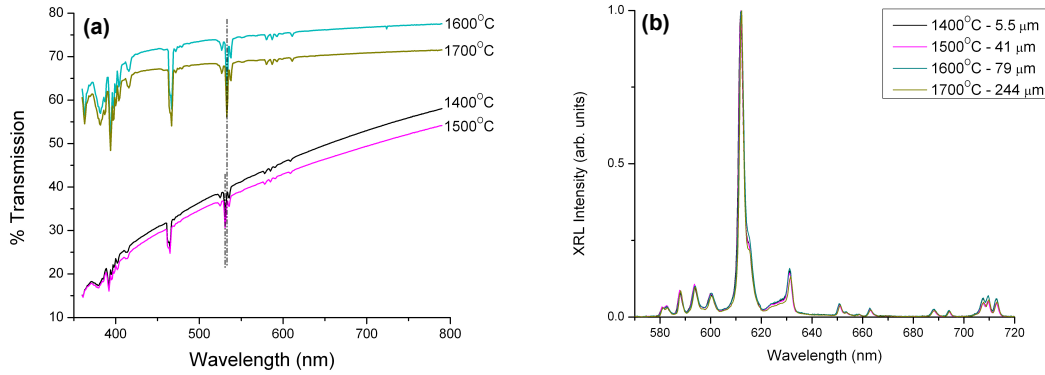


Figure 27: (a) In-line optical transmission and (b) XRL spectra under 50 keVp excitation of 5 at.% $\text{Eu:Y}_2\text{O}_3$ ceramics hot-pressed at varied temperatures.

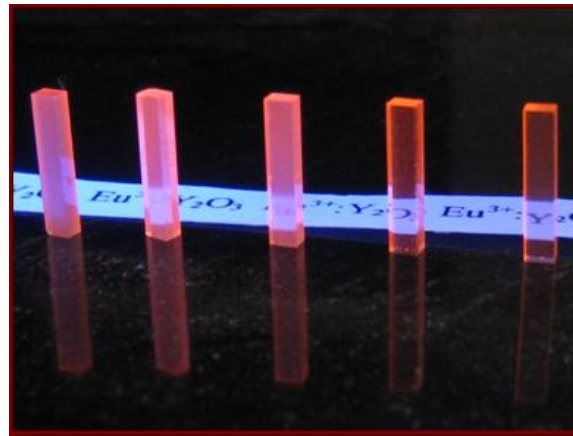


Figure 28: Ceramic samples of $\text{Eu:Y}_2\text{O}_3$ hot-pressed with increasing temperatures and with increasing grain sizes from left to right under ultraviolet irradiation. The far left sample is unannealed.

Because the trend in light yield does not arise from the light collection, recombination or conversion regimes, losses must occur during the migration processes. Migration is affected by trapping or non-radiative recombination at defect levels. The processing parameters that were varied in this study may have affected the concentration and type of traps by varying: (1) the concentration of additional electronic levels associated with abrupt grain boundaries, (2) the concentration of point defects in the bulk of the grains, and/or (3) the overall oxygen defect concentration through diffusion from the air atmosphere. Because the light yield is inversely related to grain size, the first case must not have been the origin of this trend, and grain boundary levels did not dominate the effect on light yield.

In order to investigate whether the hot-press temperature used to vary grain size had an effect on the overall point defect concentration by changing the formation rate of defects that may have been quenched into the ceramic grains, the effect of varying HIP temperature of samples hot-pressed and annealed under the same conditions was studied. The final grain sizes of these samples were found to be relatively constant. This temperature treatment at constant grain size was found to have no effect on light yield (Figure 26(b)). Therefore, the variation in light yield with hot-press temperature is directly correlated with grain size, and only incidentally correlated with temperature. In addition, the effect on charge carrier migration originated from the differences in the overall defect concentration after air annealing between samples with different grain sizes. While this qualitative analysis of the light yield data allowed us to narrow down the effect of grain size to a single mechanism, we were able to relate grain size to the measured light yield based on a charge carrier trapping model and a model for oxygen in-diffusion, according to the quantitative analyses described the follow two subsections.

Thermoluminescence and Trapping Model

The actual depth and concentration of traps in the ceramics identified by a “★” in Table 3 were measured by thermoluminescence spectroscopy (TLS). Oxygen annealing was found to decrease the concentration of deep traps in the ceramics (see Figure 29). These traps must decrease in number due to the re-introduction of oxygen into the material, and therefore are likely related to oxygen vacancy concentration. Oxygen vacancies serve as deep electron traps in Y_2O_3 [70], and thus may compete with electron trapping on Eu^{3+} .

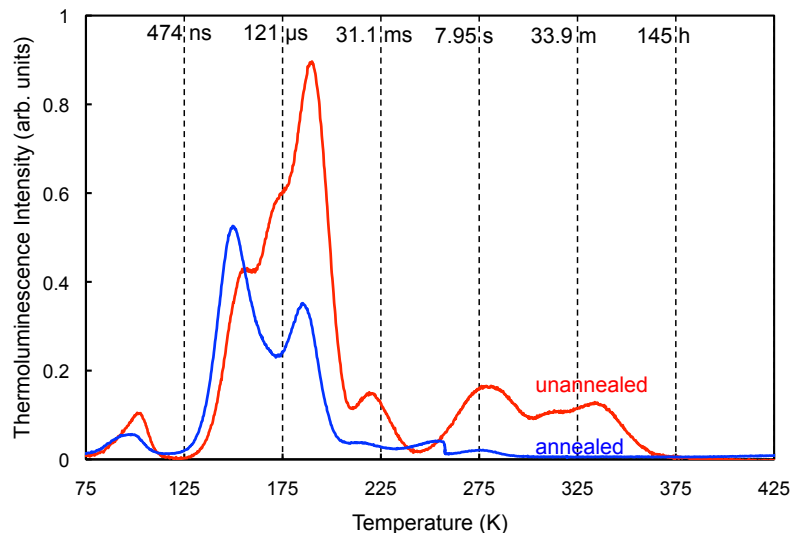


Figure 29: Thermoluminescence (TL) spectra of annealed (blue) and unannealed (red) $\text{Eu:Y}_2\text{O}_3$ ceramics after γ -irradiation at 4K. The time scale at the top of the plot identifies first-order detrapping times.

In order to identify the origin of trapping states associated with air annealing, an unannealed and an annealed ceramic were characterized by electron paramagnetic resonance (EPR) spectroscopy after X-ray irradiation (60 kV, 30 mA) for 20 minutes at 77K. Figure 30 shows the X-ray induced EPR spectra of an annealed and an unannealed $\text{Eu:Y}_2\text{O}_3$ sample. The hyperfine structure observed around $g = 2$ is indicative of electrons trapped at oxygen vacancies near a yttrium ion and holes trapped at yttrium vacancies defects [71,72]. The differential intensity of the microwave absorptions identified as an electron trapped at an oxygen vacancy (on either side of $g = 2$) decreased after air annealing.

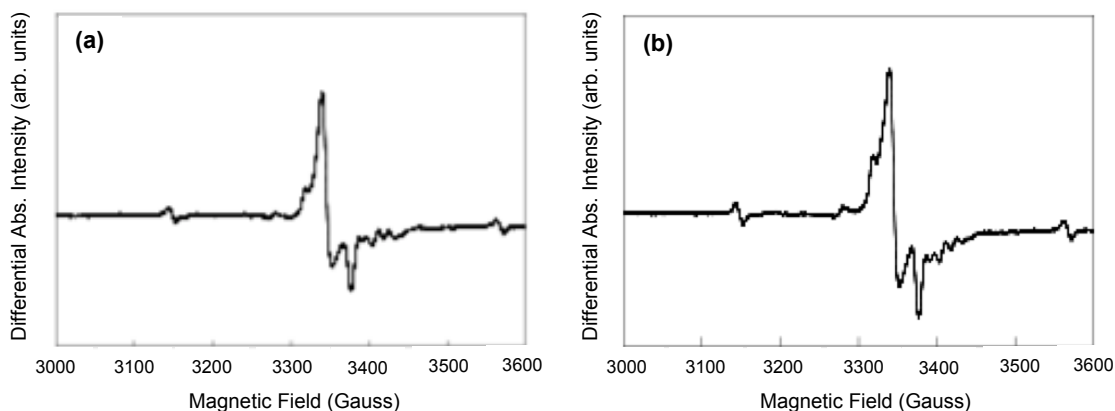


Figure 30: X-ray induced EPR spectra of (a) annealed and (b) unannealed $\text{Eu:Y}_2\text{O}_3$ ceramics.

The kinetics of scintillation are strongly dependent on the concentration and depth of traps [73]. For a single electron trap,

$$\begin{aligned}
\frac{dn}{dt} &\cong 0 = f - npA_r - n(N_{trap} - n_t)A_t + nn_tA_{dt} \\
\frac{dp}{dt} &\cong 0 = f - npA_r - npA_{dt} \\
\frac{dN_{(Eu^{3+})^*}}{dt} &\cong 0 = N_{(Eu^{3+})^*}\tau_r^{-1} - npA_r
\end{aligned} \tag{17}$$

where p and n are the concentrations of free holes and electrons, respectively, $N_{(Eu^{3+})^*}$ is the concentration of excited Eu^{3+} , N_{trap} is the concentration of traps, n_t is the concentration of trapped electrons, t is time, f is the generation rate of electron-hole pairs, A_r is the recombination rate of electron-hole pairs, A_t and A_{dt} are the trapping and detrapping rate of electrons at the trap, and τ_r is the relaxation rate of $(Eu^{3+})^*$.

Light yield may also have a strong dependence on trap concentration:

$$\begin{aligned}
LO/(time * volume) &\cong N_{(Eu^{3+})^*}\tau_r^{-1} \cong npA_r \\
&= \frac{pA_rf}{pA_r + (N_{trap} - n_t)A_t - n_tA_{dt}} \\
\text{For } p &= n + n_t \\
\text{and } N_{trap} - n_t &\approx 0, \\
&= \frac{(n + n_t)A_rf}{A_r(n + n_t) - n_tA_{dt}} = \frac{A_rfn + A_rfn_t}{A_rn + (A_r - A_{dt})n_t}
\end{aligned} \tag{18}$$

Using this simplified model of the effect of a single trap state on light yield, the trend in integrated XRL intensity with air anneal time was evaluated. If the increase in light yield with air anneal time were caused by the decrease in deep-trap concentrations observed in the TLS glow curves, then there should be a strong relationship between the concentration of trapped electrons and the kinetics of oxygen diffusion into $Eu:Y_2O_3$ ceramics.

The earliest (and simplest) analytical models for grain boundary diffusion of atomic species relied on a picture of the boundary as a narrow region with high diffusivity sandwiched between two semi-infinite crystals with lower diffusivity (see inset in Figure 31 for schematic) [74-76]. All solutions to these “bi-crystal” models were based on the set of equations:

$$\frac{\partial C(x,y,t)}{\partial t} = D_L \nabla^2 C(x,y,t) \quad (19)$$

$$\frac{\partial C'(x,y,t)}{\partial t} = D_{gb} \nabla^2 C'(x,y,t) \quad (20)$$

and the boundary conditions:

$$C'(x, \delta/2, t) = C(x, \delta/2, t)$$

$$D_{gb} \frac{\partial C'(x, \delta/2, t)}{\partial x} = D_L \frac{\partial C(x, \delta/2, t)}{\partial x} \quad (21)$$

$$C(0, y, t) = C_0$$

where C and C' are the concentration of the diffusing species in the crystals and the boundary region, respectively, D_L and D_{gb} are the lattice and grain boundary diffusion constants of the diffusing species in the bi-crystal material, δ is the grain boundary thickness, C_0 is the constant species concentration of the source, and t is linear time from the start of diffusion. x and y are Cartesian positions in two-dimensional space, where $x = 0$ is at the interface between the bi-crystal and the source and $y = 0$ is at the center of the grain boundary.

For this system, Levine, et al. [77] and Le Claire [78] derived an analytical expression for the $1/e$ drop-off penetration depth (κ_p), given by:

$$\kappa_p = \left((4D_L)^{1/2} \left(\frac{0.66}{D_{gb} \delta_{gb}} \right) \right)^{-3/5} t^{0.3} \quad (22)$$

where δ_{gb} is the grain boundary thickness and t is the diffusion time. Combining Eqns. 18 and 22 gives a semi-power law relationship:

$$LO = \frac{A - Bt^c}{F - t^c} \quad (23)$$

with generic coefficients A , B , and F , which are dependent on the diffusion and charge carrier rate coefficients. A fit to the light yield of the ceramics that were hot-pressed at 1600°C, HIPed at 1700°C and air annealed for different times, using Eqn. 23, generated an exponent for light yield versus time of $0.334 \pm 1.7E-4$. Samples that were not air annealed showed a broad absorption in the visible, which likely caused re-absorption of the emitted light, thus attenuating light yield considerably more than that caused by trapping alone. Therefore, this ceramic was excluded from the fit. The other coefficients are listed in Table 4, and are physically realistic. The

parameters were calculated, using a least squared fit minimized by the Levenberg-Marquardt algorithm. Parameters were bounded within realistic values in order for the fit to converge. The χ^2 of the fitted function was 0.0188.

The similarity between our experimentally derived coefficient of 0.334 and the coefficient 0.3 of the model implies a relationship between the light yield and the diffusion of oxygen into these ceramics. Therefore, the observed trend in grain size could arise from the lower concentration of grain boundaries available in ceramics with larger grains, which results in longer times to reach thermodynamic equilibrium.

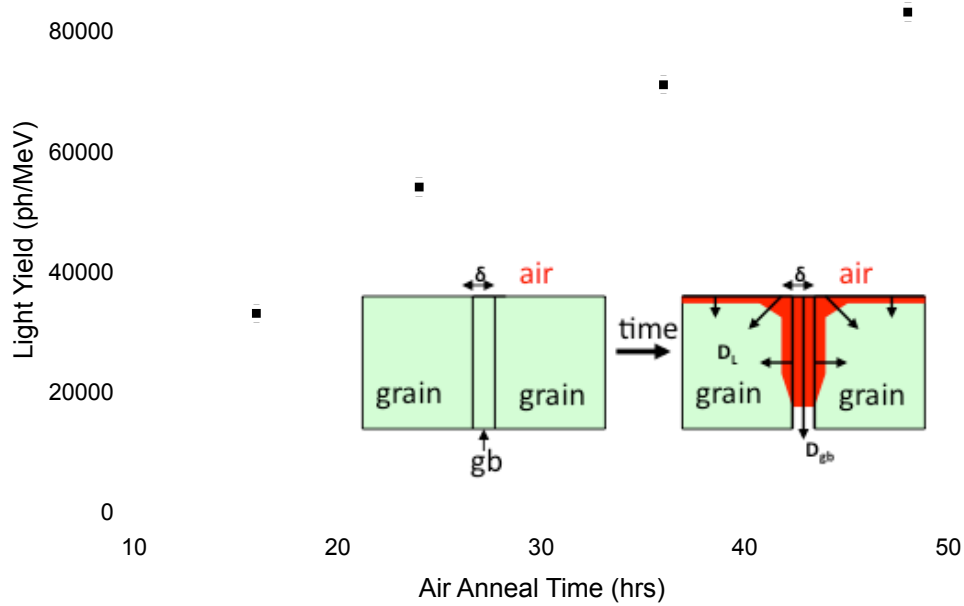


Figure 31: Fit of XRL intensity with varied air anneal time based on the LeClaire model for oxygen diffusion distance. A schematic of diffusion into the semi-infinite bicrystal described by the LeClaire model is shown in the inset.

The similarity between our experimentally derived coefficient of 0.334 and the coefficient 0.3 of the model implies a relationship between the light yield and the diffusion of oxygen into these ceramics. Therefore, the observed trend in grain size could arise from the lower concentration of grain boundaries available in ceramics with larger grains, which results in longer times to reach thermodynamic equilibrium.

Table 4: Fit Parameters for Model for Light Yield of Air Annealed Ceramics

Parameter	Value	Notes
$A \equiv \left(\frac{A_r}{A_r - A_{dt}} \right) \frac{fn}{\left((4D_L)^{1/2} \left(\frac{0.66}{D_{gb}\delta_{gb}} \right) \right)^{-3/5}}$	3.50×10^5	A should be $10^5 - 10^6 \times F$
$B \equiv \left(\frac{A_r}{A_r - A_{dt}} \right) f$	1.6×10^5	$\left(\frac{A_r}{A_r - A_{dt}} \right) \approx 1$ $f \approx 122,600 \text{ pairs/cm}^3\text{s}$
$F \equiv \left(\frac{A_r}{A_r - A_{dt}} \right) \frac{n}{\left((4D_L)^{1/2} \left(\frac{0.66}{D_{gb}\delta_{gb}} \right) \right)^{-3/5}}$	0.801	$A = \frac{BF}{\left(\frac{A_r}{A_r - A_{dt}} \right)}$

Model of Oxygen Diffusion and Light Yield

The diffusion of oxygen into $\text{Eu:Y}_2\text{O}_3$ ceramics is dependent not only on air annealing time (as was described by the model above), but also grain size. If the observed dependence of light yield on grain size were to originate from a difference in the overall concentration of oxygen-dependent traps in the ceramics, we should be able to predict this relationship using an ionic diffusion model that considers grain size as a parameter. The normalized uptake coefficient (NUC) ($\langle M \rangle$) describes the fraction of filled sites in a single-body inside a bath of ionic species according to the ratio [79,80]:

$$\langle M(R,t,T) \rangle = \frac{\iiint_V C(r,t,T) dV}{\iiint_V C(r,\infty,T) dV} \quad (24)$$

where $C(r,t,T)$ is the concentration of species at a radial position r from the center of an object with radius R at time t and temperature T . V is the volume of the object.

Because the ionic diffusion of species into the grain from an infinite, homogeneously-mixed bath at concentration C_0 into an object with radius R satisfies Fick's second law,

$$\frac{\partial C}{\partial t} = D_L \nabla^2 C(r,t) \quad (25)$$

where D_L is the lattice diffusion coefficient of the object and $\nabla^2 = \frac{1}{r^2} \frac{\partial}{\partial r} \left(r^2 \frac{\partial}{\partial r} \right)$ in a spherical coordinate system with only radial concentration variation.

For the boundary conditions:

$$C(R, t \geq 0) = C_0 \quad (26)$$

$$C(0 \leq r < R, t = 0) = C_1 \quad (27)$$

The solution to Eqn. 24 can be written as:

$$\frac{C(r, t) - C_1}{C_0 - C_1} = 1 + \frac{2R}{\pi r} \sum_{n=1}^{\infty} \frac{(-1)^n}{n} \sin\left(\frac{n\pi r}{R}\right) \exp\left(-\frac{D_L n^2 \pi^2 t}{R^2}\right) \quad (28)$$

A more accurate model for the diffusion of species may be derived from the object-bath model with a variable concentration of species in the bath. For this case, the concentration profile is given by:

$$C_\phi(r, t) - C_1 = \frac{2D_L}{rR} \sum_{n=1}^{\infty} \frac{(-1)^n}{n} \exp\left(\frac{D_L n^2 \pi^2 t}{R^2}\right) n\pi \sin\left(\frac{n\pi r}{R}\right) \times \int_0^t \exp\left(\frac{D_L n^2 \pi^2 \lambda}{R^2}\right) \phi(\lambda) d\lambda \quad (29)$$

$$\phi(t) = \langle M(R, t, T) \rangle_{gb} = 1 - 4 \sum_{n=1}^{\infty} \frac{1}{\beta_n^2} \exp\left(-\frac{D_{gb} \beta_n^2 t}{L^2}\right) \quad (30)$$

where β_n is the n th zero of the zeroth-order Bessel function of the first kind, such that $J_0(\beta_n) = 0$.

Numerical solutions to 29 and 30 were calculated for grain sizes and anneal times of ceramics processed in this study. The oxygen lattice diffusion coefficient used for these calculations was based on literature values from diffusion studies in Y_2O_3 single-crystals [81,82]. While the self-diffusion coefficient of oxygen in Y_2O_3 is quite low (on the order of 10^{-12} [82]), and its high-temperature ionic conductivity is limited [83,84], cubic Y_2O_3 can accommodate a large oxygen non-stoichiometry [85] that can significantly enhance the in-diffusion of oxygen from an oxygen-rich atmosphere. Because our experiments rely on air annealing to reintroduce oxygen into our ceramics, the relationship between lattice diffusion and temperature experimentally determined by Berard, et al. [81] was used to calculate oxygen lattice diffusion coefficients for our model. The value of this coefficient for 1150°C was $5.9 \times 10^{-9} \text{ cm}^2/\text{s}$.

The oxygen grain boundary diffusion coefficient (D_{gb}) was determine from oxygen diffusion experiments in the 5 at.% Eu: Y_2O_3 ceramic sample hot-pressed at 1700°C . Ceramics were air annealed at 1150°C , and the distance between the oxidation front

and the surface of the sample (x) was measured. The results of this oxygen diffusion study are shown in Figure 32. The experimental data was fit by to the equation:

$$x = \sqrt{2D_{gb}t} \quad (31)$$

From this fit, a D_{gb} of $3.7 \pm 0.3 \times 10^{-7} \text{ cm}^2/\text{s}$ was calculated. Therefore, the ratio of D_{gb} to D_L was 62.7. Below a ratio of 10^4 , the analytical solution in Eqns. 29 and 30 has previously been shown to fit numerical simulations of atomic diffusion in Voronoi microstructure over all time scales, while above this ratio, intermediate time scales are not well-represented [80].

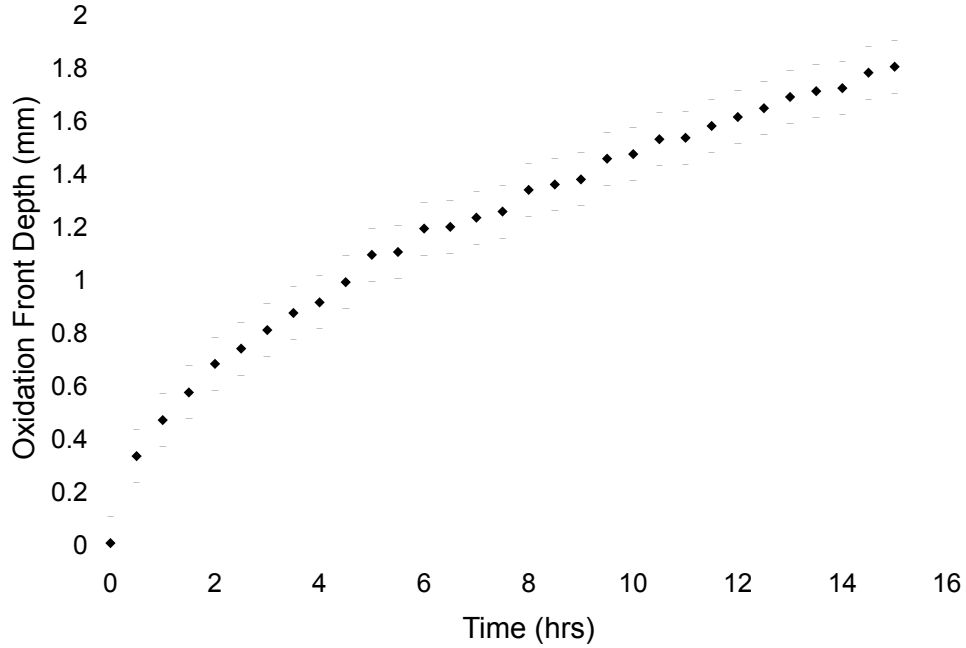


Figure 32: Penetration depth of oxidation front as a function of air anneal time in 5 at.% Eu:Y₂O₃ ceramic. (line) Power law fit from which D_{gb} was calculated.

Results of the NUC are compared to normalized integrated XRL intensity in Figure 33. Calculated NUCs were found to closely follow the normalized light yields measured for our Eu:Y₂O₃ ceramics, further supporting the strong relationship found between the oxygen stoichiometry and scintillation light yield. Additionally, the dominant effect of grain size on light yield does not appear to be caused by trapping states arising from localized distortions at the boundaries. However, for samples with the smallest grain size (5.5 μm), the light yield did not follow the predicted trend. For all air anneal times, the light yields of these ceramics decreased by the same ratio with respect to the ceramic with the next lowest grain size. This trend appears to originate from a different mechanism related to non-radiative recombination or trapping at the boundary, discussed in Section 4.2.

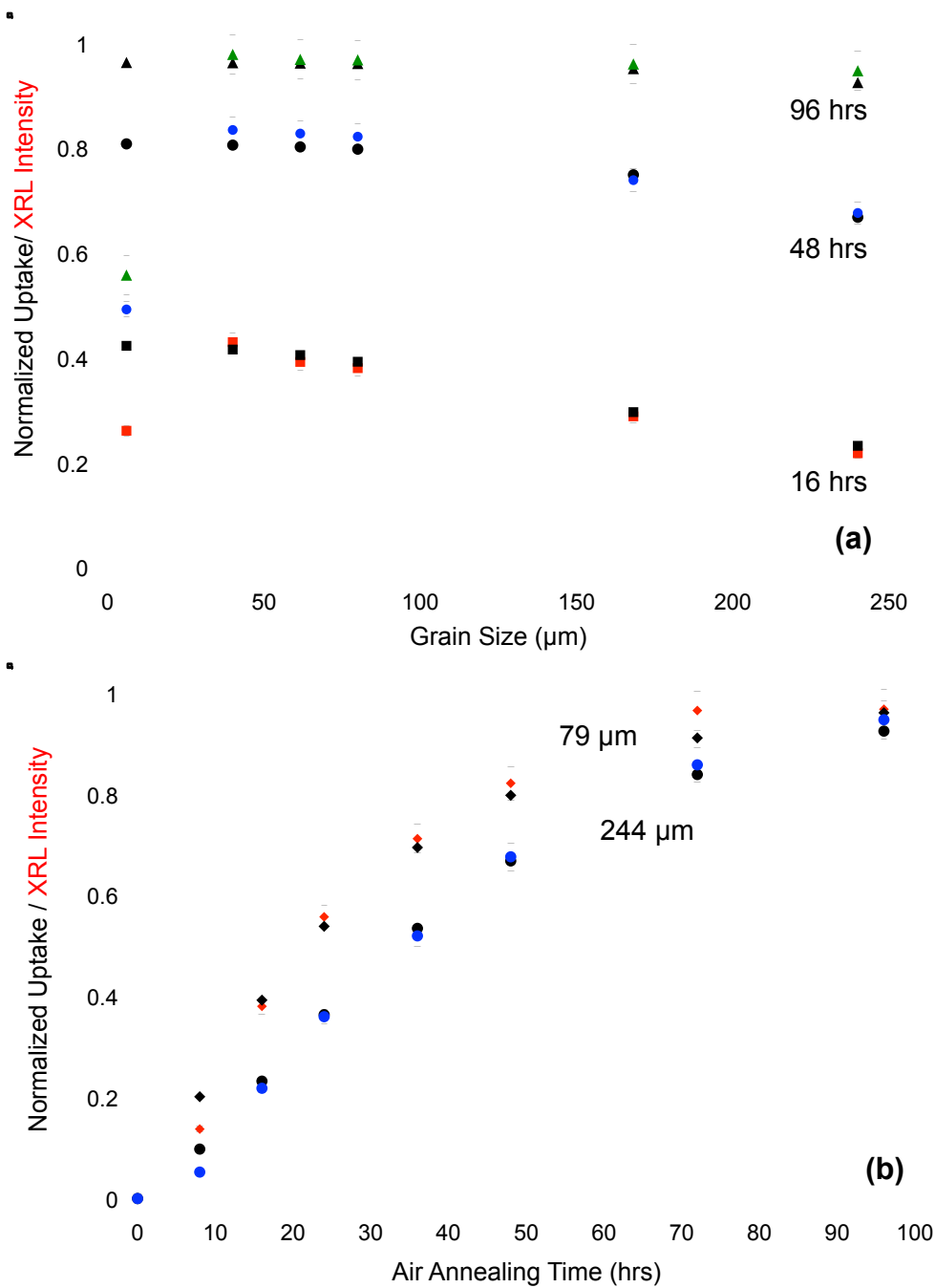


Figure 33: Measured XRL integrated intensity (individual data points) and calculated NUC (data points connected with lines) for (a) ceramics annealed for three different durations with different grain sizes and (b) ceramics with two different grain sizes annealed in air for different times.

For 5 at.% $\text{Eu:Y}_2\text{O}_3$ ceramics with grain sizes ranging from 5 - 250 μm , oxygen non-stoichiometry was the primary cause of variations in light yield between samples. Differences in the total oxygen concentration that had diffused into ceramics lead to different trapping concentrations. A model for the attenuation of light yield by

trapping states due to oxygen in-diffusion was in good agreement with experimental data, indicating that the observed decrease in light yield with grain size arose from oxygen-related defects. Effect from these oxygen-related defects may be mitigated through air annealing and ultimately eliminated after long times (>72 hours at 1150°C), depending on the grain size of the Eu:Y₂O₃ ceramic. The transparency of the samples, however, was optimized after 16 hours of air annealing for all ceramics.

Those studies that have pointed to a relationship between an observed attenuation of light yield and grain boundary-related states [86-88] (for studies on Ce:YAG, Ce:LuAG, and Eu:Lu₂O₃) did not indicate that a set of processing conditions optimized for scintillator performance was used. In our study of Eu:Y₂O₃, optimizing oxygen stoichiometry was quite important to optimizing scintillator performance, but its effect was found to be correlated to the grain size. Our complete study of air annealing and other processing parameters on the light yield of Eu:Y₂O₃ allowed us to distinguish between correlative and causative relationships with grain boundary volume fraction. Without such a study, it would have been easy (but misguided) to attribute our relationship between light yield and grain size to some sort of grain boundary-related defect state.

4.2 Micro-scale Scintillation Characterization Across Grain Boundaries in Ceramic Scintillators

Highlights:

- *Developed a novel micro-scale scintillation technique using focused X-ray excitation to characterize localized scintillation emission.*
- *First determination of effective charge carrier diffusion lengths in insulating scintillator materials, using emission spot maps and charge carrier generation and transport models.*
- *Identified a relationship between charge carrier depletion at grain boundaries and the effect on bulk ceramic light yield.*
- *Proposed a method, based on charge carrier diffusion parameters, for identifying inorganic scintillator materials that may perform more efficiently in ceramic form due to their ability to replenish charge carriers lost to boundary electronic states.*

Experimental Details:

The aforementioned bulk scintillation characterization studies showed that air annealing Eu:Y₂O₃ strongly affected light yield. However, the effect from the grain boundaries themselves appeared minimal, except that is, beyond acting as a diffusion pathway for oxygen. In order to elucidate the previous macro-scale scintillation results presented in section 4.1 and to identify the origin of the difference in light yield seen for the smallest grain sizes, fluorescence microscopy techniques were adapted to investigate local variations in scintillator properties near and away from grain boundaries. As part of these studies, a novel technique involving the use of focused ionizing radiation to stimulate micro-scale light emission was developed. The method was called X-ray radioluminescence microscopy (XRLM).

To verify the results, obtained in the above studies, experiments were performed at the Naval Postgraduate School, using their micro-scale cathodoluminescence characterization method. This was the first time this technique had been applied to insulating scintillator materials. By coupling these two techniques with microstructural and chemical characterization, the true effect of sharp interfaces on scintillator performance within ceramic materials could be definitively determined.

Development of X-Ray Radioluminescence Microscopy (XRLM) Technique

The XRLM studies were conducted using the X-ray microprobe beam line 2-3 at the Stanford Synchrotron Radiation Lightsource (SSRL) (SLAC National Accelerator Laboratory). This beam line provided a focused, monochromatic X-ray beam with spot size <1.2 μm at a flux of $\sim 10^{10}$ photons/sec [89]. The X-ray energy is tunable between 4.5 and 24 keV. The microprobe is both vertically and horizontally focused using Kirkpatrick-Baez X-ray optics. The beam line is primarily used as an X-ray absorption spectroscopy (XAS) imaging station, and also has the capability to perform X-ray fluorescence (XRF) mapping, using a Si Vortex detector. Samples were held vertically in the line of the beam, and were positioned using sample stage translational motors in the X, Y, and Z directions. The sample motors had a positioning precision of 50 nm [89].

An objective microscope equipped with a Photometrics CoolSNAP cf² monochrome charge coupled device (CCD) camera was incorporated into the standard beam line configuration, and visible light optics were used to collect and direct the emission from the sample produced under excitation from the X-ray microprobe. Emission distributions were imaged from the back surfaces of the samples in order to accommodate the optical microscopy setup within the existing configuration inside the hutch. An optical geometry was used such that the real image of the emission distribution was in-focus at the working distance of the microscope objective. A schematic for the XRLM setup is shown in Figure 34.

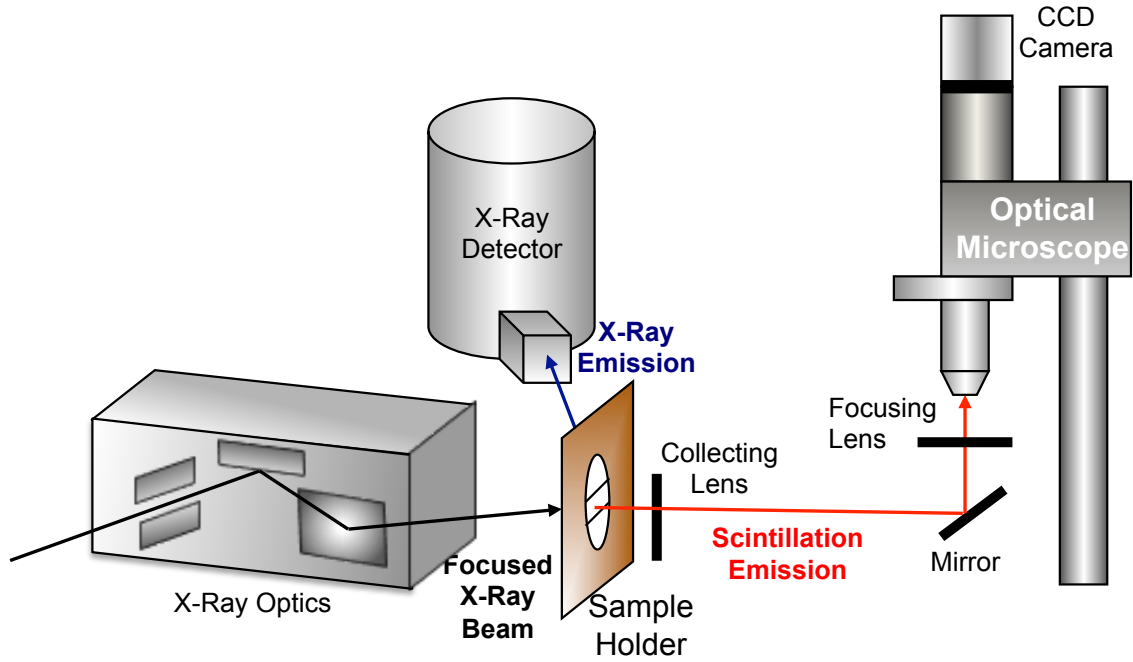


Figure 34: Schematic of XRLM setup.

The CCD imaging array in the camera had 1392×1040 pixels, with each pixel cell $4.65 \times 4.65 \mu\text{m}$, giving a detector resolution of 310 nm at a microscope magnification of $15\times$. However, the numerical aperture of the objective limited the lateral spatial resolution of the microscope, such that its Abbe diffraction-limit was between 325 and 527 nm for wavelengths between 400 and 650 nm. Therefore, there was minimal light bleeding between pixels. The aperture in front of the collection lens provided a depth of field (DOF) between 14.8 and $24.1 \mu\text{m}$ in this same range of wavelengths. This DOF is nearly the thickness of the samples, so that the microscope was in focus at all depths through each sample. A smaller DOF could be achieved by removing the aperture in front of the collection lens.

In order to verify that the XRLM technique could be used to measure charge carrier transport behavior, the diffusion length (L_{diff}) of a $\sim 5\text{-}\mu\text{m}$ thick film of epitaxial GaAs on Ge with known properties was calculated from its emission distribution. The GaAs/Ge sample was thinned from the substrate surface down to $\sim 20 \mu\text{m}$ and the GaAs surface was directed towards the collection lens so that its visible emission would not be absorbed within the Ge substrate layer before reaching the optical microscope. Emission spots were imaged at 15 locations within the sample, and the tails of the average emission distribution were fitted to a zeroth-order Bessel function of the second kind (\mathbf{K}_0), using a procedure described in Section 4.3.4, with L_{diff} as a fitting parameter, as shown in Figure 35. The calculated diffusion length of $17.5 \pm 0.4 \mu\text{m}$ is in good agreement with previously reported values ($L_{diff} = 17.1 \mu\text{m}$ [90]).

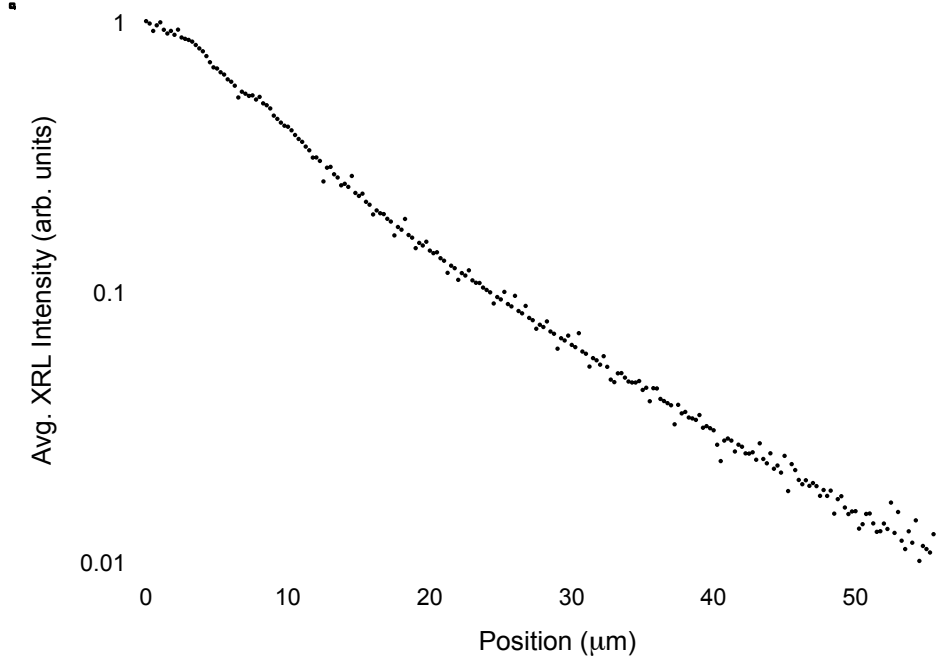


Figure 35: Average X-ray radioluminescence (XRL) intensity (black dots) of epitaxial GaAs on Ge as a function of distance from the center of the 8.1 keV X-ray excitation beam. The red line shows the fit of the emission distribution tail using a K_0 function in order to calculate L_{diff} .

Two $\text{Eu:Y}_2\text{O}_3$ ceramics were characterized by XRLM. Both were hot-pressed at a temperature of 1600°C and pressure of 40 MPa. However, the ceramic sample labeled “Y01,” was sintered with a single ramp up to the maximum pressure after outgassing at 1150°C . In the case of sample “Y02,” the temperature and pressure were ramped up step-wise during sintering. The total sintering times of ceramics Y01 and Y02 were 16 and 25 hours, respectively. Both ceramics were HIPed in argon at 1700°C for 2 hours at 200 MPa, and then air annealed at 1150°C for 72 hours.

In addition to the yttrium oxide samples described above, two 0.1 at.% Ce:YAG samples were also characterized by XRLM in order to verify that the technique and charge carrier transport models used to determine materials parameters were both accurate. The first was a bicrystal made by pressure bonding two single-crystals together, the other a Ce:YAG ceramic. These results are discussed below, following the results on $\text{Eu:Y}_2\text{O}_3$ ceramics.

All samples were ground and polished to below a single-grain thickness ($\sim 20\ \mu\text{m}$) and mounted on a copper foil in preparation for XRLM measurements. Samples were thinned to avoid interactions with multiple boundaries and to limit the effect of scattering from any residual porosity. An image of a thinned sample of $\text{Eu:Y}_2\text{O}_3$ and a typical XRLM emission spot from the sample are shown in Figure 36.

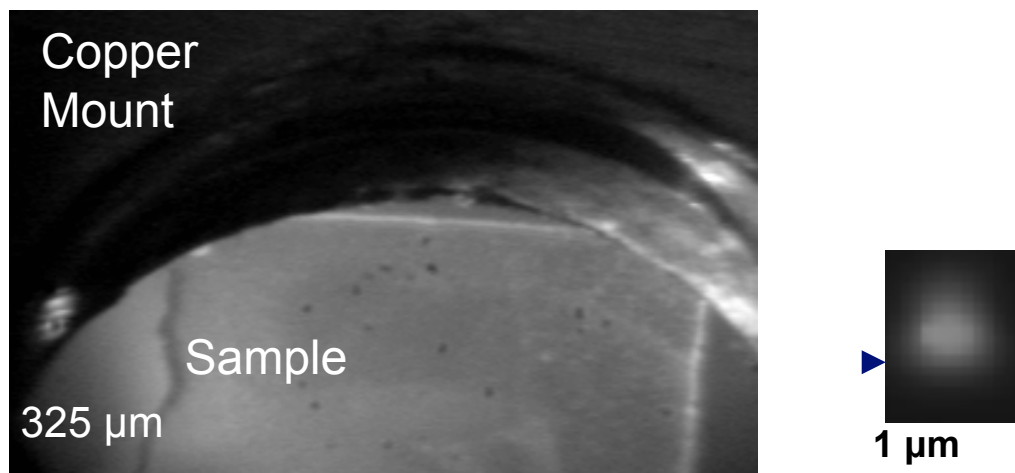


Figure 36: CCD images of thinned YO1 Eu:Y₂O₃ sample at low magnification and typical XRL emission spot at high magnification. The thinned sample was under backlight when the low magnification image was taken. The image of the thinned sample shows the sample mounted over a hole in a copper foil. The black dots on the sample are aberrations from dust and imperfections in the backlight.

Radioluminescence across Grain Boundaries in Eu:Y₂O₃

Scintillation emission intensities were measured in the ceramics and bicrystal by incrementally moving the sample along the vertical (Z) axis by 0.25 μm, so that the X-ray beam was focused on a series of spots along ~14-μm lines crossing boundaries. At each spot, 45 images of the emission distribution were acquired.

The normalized peak XRL intensities plotted in Figure 37 were calculated from images of emission distributions. The maximum intensities of the measured distributions in all of the images taken at each spot were averaged and then normalized to the average value at the beginning of each line (nominal position = 0 μm). The error bars on each maximum of an XRL intensity signify the 95% confidence interval of its mean value.

Figure 37(a) shows the normalized peak XRL intensity under 8.1 keV focused excitation centered at spots along the 10.5 μm line identified in Figure 37(c). The line crossed the grain boundary indicated by the arrow, which coincided with the position 4.25 μm in Figure 37(a). Other than at this position, the trend in peak XRL intensity followed the change in Eu concentration. Because the Eu concentration varied from ~4.5 mol.% to ~5.5 mol.% in this area of the sample, and the light yield of Eu³⁺:Y₂O₃ has been shown to vary roughly linearly with concentration over this concentration range [91], the overall trend in maximum XRL intensity with position likely originated from the difference in Eu³⁺ along the line.

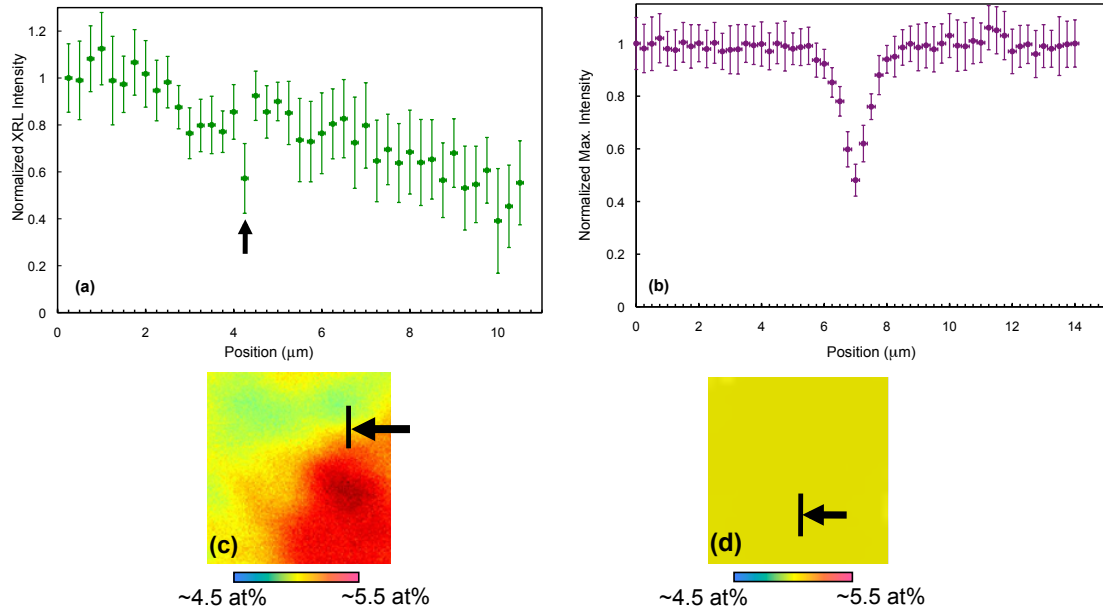


Figure 37: Peak XRL emission intensity at positions 0.25 μm apart from each other along lines that cross a boundary in samples (a) Y01 and (b) Y02. Intensities were normalized to the initial point on the line. Figures c and d show XRF maps of Eu in Y01 and for Eu in Y02 respectively. The line in (c) shows where the data in (a) was taken and the line in (d) the data from (b). The arrows in (c) and (d) identify the boundaries at the positions of 4.25 μm in (a) and 7 μm in (b), respectively.

In contrast, the depletion regions in Y02 were much more distinctive than that observed in Y01. Significant depletion was found over a region $\sim 1 \mu\text{m}$ wide, and clear depletion began to occur over a region $\sim 2 \mu\text{m}$ wide, as illustrated in Figure 37(b). The effect of Eu concentration gradients within Y01 on local emission intensity largely obscured any effect of the boundary, such as that observed in Y02, beyond a narrow width right at the boundary.

In previous studies, a difference in the emission intensity or conductivity at grain boundaries, such as the ones observed here, has been variously attributed to: (1) a decrease in material thickness due to grain boundary grooving at the surfaces [92], (2) light channeling due to a difference in refractive index across a boundary [93], (3) excited state quenching of activator ions from defect states at the boundary [94,95], and/or (4) depletion of charge carriers at boundary states prior to recombination at luminescent centers [96-101]. Through an analysis of previous literature, and chemical and structural characterization of the ceramics studied by XRLM, effect 4 was found to cause the observed decrease in XRL intensity at the grain boundaries. Transmission electron microscopy (TEM), nanometric secondary ion mass spectroscopy (NanoSIMS), and fluorescence confocal laser scanning microscopy results are briefly discussed below, but for further discussion see Ref. 102.

Figure 38 shows a TEM image of a typical grain boundary in the region of the sample used for XRLM characterization. The ~ 5 nm width of the boundary in the image appears to be a region of overlap between the two grains on either side of the boundary, since the lattice fringes of each of the grains extend through the region. Within a ~ 10 nm region, starting at the boundary, the lattice parameter is slightly distorted. This is possibly due to a very low concentration of line defects that were present within this sample ($<\sim 10/\text{grain}$) (Figure 38(inset)). They were typically close to the edge of the distorted region, but also present within the bulk of the grain and may indicate a segregation of dislocations right near the boundary, which may occur due to a decrease in their energetics of formation near the boundary. However, while some disorder in the crystalline structure was observed near the boundaries, there still was a strong crystalline order at the boundary, and any increased concentration of structural defects was within a very limited width around it. Although additional electronic states from these structural defects may serve as trapping and non-radiative recombination centers [103], their localized concentration extended over only 1/100th of the width of the scintillation intensity depletion region measured by XRLM. Therefore, any effect that this boundary disorder may have on scintillation need not be considered in addition to any the effect of an abrupt boundary, considering its narrow spatial scale.

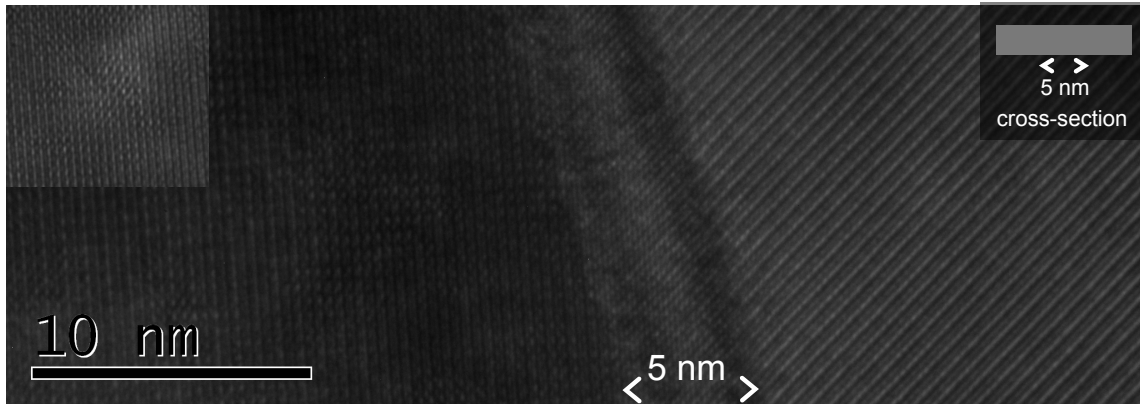


Figure 38: TEM image of grain boundary in Eu:Y₂O₃ ceramic, showing lattice fringes of both grains that extend through the ~ 5 nm overlap near the boundary between the two grains. (inset) TEM image of typical dislocation loop.

While there may be limited structural disorder near the grain boundaries in the YO₂ sample, chemical segregation may still occur at these boundaries, and may cause differences in scintillation emission. SIMS measurements showed no preferential segregation of Eu or other impurities at grain boundaries. Figure 39 shows a typical line profile for Eu and some other impurities across a grain boundary.

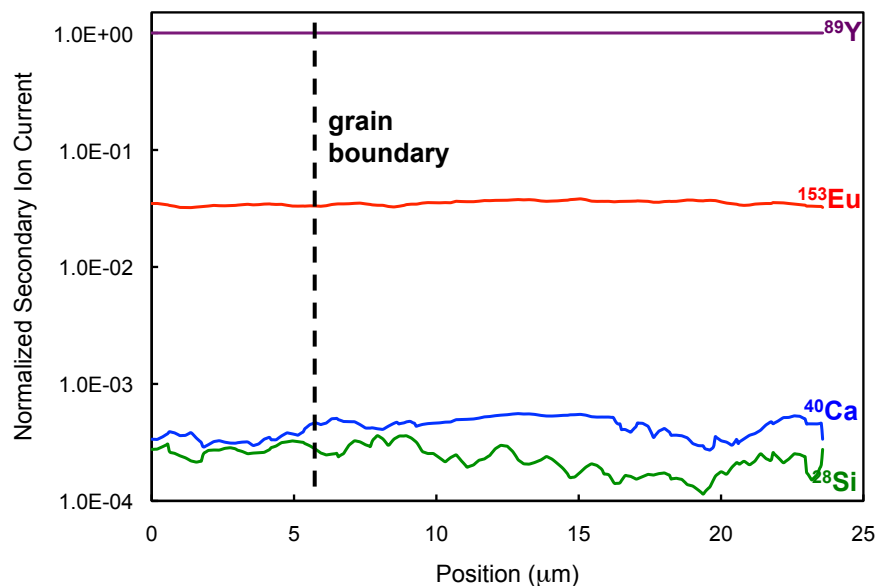


Figure 39: Secondary ion mass spectrometry (SIMS) line profile across a grain boundary for ^{89}Y , ^{153}Eu , ^{40}Ca , and ^{28}Si . Ion currents are normalized to that of ^{89}Y at each position. The position of the grain boundary is indicated by the dashed line.

Figure 40 shows a confocal microscope image of the 611 nm emission of the YO2 sample under excitation from an argon laser. At this wavelength the ^5D multiplet of Eu^{3+} is excited. The emission intensity was found to vary only at the boundaries. Also, the emission spectrum did not shift across the boundary. Therefore, the decrease in emission intensity observed at the grain boundaries by direct excitation of Eu^{3+} was not as wide as that measured by XRLM, making excited state quenching of activator ions an unlikely source of the depletion. It is worth noting that concentration quenching was not even observed in $\text{Eu}:\text{Y}_2\text{O}_3$ ceramic YO1, where the local Eu concentrations never reached above ~ 5.5 at.%, which is below the Eu concentration at which quenching has been reported [104].

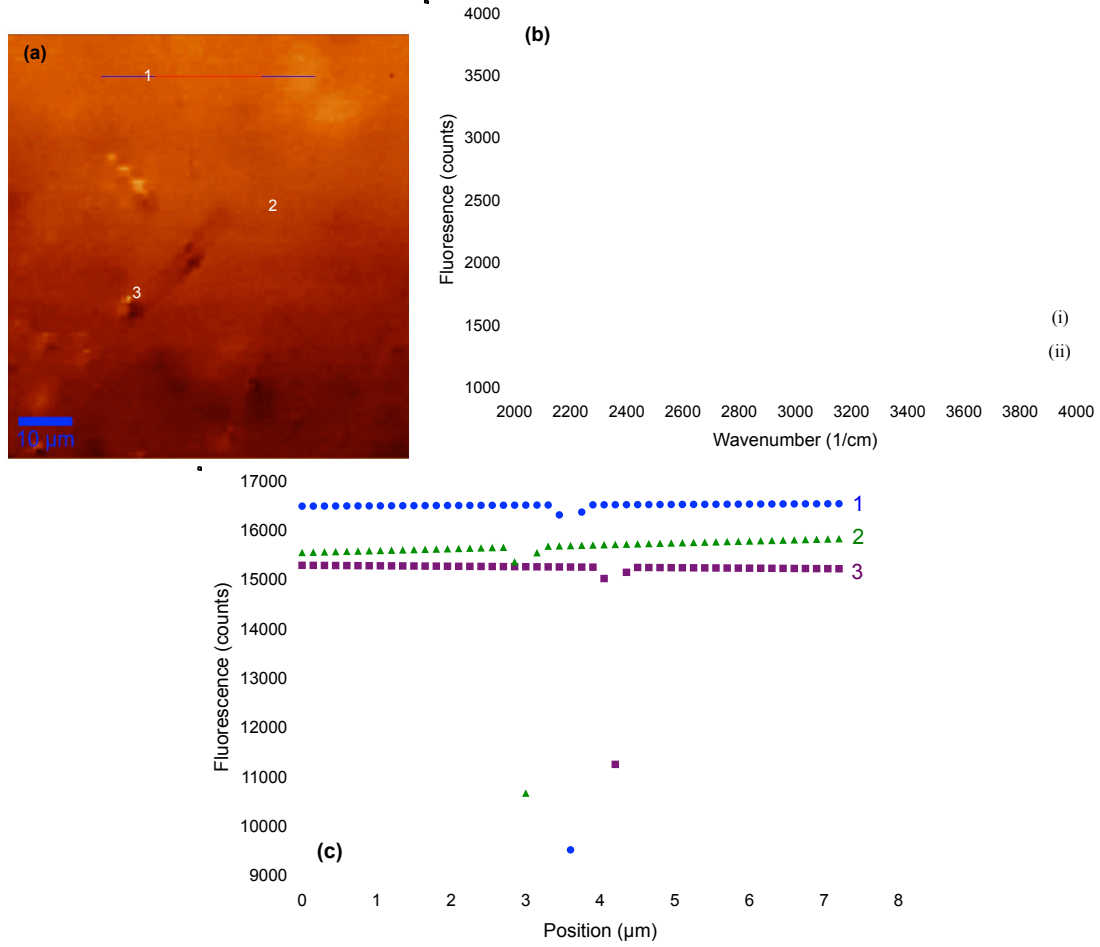


Figure 40: (a) Scanning fluorescence confocal microscopy image of 611 nm emission from Eu³⁺ at a depth of 5 μm in Eu:Y₂O₃ ceramic YO₂ under 488 nm excitation. (b) Eu³⁺ fluorescence spectra at point (i) at grain boundary (ii) away from grain boundary; no peak shifts were observed. (c) Fluorescence intensity line profiles of the three lines crossing grain boundaries marked in the confocal image in (a).

Calculation of Boundary Recombination Velocities using a Charge Carrier Transport Model

The experimental results presented above showed that charge carrier depletion at electronic defect states located in the immediate vicinity of the boundary led to the decrease in XRL intensity. To verify this effect, a charge carrier transport model was used, as discussed in this section. Using this model with experimentally measured transport parameters, the “boundary recombination velocities” were calculated by fitting simulated XRL profiles to the measured data. This method quantified the effect of the grain boundaries on XRL intensity.

The spatial extent of an emission distribution represents the volume over which charge carriers are generated and subsequently transported before radiatively

recombining at activator ions or other radiative sites within the host material. Thus, the distributions measured in this study provided information on the nature of both charge carrier generation and transport. Generally, the spatial distribution of free carriers within a material under steady-state, ionizing excitation can be described by the continuity equation:

$$D\nabla^2 n - \frac{n}{\tau} + S(\mathbf{r}) = 0 \quad (32)$$

where D is the diffusion coefficient of the charge carrier of interest (i.e., electron, hole, ambipolar, exciton), n is the charge carrier concentration, τ is the lifetime of the carrier, and $S(\mathbf{r})$ is a spatially-dependent carrier source term. Similar charge carrier diffusion models have been used extensively to describe conductivity in semiconductors ever since the results of the Haynes-Shockley experiment were reported [105].

In its time-dependent form, Eqn. 32 has also been used to describe the kinetics of emission from photoelectric semiconductor materials [106-109], where the emission intensity is assumed to be proportional to the minority charge carrier concentration. A similar approach can be used to describe the transport of charge carriers in inorganic, insulating materials excited by ionizing radiation (such as the scintillator materials investigated here) [110-112].

With a radially-symmetric, Gaussian source term and no imposed boundary conditions, and when $r \gg \sigma$, where σ is the standard deviation of the source, (i.e., a couple of microns from the source), Eqn. 32 can be approximated [113] as:

$$I(r) \propto \mathbf{K}_0(r/L_{diff}) \quad (33)$$

where L_{diff} is the effective diffusion length and \mathbf{K}_0 is the zeroth-order modified Bessel function of the second kind. Therefore, L_{diff} may be calculated by fitting the tail of an emission distribution with a \mathbf{K}_0 function. The effective diffusion coefficient in Eqn. 32 may then be experimentally determined from calculated values of L_{diff} and the measured scintillation decay times (τ), using:

$$D = \frac{L_{diff}^2}{\tau} \quad (34)$$

To understand the physical parameters associated with the observed emission intensity depletion in the boundary region, a boundary condition that could account for the effect of sink states (deep traps and non-radiative recombination centers) was used to simulate emission distributions in the Eu:Y₂O₃ samples. Because limited segregation of dopants, impurities and structural defects was observed at the

boundaries in these materials, an abrupt boundary condition was found to be an appropriate assumption. The boundary condition [114]:

$$\bar{n} \cdot \nabla I = \frac{I}{D/s} \quad (35)$$

was used to account for rate-limited, non-radiative recombination at a boundary surface, where s is the boundary recombination velocity, and \bar{n} is the unit vector normal to the boundary. As discussed below, calculated values for s , based on solutions to Eqns. 32 and 35, were used to quantify the effect of a nearly abrupt boundary on the depletion of nearby charge carriers.

The effective charge carrier diffusion lengths were calculated from averaged XRL emission distributions (Table 5). The average distributions were constructed from 10 cross-sections of a distribution averaged over 1,800 images of emissions from each of the samples (45 images taken at each of 40 different locations). Each emission profile consisted of three regions: (1) one that decreased faster than exponential, (2) a second that decreased nearly exponentially (the linear section on the log-linear plot), and (3) a third at the detection limit below the level of background. Because the Gaussian tails of the X-ray source distribution fall off faster than exponential, the exponential-like “tails” that arise from transport of charge carriers generated within the extremes of the Gaussian source volume were easily identified. These tails were fit with a K_0 function (an exponential-like function), using a least-squares fitting method to determine L_{diff} , according to the relationship in Eqn. 33 (see Figure 41 for an example profile and fit).

Table 5: Measured Effective Diffusion Lengths and Decay Times

Sample	Effective Diffusion Length (μm)	Boundary Recombination Velocity (cm/s)	Decay Time (ms)	Percentage of Total Decay
Eu:Y ₂ O ₃ Ceramic Y01	1.47 ± 0.14	---	0.983	93%
Eu:Y ₂ O ₃ Ceramic Y02	1.56 ± 0.09	4,500	0.978	95%

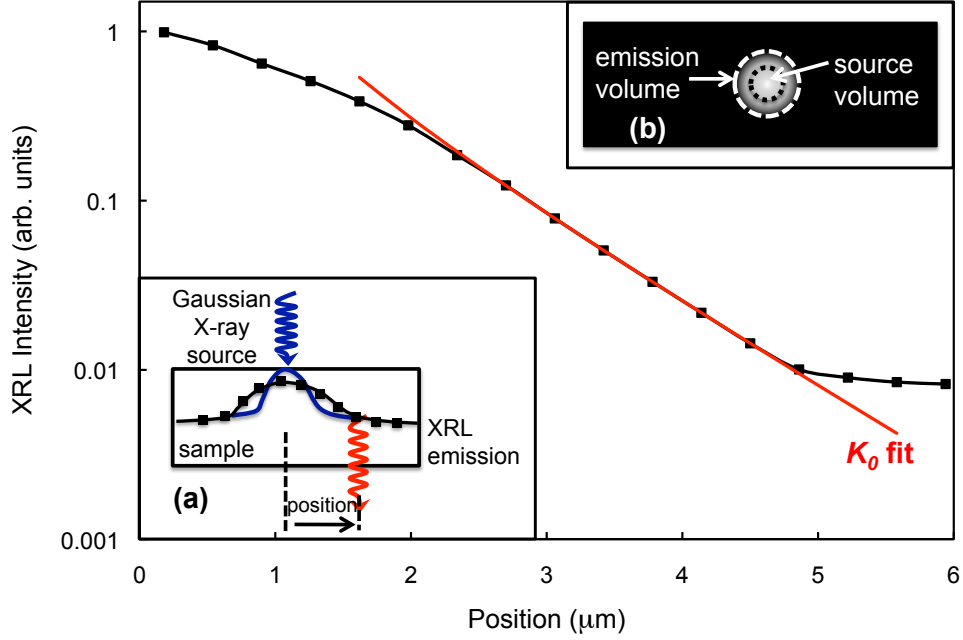


Figure 41: Typical XRL emission profile. The black squares plot the intensities at each pixel averaged over images of emission from excitations at a number of different spots. Inset (a) shows a schematic of the technique used to measure profiles. Inset (b) illustrates the contribution of the source volume to the total emission volume.

Effective charge carrier lifetimes (τ) were calculated from bulk scintillation emission decay after γ -excitation (Table 5). In the cases where multiple decay components were observed, an effective τ was calculated based on the relative contributions of the components. The decay in scintillation intensity with time represents the probability that charge carriers radiatively recombine at a given time after their generation. The decay time expresses the exponential fall-off rate of this probability. Trapping and non-radiative recombination affect the probability of radiative recombination within a given time window, and therefore effect the values of decay time [115,116]. Under the high-flux, steady-state excitation conditions used in these experiments, activator ions can be continuously populated, so that the relaxation rate significantly affects the time (and equivalently the distance) over which a charge carrier must hop until it finds a free activator ion. Therefore, scintillation decay times can be used as a measure of the effective charge carrier lifetimes of interest in this study.

Before calculating values of s , it was first confirmed (by fitting solutions to the diffusion equation (Eqn. 33) with the appropriate boundary condition (Eqn. 35) to XRLM data) that both charge carrier generation and transport could be effectively modeled. For a further discussion of these studies, see Ref. 102.

A two-dimensional, Gaussian source term centered at point (x_0, y_0) , as expressed by:

$$S(x, y) = \exp\left(-\frac{(x - x_0)^2 + (y - y_0)^2}{2\sigma^2}\right) \quad (36)$$

was used for the emission distribution models. The PDE was solved over a 525,313 node mesh within a circular area with a diameter of 75 μm . The standard deviation (σ) of $S(x,y)$ was calculated through the convolution of a Gaussian X-ray source with the interaction volumes of a single collimated X-ray. These calculations only take into account sequential photoelectron emission (i.e., the low energy limit) from the element with the largest photoelectric interaction cross-section. The three-dimensional distributions of the energy deposited by photoelectrons in 103-nm³ bins were modeled using the CASINO 2.42 software package [117]. These distributions were then integrated over the sample thickness to produce a two-dimensional distribution of the energy deposited by each photoelectron. The convolution of the sum of the Gaussians from the possible photoelectron energies (i.e., photoelectrons excited by either the primary X-ray or X-ray fluorescence from the relaxation of electrons to cores energy levels in Eu, Y, or O) was fit by a Gaussian function to determine the σ of the excitation source, i.e., the initial distribution of charge carriers with energies below the threshold for photoelectric interactions (set to <50 eV here).

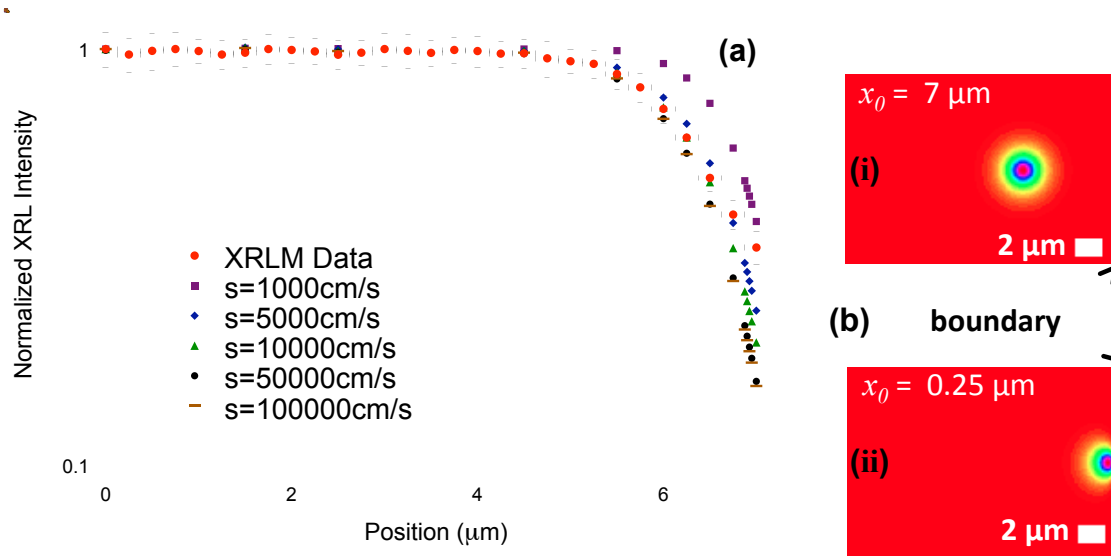


Figure 42: Experimental and simulated XRL intensities at different excitation spots within 7 μm of a boundary. The boundary was located at the 7 μm position on the plot. Five simulated line profiles are shown in (a) with different boundary recombination velocities (s), along with XRLM data. The intensity maps in (b) show the simulated distributions in two-dimensional space with the boundary condition in Eqn. 3.5 at the right-hand surface of the figures and an $s = 10,000 \text{ cm/s}$ for identical Gaussian excitations centered at (i) 7 μm and (ii) 0.25 μm from the boundary. The hue-saturation-value of the colormaps in (b) was normalized with respect to the maximum intensity of the individual distributions.

Figure 42 shows the maximum intensity of the simulated XRL distributions for the Eu:Y₂O₃ ceramic Y01 excited by a 8.1 keV Gaussian source centered at different

positions with respect to a boundary located at $7\text{ }\mu\text{m}$ in the figure. The position (x_0, y_0) was varied to simulate the spot by spot excitations measured by XRLM. Solutions were plotted for a number of different values of s for the boundary condition in Eqn. 35 and were compared to the XRLM data across a boundary. Boundary recombination velocities for the measured grain boundaries were determined by comparing XRLM results with simulated emission spot intensities for different values of s . Table 5 shows the values of s calculated using this method.

Extension to Bulk XRL Intensity of Eu:Y₂O₃ Ceramics

Figure 43 shows effect of grain size on XRL intensity in Eu:Y₂O₃ ceramics. Values of bulk XRL intensity were calculated from numerical solutions to Eqns. 32, 35, and 36, using the effective diffusion lengths and recombination velocities from Table 5. An intensity map of one such solution with a grain size of $30\text{ }\mu\text{m}$ is shown in Figure 43(b). These values were compared to the measured Eu:Y₂O₃ ceramic light yields reported in Section 4.1.

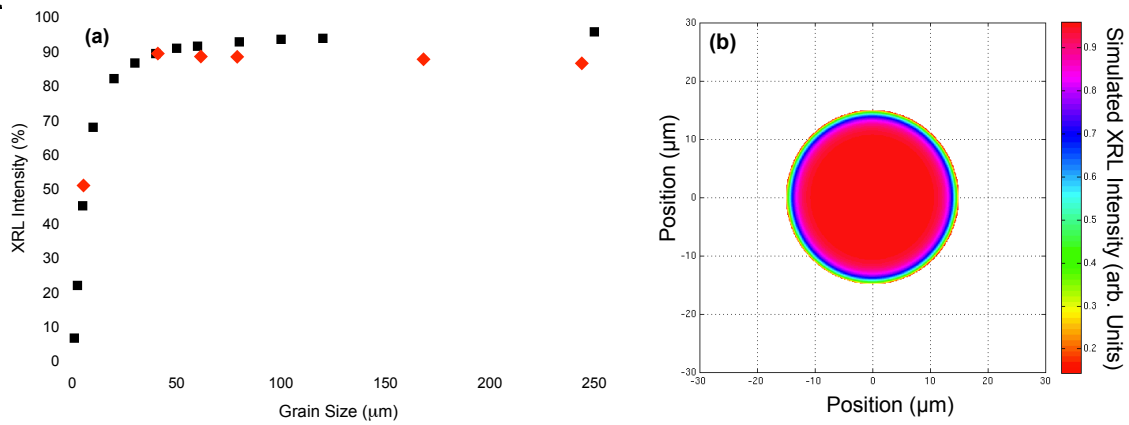


Figure 43: (a) Normalized bulk XRL intensities as a function of ceramic grain size for Eu:Y₂O₃. Values were normalized to a solution with a grain size of $500\text{ }\mu\text{m}$. Black squares are simulated values and red diamonds experimental data. Numerical solutions to Eqn. 33 with a homogeneous source term over the entire grain and with boundary condition in Eqn. 35 at circular boundaries with different radii were integrated over the entire solution space to calculate the XRL intensity. A recombination velocity of $s = 4,500\text{ cm/s}$ (the measured value for Y₂O₃) was used. (b) Example of a simulated intensity distribution in two-dimensional space for the bulk excitation of a ceramic grain.

In order to minimize the effect of oxygen non-stoichiometry described in the previous chapter, only ceramics air annealed for 96 hours were compared to these predicted values. The prediction agreed well for Eu:Y₂O₃ ceramics having similar grain sizes. For example, our model predicted a relative luminosity of 58% for a $5.5\text{ }\mu\text{m}$ grain size ceramic and 63% for a ceramic with $34.1\text{ }\mu\text{m}$ grains

At larger grain sizes ($>50\text{ }\mu\text{m}$), the effect of oxygen non-stoichiometry began to have a significant effect on light yield, and therefore resulted in a deviation between measured and predicted values. These results were also found valid for powders. $\text{Eu:Y}_2\text{O}_3$ powder with a particle size of 60 nm was found to have $\sim 10\%$ of the emission intensity of ceramics with $2\text{ }\mu\text{m}$ grain size [118,119], for which a $\sim 5\%$ relative luminosity is predicted.

Comparison of X-Ray Radioluminescence across Boundaries in $\text{Eu:Y}_2\text{O}_3$ and Ce:YAG Ceramics

To study how grain boundaries affect scintillation behavior in different materials, the $\text{Eu:Y}_2\text{O}_3$ ceramics were compared to both a $\text{Ce:Y}_3\text{Al}_5\text{O}_{12}$ (Ce:YAG) ceramic and a bicrystal using the XRLM method. The Ce:YAG transparent ceramic was produced by vacuum sintering of mixed oxide powders, and the Ce:YAG bicrystal was produced through pressure bonding two parts of a cut single-crystal back together.

The peak XRL intensities in the Ce:YAG bicrystal (Figure 44(a)) and ceramic (Figure 44(b)) had a similar shape to that of $\text{Eu:Y}_2\text{O}_3$ ceramic YO2. The boundaries characterized in the Ce:YAG samples had very similar widths ($\sim 2 - 2.5\text{ }\mu\text{m}$) and depths ($30 - 35\%$) compared to each other, but were wider than and deeper than the boundaries found in YO2. The similarity between the Ce:YAG bicrystal and ceramic indicates that the bicrystal boundary may be a good model for a ceramic grain boundary in this context, and that there is no significant additional effect from surface damage during polishing of the crystals before bonding.

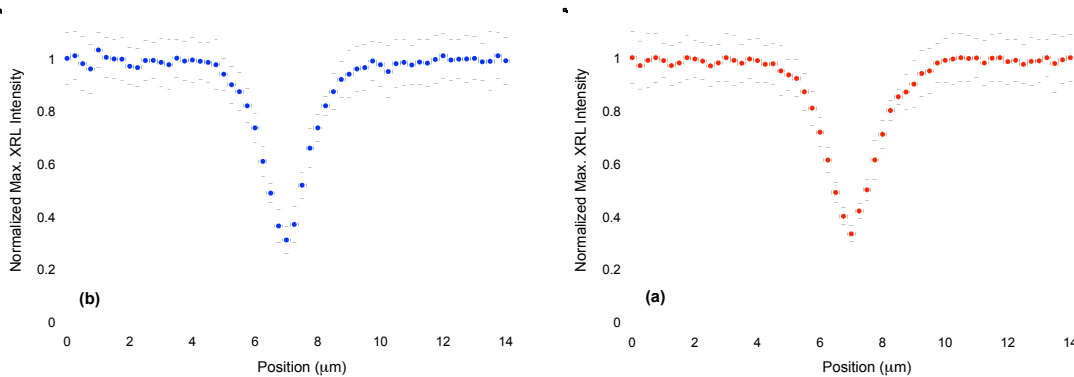


Figure 44: Peak XRL intensity of emission spots excited at positions $0.25\text{ }\mu\text{m}$ apart from each other along lines that cross a boundary in a Ce:YAG (a) bicrystal and (b) ceramic. Intensities were normalized to the initial point on the line.

Effective charge carrier diffusion lengths and decay times were also determined for the Ce:YAG samples and are shown in Table 6.

Table 6: Measured Effective Diffusion Lengths and Decay Times in Ce:YAG

Sample	Effective Diffusion Length (μm)	Boundary Recombination Velocity (cm/s)	Decay Time (ns)	Percentage of Total Decay
Ce:YAG bicrystal	0.98 ± 0.03	8,500	82	79%
			394	28%
Ce:YAG ceramic	0.89 ± 0.07	8,900	73	71%
			578	11%

Based on the above results, a number of important trends were observed:

1. As boundary recombination velocity increases, changes in the width and depth of the depletion region became less pronounced for a given effective diffusion coefficient. Therefore, there is little effect on the total XRL intensity from defects (e.g. traps and non-radiative recombination sites) beyond a certain concentration or rate of trapping on such sites in the immediate vicinity of a boundary. This may in part explain the minimal differences observed in the depletion regions measured across different boundaries in the same ceramic, even though the crystalline orientation of grains was random.

2. Both the recombination velocity at the boundary and the flux rate at which charge carriers can diffuse to the boundary affected the characteristics of the depletion region. Such a mechanism preserves local thermodynamic equilibrium, and is dependent on transport properties both at the boundary and within the bulk of the grains. Therefore, while the recombination velocities of the $\text{Eu:Y}_2\text{O}_3$ (4500 cm/s) and Ce:YAG ceramics (8900 cm/s) in this study were similar, their depletion widths and depths were quite different.

3. Even though the D/s -ratio for $\text{Eu:Y}_2\text{O}_3$ was nearly four orders of magnitude smaller than that of Ce:YAG, its much smaller D led to a smaller charge carrier flux rate in response to the same concentration gradient.. This results in a smaller depletion region. In this way, the transport properties within the bulk of the grains play a significant role on the depletion of charge carriers near the boundary.

It should be noted that the error in the calculation for values of s was quite large ($>2,250$ cm/s and $<40,500$ cm/s), because of the spread in the measured XRL intensities and the small differences in simulated intensity for different values of s . Calculated mean values were, however, found to be similar to surface and boundary recombination velocities reported in the literature [120-124]. Most importantly, the trends observed here are still accurate even with the large error, and because the value of s appears to be less significant than D , there was much less error in the calculated values of bulk XRL intensity presented in the following section.

In summary, the comparative analysis of Ce:YAG and Eu:Y₂O₃ ceramics, based on charge carrier diffusion parameters, showed that this approach can be a powerful tool for identifying more efficient inorganic ceramic scintillator materials. Results from the above XRLM studies suggest that lower charge carrier diffusion constants lead to a decrease in light yield attenuation, likely because charge carriers diffuse over a shorter path, and therefore have a higher probability of recombining at a site within the bulk of the grains. XRLM and cathodoluminescence techniques can aid in determining these properties, and thus helping determine if some materials are more sensitive to boundaries than others.

Additionally, the nature of defects at the grain boundaries and their overall effect on charge carrier trapping and non-radiative recombination have been shown to be quite important because of their contribution to the boundary recombination velocity (s). Evaluating these properties may be aided by XRLM analysis and bulk scintillation characterization techniques coupled with parametric processing studies. Atomistic and first-principles models of grain boundary electronic states also may inform the study of grain boundaries and scintillation performance. Atomistic modeling of grain boundaries in other classes of materials has been used with some success in predicting properties of compounds such as MgO and HfO₂ [125-128].

4.3. Eu:(Gd,Lu)₂O₃ Transparent Ceramic Sintering

Highlights:

- *Optically transparent ceramics of **Eu:(Gd,Lu)₂O₃** were prepared from pre-synthesized nanopowders through a step-wise application of temperature and pressure that was optimized for optical quality under similar conditions to those used in the Eu:Y₂O₃ mixed oxide ceramic fabrication procedure.*
- *Determined the phases existing over a range of **Lu₂O₃** and **Gd₂O₃** concentrations and defined the extent of the single-phase region over which the solid solution was cubic.*

Experimental Details:

To facilitate the fabrication of transparent Eu:Lu₂O₃ ceramics from nanopowders produced by spray pyrolysis (prepared at Lawrence Livermore National Laboratories), we initially relied on our previous work on hot pressing Eu:Y₂O₃ ceramics from mixed oxide powders. In that work, we found that a step-wise application of temperature and pressure led to more transparent samples and that transparent ceramics were produced over a large temperature range (1400 - 1800°C). However, the powder sizes in our previous study were large by comparison to these nanopowders (~1 μm), so the increased stress intensification

factors and the higher sinterability of the nanopowders should necessitate a different sintering program in order to optimize the final transparency of the ceramic. In this study, ceramics of $\text{Eu:Lu}_2\text{O}_3$ and $\text{Eu:}(\text{Lu,Gd})_2\text{O}_3$, were hot-pressed and the monoclinic-cubic two phase region in the binary oxide phase diagram studied.

Rare-earth sesquioxides exist in three stable crystalline structures at temperatures above $\sim 600^\circ\text{C}$, hexagonal (A), monoclinic (B) and cubic (C), based on the size of their cations [129]. Y_2O_3 has a cubic structure, while Gd_2O_3 and Eu_2O_3 have a monoclinic structure. In order to study the region over which the binary phase region exists in the $\text{Gd}_2\text{O}_3\text{-Lu}_2\text{O}_3\text{-10\%Eu}_2\text{O}_3$ phase diagram, differential thermal analysis (DTA) was carried out on powders with varied $(\text{Gd+Eu})/\text{Lu}$ cation ratios. Seven (7) samples with ratios between 0.3 and 47.5 and a sample with a ratio of 0.9 were analyzed.

DTA curves for 5 of the 8 samples are shown in Figure 45(a). Both heating and cooling ramps are plotted, at ramp rates of $10^\circ\text{C}/\text{min}$. Substantial supercooling was observed in all cases, suggesting that the monoclinic phase could be stabilized at temperatures well below the equilibrium phase boundary. The quasi-equilibrium phase boundaries are plotted in Figure 45(b) based on the DTA results. The boundaries converged at $\sim 2100^\circ\text{C}$ and a concentration of $\sim 47.5 \text{ mol\% Lu}_2\text{O}_3$. This concentration is lower than that of Y_2O_3 in the binary phase diagram of $\text{Y}_2\text{O}_3\text{-Gd}_2\text{O}_3$ (YGO), making the cubic phase in the Lu_2O_3 system more stable at higher temperatures [130]. However, the two-phase region is wider at lower temperatures than that of YGO.

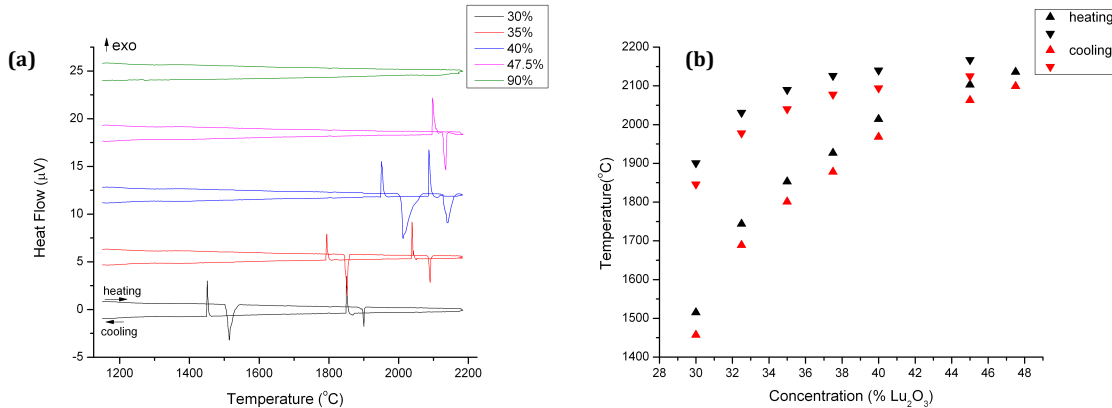


Figure 45: Differential thermal analysis (DTA) on $\text{Gd}_2\text{O}_3\text{-Lu}_2\text{O}_3\text{-10\%Eu}_2\text{O}_3$ powders with different ratios of Lu_2O_3 to Gd_2O_3 . DTA curves are shown in (a) and the resulting quasi-equilibrium phase diagrams upon both heating and cooling are shown in (b).

Two batches of $\text{Eu:}(\text{Gd,Lu})_2\text{O}_3$ powders were sintered by hot pressing to produce transparent ceramics and study the effect of processing parameters on optical transparency. Batch 1 had a chemical composition of $\text{Eu}_{0.1}\text{Gd}_{1.0}\text{Lu}_{0.9}\text{O}_3$, and Batch 2

had a composition of $\text{Eu}_{0.1}\text{Gd}_{0.9}\text{Lu}_{1.0}\text{O}_3$. A step-wise sintering program was used for both batches and ceramics were then HIPed and air annealed. Ceramics processed under different conditions are shown in Figure 46. Ceramics HIPed at 1750°C were found to be significantly more transparent than ceramics HIPed at 1800°C. This was found to be related to regions of low-density that were more present in ceramics HIPed at 1800°C (Figure 47). These open pore networks were not present in ceramics sintered from Batch 2 powder, and their formation may have been related to the segregation of Gd or Eu into a secondary phase at high temperature and pressure (see Figure 48 for chemical analysis).

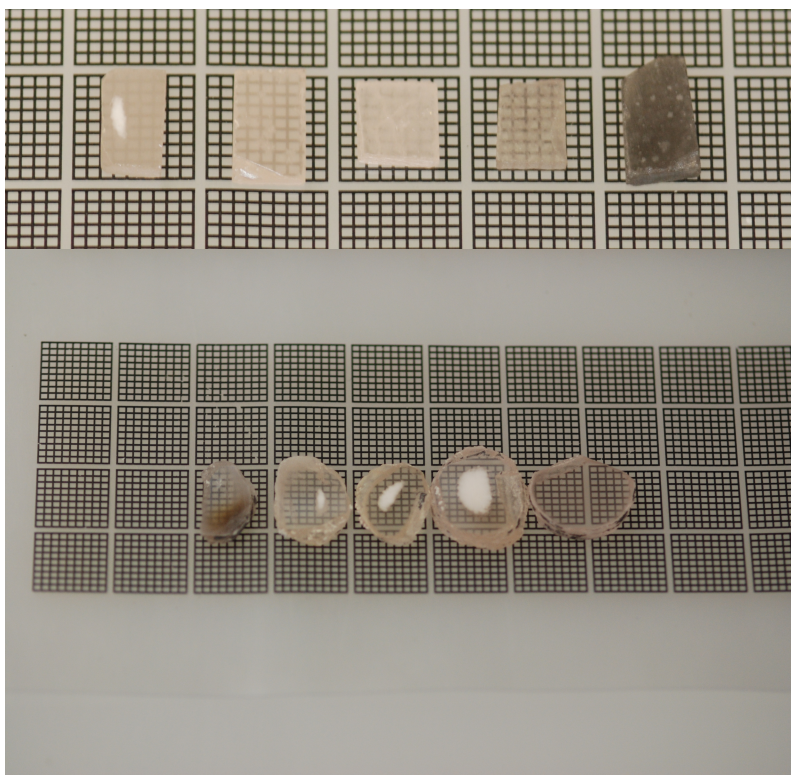


Figure 46: Ceramic $\text{Eu}:(\text{Gd,Lu})_2\text{O}_3$ processed under different conditions. Ceramics in the top image were HIPed at 1800°C and those in the bottom image at 1750°C. From left to right, samples were hot pressed at 1400°C, 1500°C, 1600°C, 1600°C/45MPa, 1650°C, 1600°C/45MPa, 1400°C, 1350°C, 1400°C, and 1600°C. The last two ceramics were sintered from Batch 2 powder. Ceramics were hot pressed at 40MPa, unless specified.

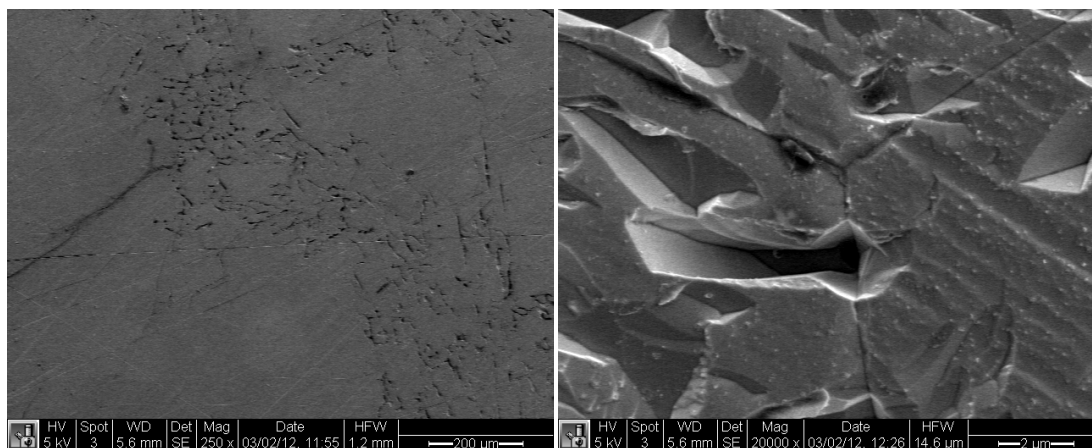


Figure 47: Low-density regions in a ceramic HIPed at 1800°C from Batch 1 powder.

Ceramics sintering at lower temperatures were also found to be more transparent than ceramics sintered at higher temperatures. This was related to the presence of larger pores incorporated into the ceramic grains after HIPing (compare SEM images in Figure 49(c)-(f)). After hot pressing, although pores remained at triple junctions in ceramics sintered at both low and high temperatures, the pores in the lower temperature samples were much larger than those sintered at higher temperature (compare SEM images in Figure 49(a) and (b)). The mobility of pores is inversely proportional to their size [131], and it appears that while HIPing the mobility of grain boundaries exceeded that of the larger pores, which causes the boundaries to move past them, inhibiting densification.

It was found that a similar step-wise sintering program was optimal for sintering $\text{Eu}:(\text{Gd},\text{Lu})_2\text{O}_3$ ceramics in addition to $\text{Eu}:\text{Y}_2\text{O}_3$ ceramics. In addition, secondary phases formation that can lead to degradation in density is important in this system. This limits the sintering conditions over which transparent ceramics can be produced.

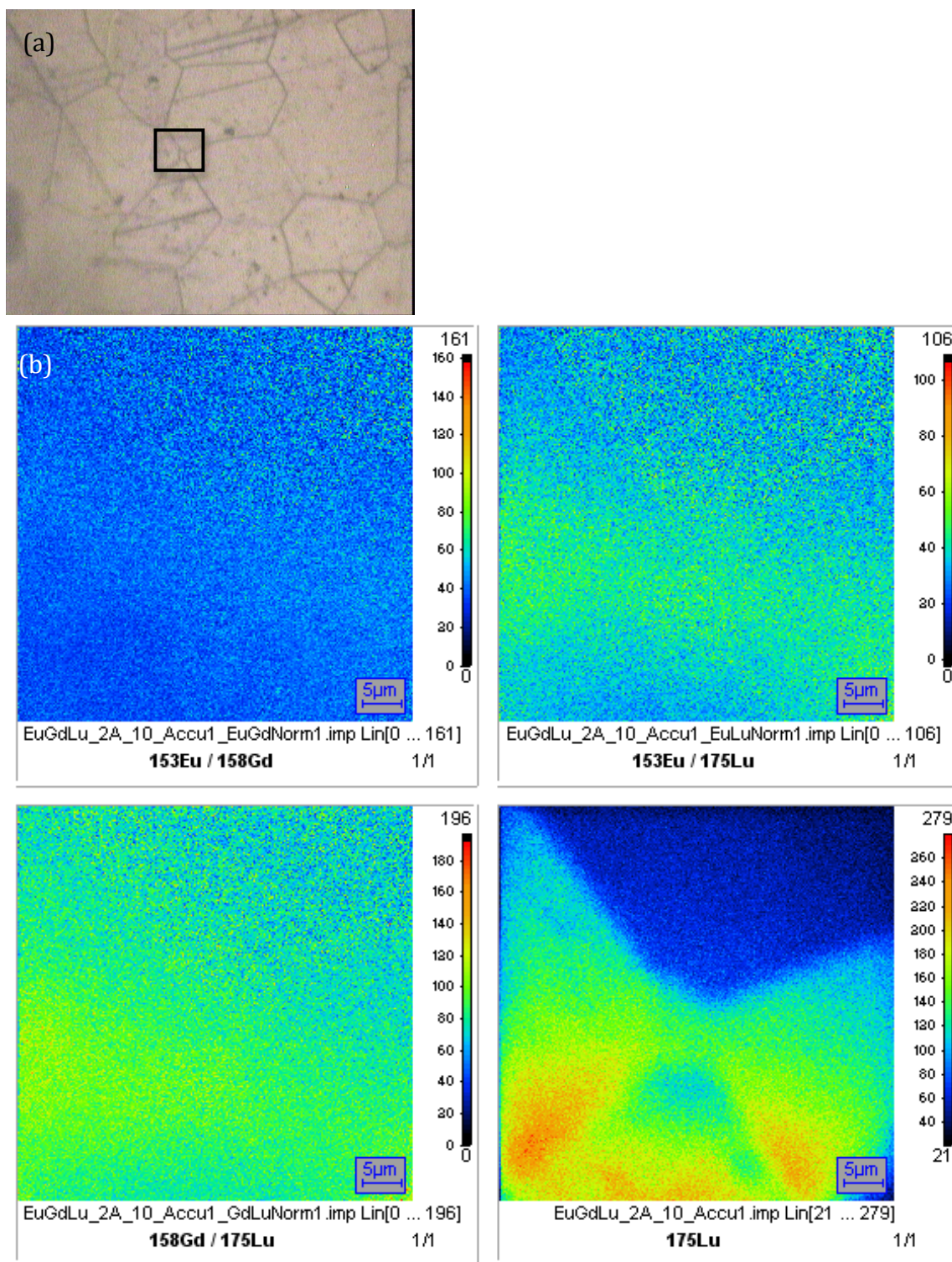


Figure 48: Nano-scale secondary ion mass spectrometry (NanoSIMS) analysis on ceramic (a) Optical image region analyzed by SIMS, showing grain boundaries from on chemical etched surface. SIMS maps were taken around a small inclusion that was a few microns in size. (b) Ratios of ion currents from Eu, Gd and Lu, showing a preferential segregation of Eu and Gd away from Lu in and around the inclusion. A Lu ion current map is shown, as well, in which the underlying microstructure can be seen due to preferential grain etching.

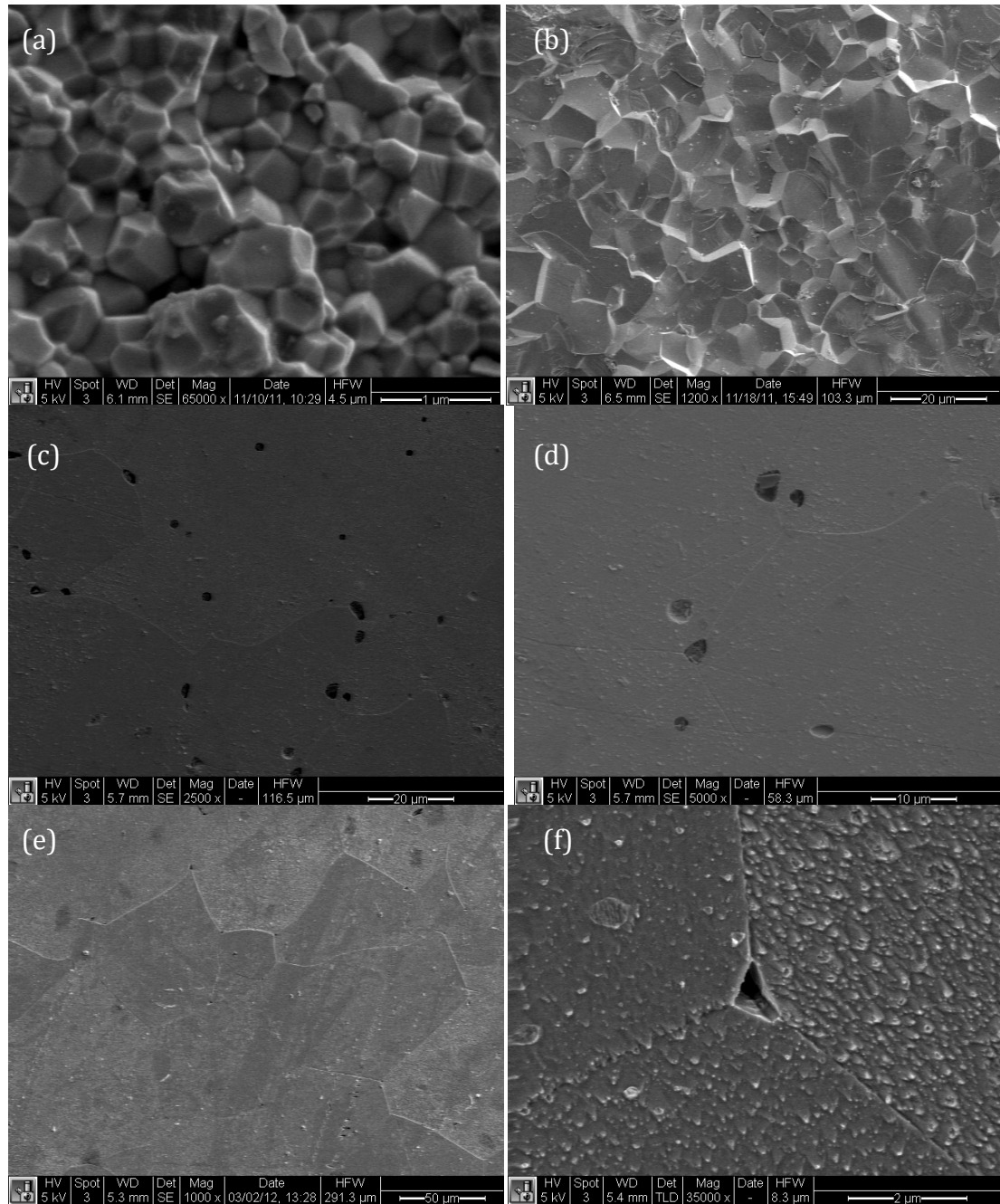


Figure 49: SEM images of ceramics sintered from Batch 2 at 1400°C in (a),(c) and (d) or 1600°C in (b), (e) and (f). (a) and (b) show ceramics pre-HIPing and (c), (d), (e) and (f) post-HIPing.

4.4. Ce-doped Alkaline Earth and Rare Earth Hafnates Ceramics: Sintering and Scintillation Properties

Highlights:

- Transparent ceramics of **Ce:SrHfO₃** and **Ce:BaHfO₃** were prepared by hot pressing pre-reacted nanopowders and **Ce:La₂Hf₂O₇** and **Ce:Lu₂Hf₂O₇** by hot pressing mixed oxide powders.
- Co-precipitated **Ce:La₂Hf₂O₇** powders were synthesized for the first time, and powder purity (e.g., chlorine contamination) and cation stoichiometry (i.e., Ce-to-La-to-Hf ratio) studied.
- While highly transparent ceramics were prepared, the poor scintillation properties found for the hafnate samples were attributed to intrinsic self-absorption and the oxidation of Ce³⁺ to Ce⁴⁺. Therefore work on these compounds was terminated.

Experimental Details:

Ce:BaHfO₃ and Ce:SrHfO₃ Ceramics

In a joint program with LLNL, the preparation of stoichiometric Ce:BaHfO₃ (BHO) and Ce:SrHfO₃ (SHO) nanopowders by the spray-pyrolysis method was investigated. The powders produced were not strongly agglomerated and the ultimate size of the particles was less than 10nm (Figure 50). This process enabled the production, for the first time, of fine-grained (~1 μ m) transparent ceramics of these materials (Figure 51).

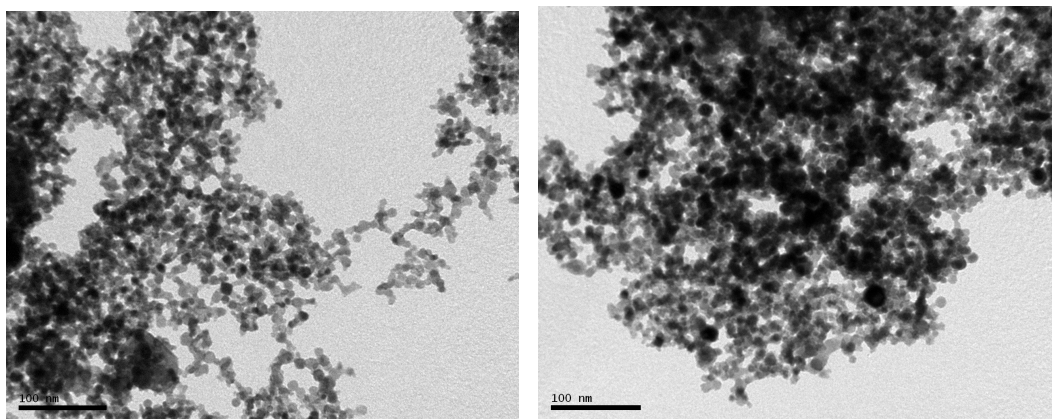


Figure 50: TEM pictures of 0.01 at.% Ce:BHO and Ce:SHO nanopowders made by spray pyrolysis.



Figure 51: 1mm-thick samples of 0.02 at% Ce:BaHfO₃ and Ce:SrHfO₃. The picture on the right shows the effect of heat-treatments on a Ce:SHO sample: parts of a hot-pressed sample (orange) has been successively air-annealed (yellow) and HIPed (light yellow).

The presence of Ce³⁺ ions in our samples was confirmed by the presence of a characteristic IR absorption corresponding to the transition between the $^2F_{7/2}$ and $^2F_{5/2}$ manifolds of the trivalent cerium (Figure 52). The position of the Stark levels of these manifolds can be assigned from this absorption spectrum (Figure 53). The zero-line is centered at 2142 cm⁻¹, which gives a spin-orbit coupling constant of 612 cm⁻¹, consistent with the value of 649 cm⁻¹ given in the literature. Compared to the spectrum obtained on annealed and HIPed samples, the spectrum of a hot-pressed only sample exhibited an additional strong and narrow absorption line at 3000 cm⁻¹. We believe that this line arises from the zero-line transition of Ce³⁺ ions occupying a different crystallographic site. This site would have a higher crystal-field as well as a higher symmetry (i.e. more forbidden 4f-4f transition therefore a narrower peak). The broadband absorption may correspond to a Ce³⁺ on the A site and the narrow band to a Ce³⁺ on the B site in the perovskite ABO₃ structure.

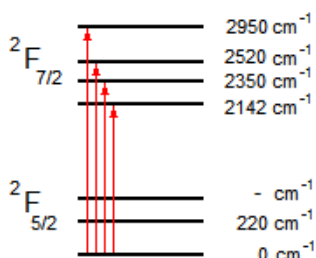


Figure 52: Energy diagram of the cerium $^2F_{5/2} \Rightarrow ^2F_{7/2}$ manifolds in Ce:SHO determined by absorption.

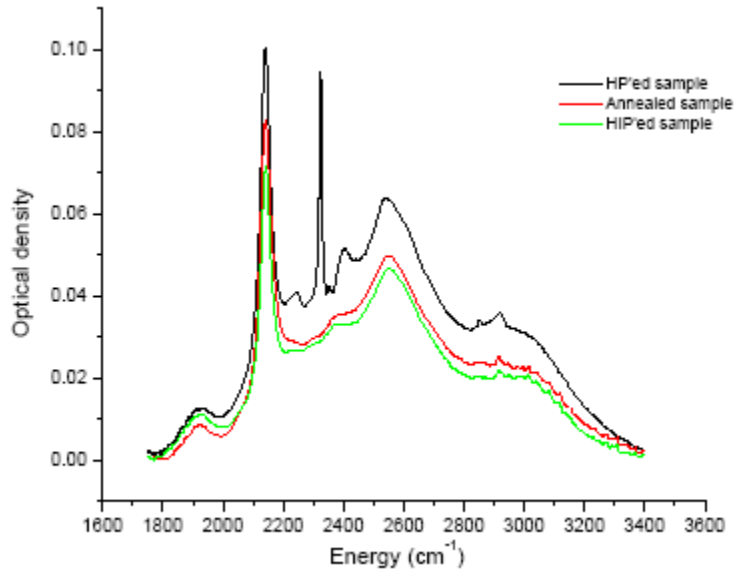


Figure 53: Infrared absorption spectrum for the transition ${}^2F_{5/2} \Rightarrow {}^2F_{7/2}$ in Ce^{3+} in hot-pressed, air-annealed and HIPed Ce:SrHfO_3 . After partial oxidation about 23% of the initial Ce^{3+} concentration is converted into Ce^{4+} .

After annealing in air, the overall intensity of the spectrum decreased by a factor of 1.3 (i.e. less Ce^{3+} , more Ce^{4+}) and the dopant then only occupied a single crystallographic site. The visible absorption spectra of Ce:SHO and Ce:BHO are presented in Figure 54. The reduced sample exhibits a broad absorption peak at 480nm. This band corresponds to color centers associated with oxygen vacancies.

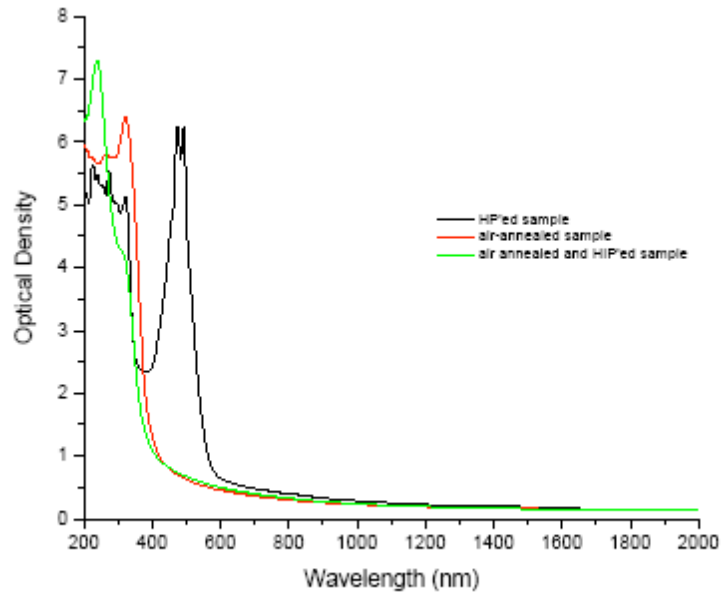


Figure 54: Optical density of hot-pressed, air-annealed and HIPed Ce:SrHfO_3 samples.

The absorption bands at 321 nm and below can be assigned to the localized 5d transitions of Ce^{3+} . The high-energy absorption edge reflects the host absorption behavior. Oxidized samples, enriched with Ce^{4+} , exhibited the onset of a strong absorption edge around 300 nm (3.5 eV). Similar behavior for cerium in Y_2O_3 was attributed to an acceptor-like electron transfer from the host valence band to the Ce^{4+} ion “ligand-to-metal” transfer. Photoexcitation of $\text{Ce}^{3+}:\text{SHO}$ by UV irradiation (280 nm) at room temperature did not show any detectable luminescence ascribable to Ce^{3+} . This suggests that the luminescence in this system is strongly quenched.

The scintillation performance of $\text{Ce}:\text{BaHfO}_3$ (BHO) and $\text{Ce}:\text{SrHfO}_3$ (SHO) ceramics was characterized under α and β excitations. The radioluminescence spectra are shown in Figure 55 and Figure 56.

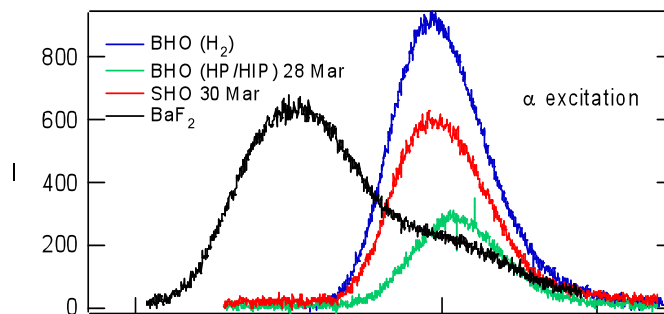


Figure 55: Radioluminescence spectra of the produced $\text{Ce}:\text{BHO}$ and $\text{Ce}:\text{SHO}$ ceramics under α excitation. The spectrum of BaF_2 is given for comparison.

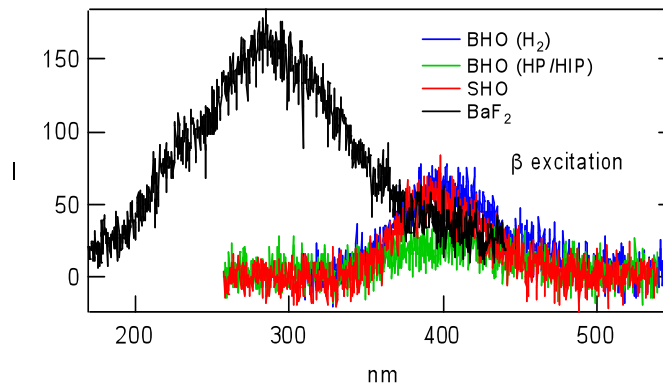


Figure 56: Radioluminescence spectra of the produced $\text{Ce}:\text{BHO}$ and $\text{Ce}:\text{SHO}$ ceramics under β excitation. The spectrum of BaF_2 is given for comparison.

As mentioned earlier, after spray pyrolysis it was found necessary to calcine the nanopowders in air to burn out carbon residues. However, a shortcoming of this calcination was the conversion of some Ce^{3+} to the tetravalent state. Significant

improvement was obtained by performing a second heat-treatment in hydrogen to restore the cerium ions to their trivalent state. This particular result is illustrated in Table 1 where ceramics made with H₂-treated Ce:BHO powders exhibit a higher light-yield than the ones made with untreated powders.

Table 7: Light yield of the produced Ce:BHO and Ce:SHO ceramics under α and β excitation. The light yield of BaF₂ is given for comparison.

	Light yield α (photon/MeV)	Light yield β (photon/MeV)
SHO ceramic	1240	1,700
BHO ceramic	540	1,200
BHO ceramic (powder heat treated in H ₂)	1,780	2,600
BaF ₂ single crystal	2,000	10,000

Three fundamental reasons that could explain the low light-yields in the hafnates ceramics are [132]:

- (i) an excess of strontium which forces Ce³⁺ into the B sites and introduces an absorption band overlapping with the Ce³⁺ emission,
- (ii) a deficiency in strontium which introduces small HfO₂ second phase particulates that scatter light,
- (iii) and small pores that scatter light efficiently in the blue where the cerium emits.

Therefore the fabrication of high light-yield Ce:BHO and Ce:SHO ceramics requires a precise control over strontium evaporation, cerium valence state and the ceramic porosity level. In the case of Ce:SHO for example, optical characterization shows that:

- (i) Absorption and radioluminescence spectra overlap (Figure 57)

and Rietveld analysis on X-ray diffraction patterns suggests that:

- (ii) hafnium is slightly deficient with a ratio Hf/Sr~0.99
- (iii) and, as a consequence, Ce³⁺ ions lie on the Hf⁴⁺ site.

Figure 54 showed that after successive high-temperature heat-treatments, the edge of the optical density spectrum was shifted to shorter wavelengths. This reduction in the extinction coefficient (i.e. cumulated effect of bulk absorption and scattering)

maybe related to (1) a progressive evaporation of the strontium excess towards stoichiometry, or (2) a reduction in scattering after the HIPing treatment. The former hypothesis seems the most probable, as pore density and size reduction do not normally lead to the formation of a shoulder in absorption spectra.

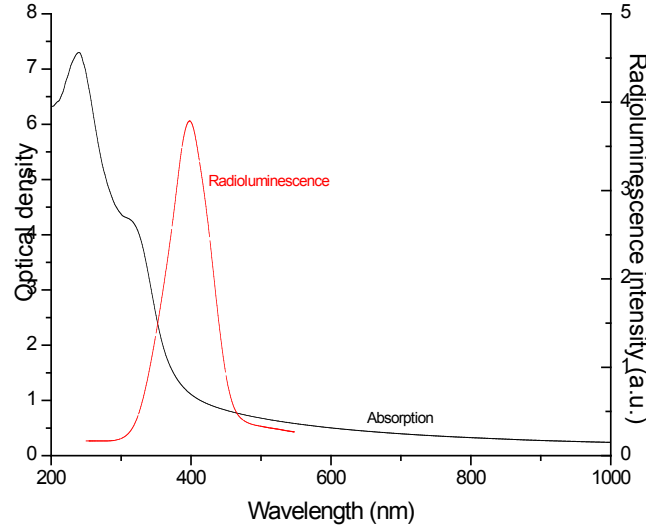


Figure 57: Overlap of the absorption and the radioluminescence spectra in the fabricated Ce:SHO ceramics. This overlap is believed to be the main reason for the poor light yield observed in our samples.

Ce:La₂Hf₂O₇ and Ce:Lu₂Hf₂O₇ Ceramics

During the second year of this program, transparent ceramics of Ce:La₂Hf₂O₇ (LHO) and Ce:Lu₂Hf₂O₇ (LuHO) were fabricated for the first time using a hot-pressing method, and the mechanisms contributing to densification and grain growth studied. LHO was sintered by both reactive and non-reactive methods, and the preparation of co-precipitated LHO nanopowders studied.

Nanosize powders of La₂Hf₂O₇ (LHO) were produced by a wet-chemistry process in which water-soluble La³⁺ and HfO²⁺ cations were co precipitated. The technique was inspired by a process developed by Komissarova *et al.* and Ushakov *et al.* who coprecipitated lanthanum and hafnium oxides [133,134] but for a different purpose and where the formation of LHO was not of primary concern.

One critical aspect of this process is that the precipitate formed must yield pure LHO by thermal decomposition. If any secondary phases are formed at this stage, they will likely produce light-scattering centers in the final ceramic. These phases form under the following circumstances:

- (i) if the concentration ratio of lanthanum and hafnium in the solid is not stoichiometric.
- (ii) if the participating ions are adsorbed by the solid during the precipitation process. Water-soluble salts of hafnium are scarce and only HfCl_4 is commonly available. Therefore, when using hafnium tetrachloride as a source material, one usually gets contamination from chloride ions, which form oxychloride impurities during calcination. Such impurities have clearly been identified by electron microprobe analysis as residing at the grain boundaries in the first set of hafnate ceramics prepared during these studies.

During our fabrication studies, we have addressed these two issues specifically.

The $\text{La}_2\text{O}_3\text{-HfO}_2$ phase diagram exhibits a wide $\text{La}_2\text{Hf}_2\text{O}_7$ -pyrochlore phase domain at high temperatures centered on the 1:3 molar composition [135]. The exact limits of this domain are not precisely known as they depend largely on the oxygen partial pressure and the kinetics of cooling during the measurements. However, previous studies suggest that, because of the extent of the pyrochlore solid-solution, fully dense ceramics will turn into transparent bodies if cooled relatively quickly from the sintering temperature ($\sim 1600^\circ\text{C}$). This would make the fabrication process not so sensitive to slight departures from the stoichiometric composition.

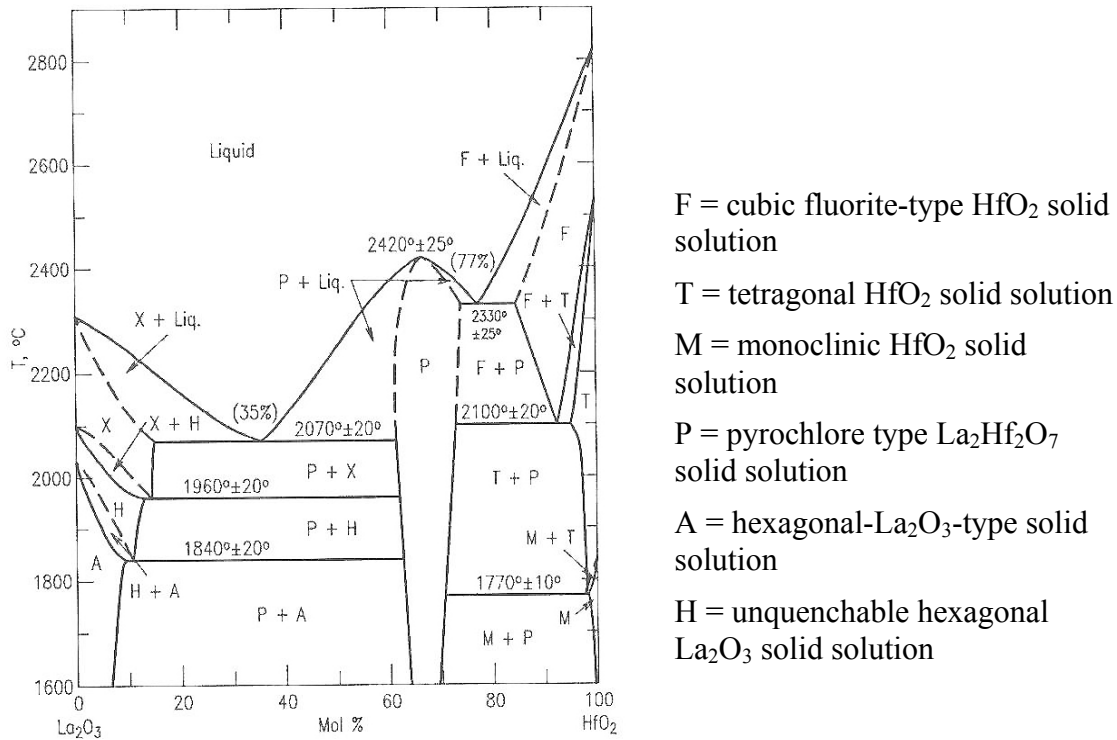


Figure 58: Phase diagram of $\text{HfO}_2\text{-La}_2\text{O}_3$ [135].

In preparing the starting material, it was found that particular attention must be paid to the accuracy of weighing the lanthanum oxide powder in order to guarantee that the preparation was stoichiometric. La_2O_3 is a very hygroscopic oxide and weight loss on ignition can be as high as 10% with most commercial powders. Figure 59 shows a thermo-gravimetric analysis (TGA) performed on this oxide. La_2O_3 loses a significant amount of water at 270°C, with the oxide reaching a constant mass at ~1120°C after the hydroxide and oxyhydroxides have slowly decomposed.

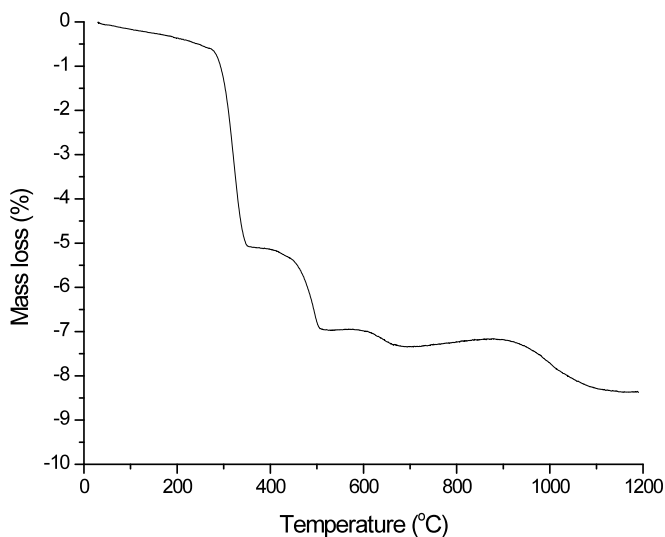


Figure 59: Thermo-gravimetric analysis (TGA) of a raw commercial La_2O_3 powder.

So far, all the fabrication studies done in this current work came to the same conclusion: the fabrication of LHO ceramics is sensitive to the starting composition. Small deviations of as much as 1 mol.% relative to the stoichiometric ratio $\text{La}:\text{Hf}=1:3$ were detrimental to the quality of the final ceramic. This might result from the narrowing of the LHO phase domain at low temperatures, coupled with a slow cooling rate or from the effect of the reducing environment used in our sintering experiments.

As stated earlier, the primary commercial source of hafnium used to prepare the LHO nanopowders was the tetrachloride HfCl_4 . To prevent the formation of oxychloride impurities in the final powder, an ion-exchange method was used. In this method the chloride ions are quantitatively eliminated and replaced by nitrate ions. It involved repeating a sequence of precipitations of hafnium hydroxide, followed by filtrations and thorough rinsing, and then dissolving this hydroxide in nitric acid. Three sequences are usually required before the chloride ions were completely eliminated in the rinsing filtrate. In a second step, hafnyl nitrate along

with lanthanum nitrate, both water-soluble salts, were mixed and added to an aqueous solution of ammonia in order to form a solid precursor of lanthanum hafnate (reverse-strike precipitation).

X-ray diffraction performed on calcined powders showed that, below 500°C, the precipitate was amorphous. At 900°C, LHO forms with the fluorite structure (F_{m3m}). Above 1200°C, LHO crystallizes with the pyrochlore structure (F_{d-3m}) (see **Figure 61**).

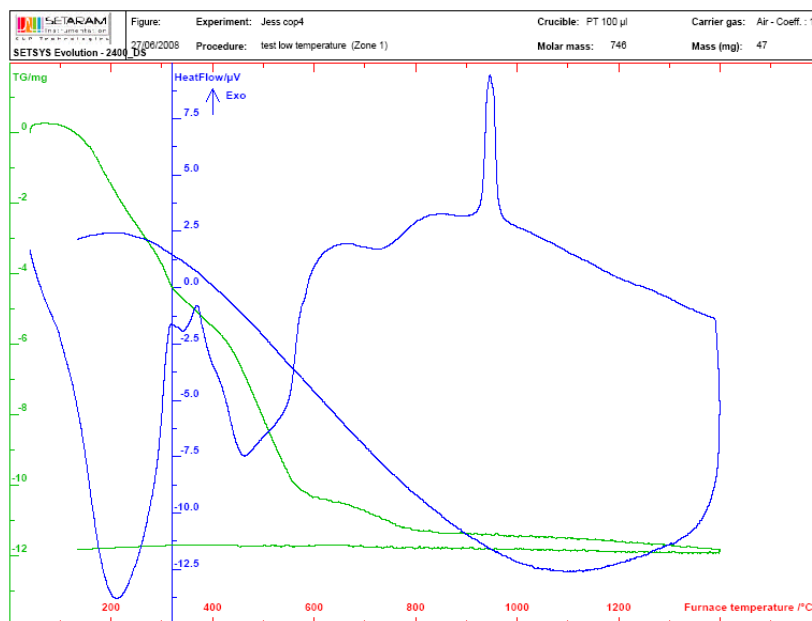


Figure 60: Thermo-gravimetric and differential analyses (TGA-DTA) of the LHO precursor. The TG signal is represented in green and the heat flow is in blue. The exothermic peak at 940°C corresponding to the fluorite-pyrochlore transition is clearly visible.

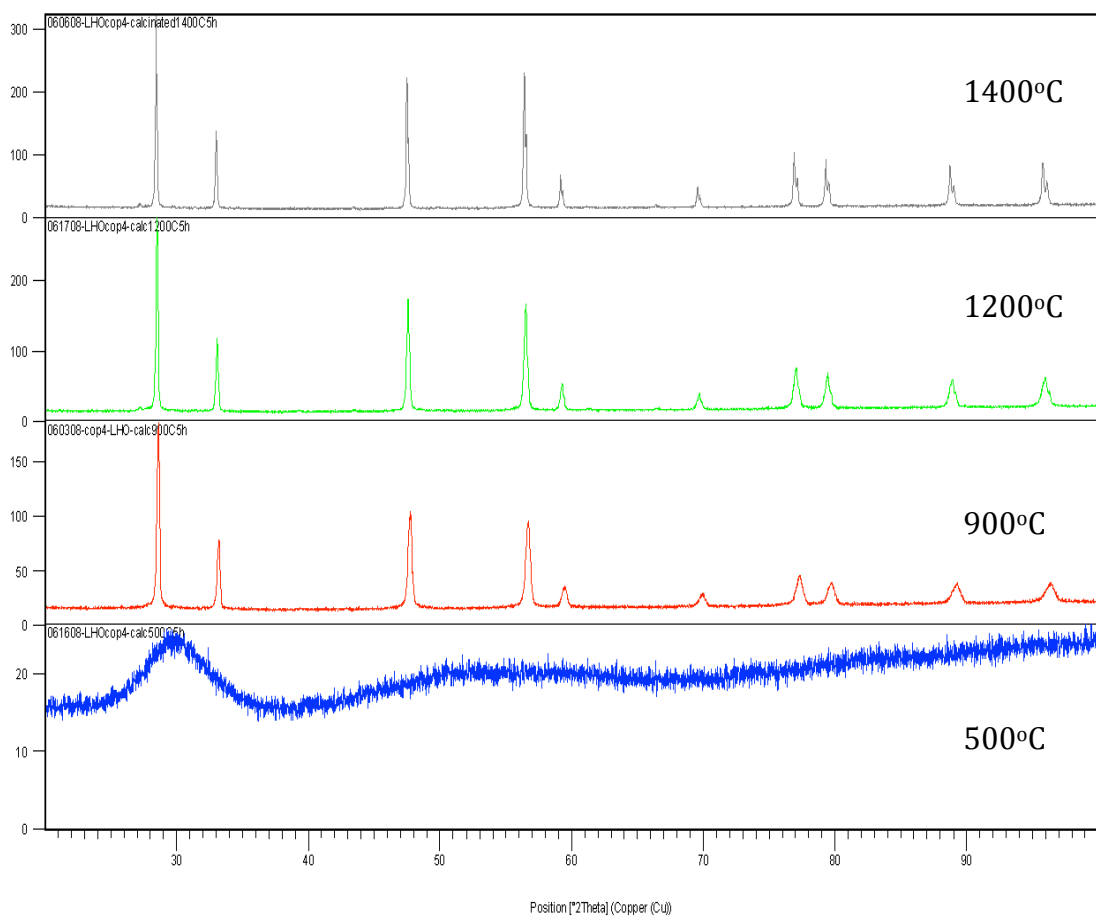


Figure 61: X-ray diffraction patterns of coprecipitated LHO powders calcined at various temperatures: 500°C, 900°C, 1200°C and 1400°C. This series of patterns illustrate

The average particle size of the LHO powders that were produced was 30 nm. The powders had an extreme fluffy appearance despite some degree of agglomeration as shown on the following SEM images (Figure 62).

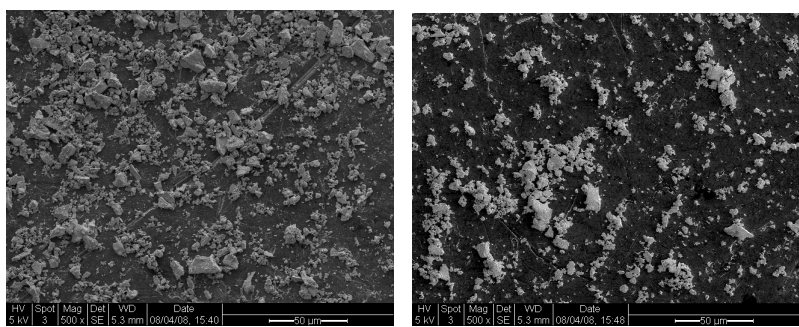


Figure 62: Coprecipitated LHO powder after calcination (a) at 900°C, (b) and 1200°C

The average crystallite size increased with calcination temperature and, for a constant soaking time, the effect of temperature is represented in Figure 63.

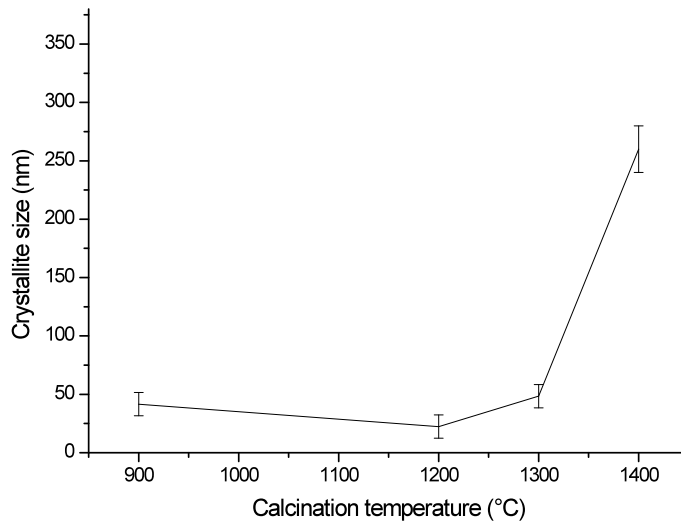


Figure 63: Average crystallite size of LHO particles as a function of calcination temperature. The soaking time is 2h.

The nanopowders produced were densified in the hot press. The influences of several processing parameters were investigated, including the time and temperature of the soak cycle as well as the duration of the out-gassing step. Regardless of these parameters densified LHO ceramics were obtained.

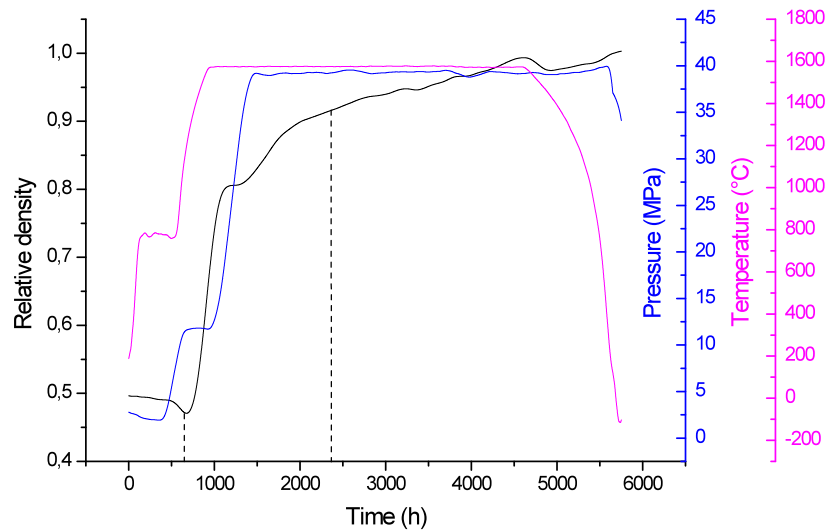


Figure 64: Densification of LHO nanopowders in a hot-press as a function of processing time. The hot-press temperature and pressure are also shown to

The curve in Figure 64 shows three different regimes during the densification:

- The first regime corresponds to particles rearrangement during which a sharp increase of the density is observed.
- The second regime corresponds to the densification with open porosity.
- The third and last regime corresponds to the collapse of the porous network and final densification by vacancy eliminations.

The fabrication of LHO ceramics was also investigated using hot-pressing with a mixture of lanthanum and hafnium oxides (reactive sintering). Preliminary results showed that the submicron-size powders of La_2O_3 and HfO_2 (see Figure 65) hardly react at temperatures below 1900°C without pressure. Despite this lack of reaction, confirmed by high-temperature thermal analyses on powder mixtures, fully reacted and densified LHO could be produced by hot-press at 1600°C under a pressure 40MPa.

The best procedure developed during this research program included blending fine powders of HfO_2 , La_2O_3 in a ball-mill using yttrium stabilized zirconia balls. When preparing optical ceramics by reactive sintering, fine starting powders are usually preferred as they provide a higher surface area for chemical reaction and lead to a better homogenization of the composition. In addition, if the grain size is kept small after sintering, mechanical properties are enhanced.

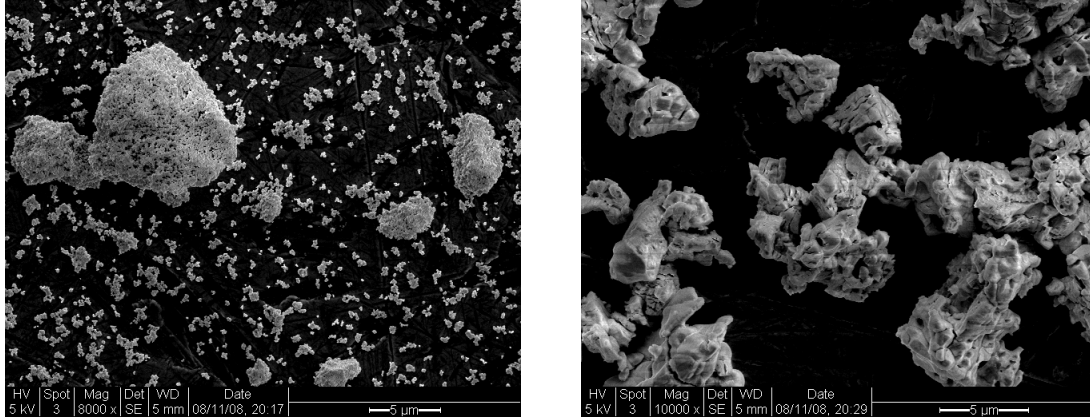


Figure 65: SEM pictures of HfO_2 (left) and La_2O_3 (right) powders.

As in the case of non-reactive hot pressing, LHO pellets were strongly reduced at high temperature in the graphite/inert atmosphere environment. Even though full density was achieved, samples were dark, showing transparency through very thin slices ($\sim 100\mu\text{m}$) (

Figure 66). By keeping the powder from coming into direct contact with the graphite die-case assembly, reduction of the ceramics could be avoided. Both boron nitride coatings and tantalum spacers were found to yield ceramics with much higher levels of translucency.

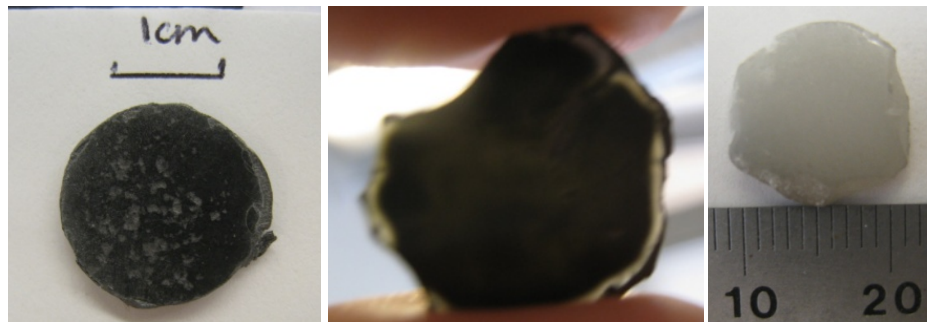


Figure 66: LHO pellets after hot-pressing in a graphite die with (a) only graphite foil spacers, (b) a boron nitride coating on the foil, and (c) tantalum foil discs.

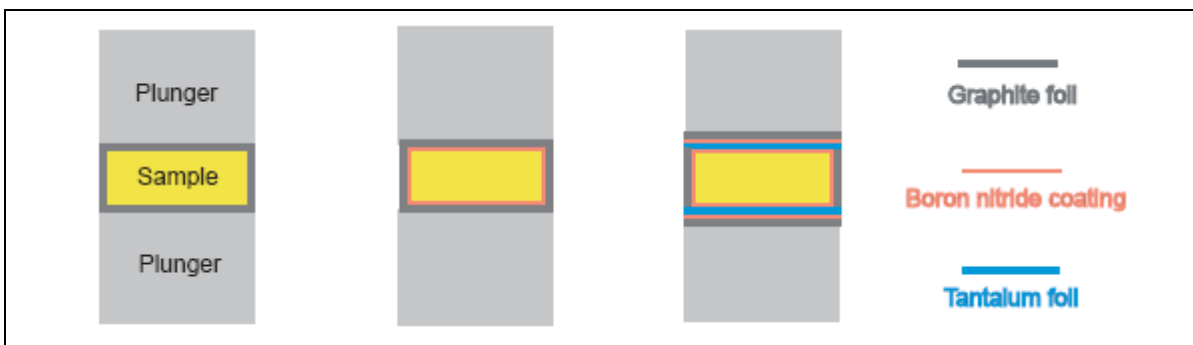


Figure 67: The three types of system that surrounded the pellet during hot-pressing.

Sintering two ceramic samples (0.1 at.% Ce:La₂Hf₂O₇ and 0.1 at.% Ce:Lu₂Hf₂O₇) through a step-wise sintering program produced the transparent samples shown in Figure 68.

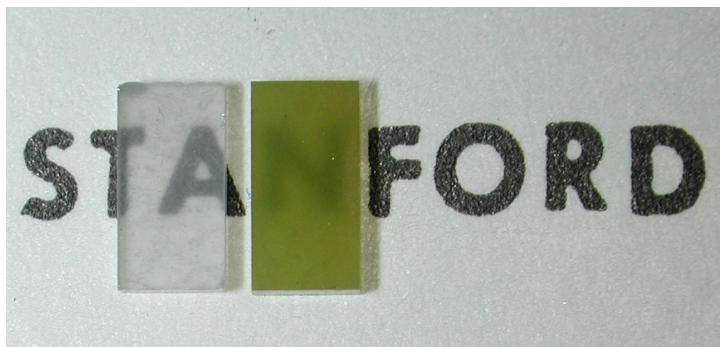


Figure 68: 1 mm thick ceramic samples of 0.1 at.% Ce:La₂Hf₂O₇ (left) and 0.1 at.% Ce:Lu₂Hf₂O₇ (right).

The fluorescence spectrum for Ce:Lu₂Hf₂O₇ showed greater splitting of the 4f electronic transition levels than those of Ce:La₂Hf₂O₇ (Figure 69). This may be due to the smaller unit cell volume of Lu₂Hf₂O₇. Both share the same pyrochlore crystal structure. The static field experienced by the larger Ce³⁺ ion from neighboring atoms in Lu₂Hf₂O₇ causes greater splitting of the its 4f levels than when Ce³⁺ occupies a La lattice site, which has a larger ionic radius than Ce³⁺. Absorption spectra of the samples show a broader absorption band in Ce:Lu₂Hf₂O₇ than Ce:La₂Hf₂O₇, which explains the low measured fluorescence intensity at shorter wavelengths in Ce:Lu₂Hf₂O₇.

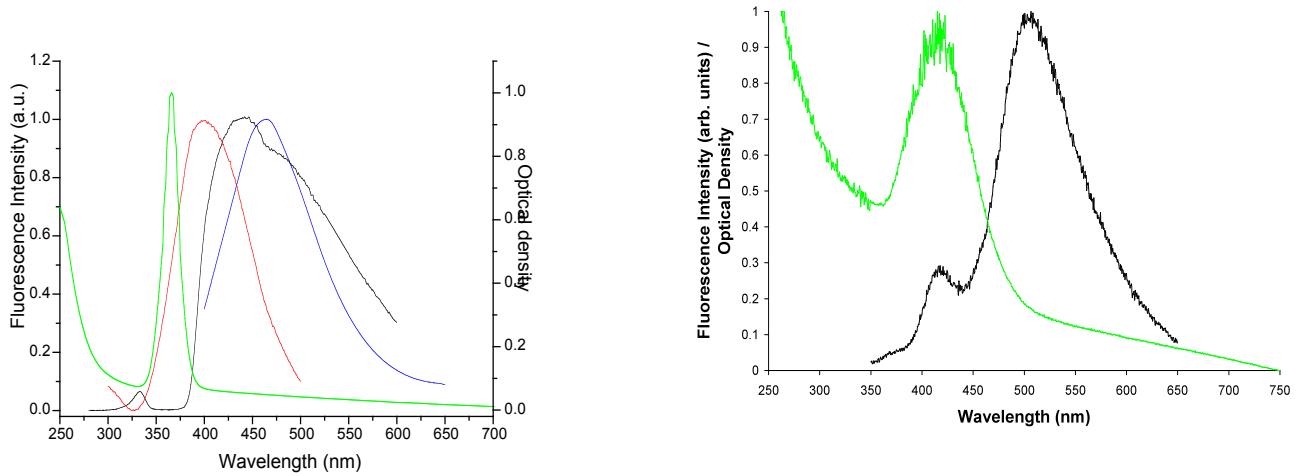


Figure 69: (a) Fluorescence under 268 nm excitation (red, black) and optical absorption of 0.1 at.% Ce:La₂Hf₂O₇. The spectrum in red was obtained from ceramic samples produced by reactive sintering. The spectrum in black was obtained from the same ceramics crushed to a powder. The spectrum in blue is the fluorescence spectrum obtained by A. Borosevich, et al. on a powder sample of Ce:La₂Hf₂O₇. (b) Fluorescence and optical absorption of 0.1 at.% Ce:Lu₂Hf₂O₇ ceramic sample.

Scintillation decay under 2 keV excitation on Ce:La₂Hf₂O₇ and Ce:Lu₂Hf₂O₇ samples was measured in collaboration with LBL. While the Ce:Lu₂Hf₂O₇ emission, (Figure 70(a)) was found to be strongly quenched, that of Ce:La₂Hf₂O₇ was found to have multiple decay components at 4 ns, 17 ns, 44 ns, and 141 ns (Figure 70(b)). Decay components were determined by linear fits to intervals of linearity in the log-plots of the decay curves. The decays at 17 and 44 ns are characteristic of other Ce³⁺ doped scintillators [136], while the longer component is likely due to de-trapping and the shorter component to quenching. Both samples were found to have low luminosity, with the luminosity of Ce:Lu₂Hf₂O₇ ~10% that of Ce:La₂Hf₂O₇. The low luminosity of these samples may be caused by the strong self-quenching observed in the optical spectra. This was confirmed by the scintillation decay behavior, which was significantly higher in Ce:Lu₂Hf₂O₇. While this is the first reported data on the scintillation behavior of Ce:La₂Hf₂O₇, the light yield of a Ce:Lu₂Hf₂O₇ transparent ceramic was previously reported to have a low (1,000 photons / MeV) light yield as well [137].

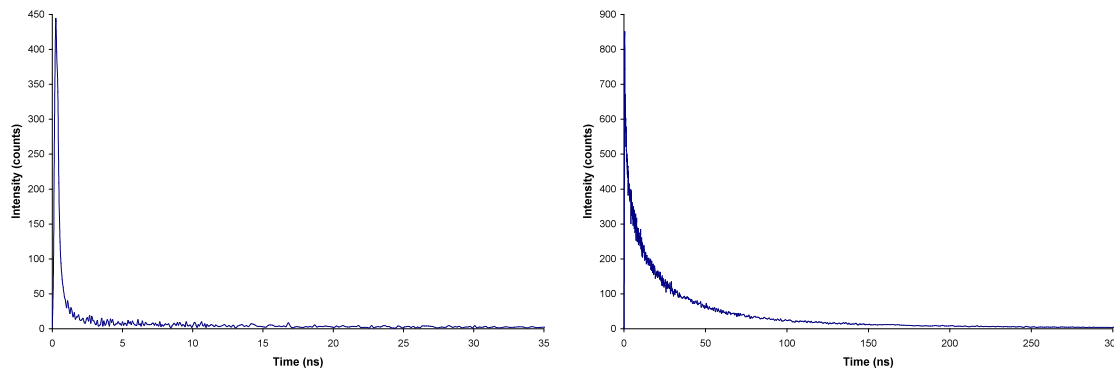


Figure 70: Scintillation decay of (a) 0.1 at.% Ce:Lu₂Hf₂O₇ and (b) 0.1 at.% Ce:La₂Hf₂O₇ from 2keV pulsed excitation.

4.5. Ce:Y₃Al₅O₁₂ (Ce:YAG) Ceramics: Sintering and Effect of Cation Non-Stoichiometry on Scintillation in Ce:YAG Transparent Ceramics

Highlights:

- *Transparent ceramics of **Ce:YAG** with varied cation ratios were prepared by vacuum sintering.*
- *Identified the relationship between cation stoichiometry, transparency and x-ray luminescence intensity. This study showed that stoichiometry must be preserved in order to optimize scintillator light yield.*

Experimental Details:

In order to extend the findings in Eu:Y₂O₃ to a more complex ternary oxide, Ce:YAG ceramics were fabricated and their optical and scintillation properties were characterized. In addition to non-stoichiometric oxygen content, which was shown to significantly affect the performance of Eu:Y₂O₃ ceramics, YAG ceramics may also have a limited, but significant, range of cation stoichiometries over which the garnet crystal structure is stable. It has been previously shown that cation non-stoichiometry in YAG is accommodated through the formation of yttrium antisite defects for yttrium-rich stoichiometries and aluminum antisite defects for aluminum-rich stoichiometries [138]. An antisite defect is the occupation of a cation of one species on the lattice site of a cation of a different species in a multi-cation material. Antisite defects in Ce:YAG have been shown to cause charge carrier trapping and degrade light yield [87], but no systematic study of the effect of cation stoichiometry on light yield has been reported in the literature. In this study and for the first time, the XRL spectra and lattice parameters of transparent Ce:YAG

ceramics with different Y-to-Al cation ratios were measured, compared and the relationship between their values and cation non-stoichiometry determined.

Ceramics of 0.1 at.% Ce:YAG with non-stoichiometric cation concentrations were sintered under high vacuum ($\sim 10^{-6}$ torr). Commercial powders of CeO_2 , Y_2O_3 , and Al_2O_3 were combined and de-agglomerated by ball milling with alumina balls and then spray dried to further extract large agglomerates from the powder mixture used to form the sintered bodies. Much attention was paid to maintaining the stoichiometric ratio between Y_2O_3 and Al_2O_3 because of the limited single-phase region of YAG. After ball milling, the powders were Al_2O_3 -rich, so incremental additions of Y_2O_3 powder were added. Powder samples with cation ratios between - 0.187% and 0.187%, as calculated from the relationship,

$$\left(\frac{\text{mol}(\text{Y}_2\text{O}_3)}{\text{mol}(\text{Y}_2\text{O}_3) + \text{mol}(\text{Al}_2\text{O}_3)} - \frac{\text{mol}(\text{Y}_2\text{O}_3^{\text{stoich}})}{\text{mol}(\text{Y}_2\text{O}_3^{\text{stoich}}) + \text{mol}(\text{Al}_2\text{O}_3^{\text{stoich}})} \right) \times 100\% \quad (37)$$

were prepared. The mixed powders were then cold uniaxially pressed to form pellets, and then cold isostatically pressed for further compaction. Optically transparent ceramics of Ce:YAG were produced by vacuum sintering at 1750°C for 12 hours. TEOS (0.5 wt.%) was used as a source of SiO_2 that serves as a sintering aid [139]. All samples were transparent with the exception of the most Al_2O_3 -rich sample (see ceramics in Figure 71).



Figure 71: 3.15-mm thick ceramics of 0.1 at.% Ce:YAG from Al_2O_3 - to Y_2O_3 -rich (left to right).

Characteristic Ce^{3+} absorption bands at 337 and 454 nm were present in the transmission spectra of all samples (Figure 72). The optical transmission of samples continually increased with the addition of 0.008 grams of Y_2O_3 in 0.002 gram increments. The optical transmission then continually decreased with additional Y_2O_3 . The stoichiometric condition was assigned to the most transparent sample, and the values of non-stoichiometry were calculated in comparison to this sample. Therefore, while values of non-stoichiometry are relative and based on optical transmission, not chemical data, they still allowed for a quantitative comparison of cation ratios between samples.

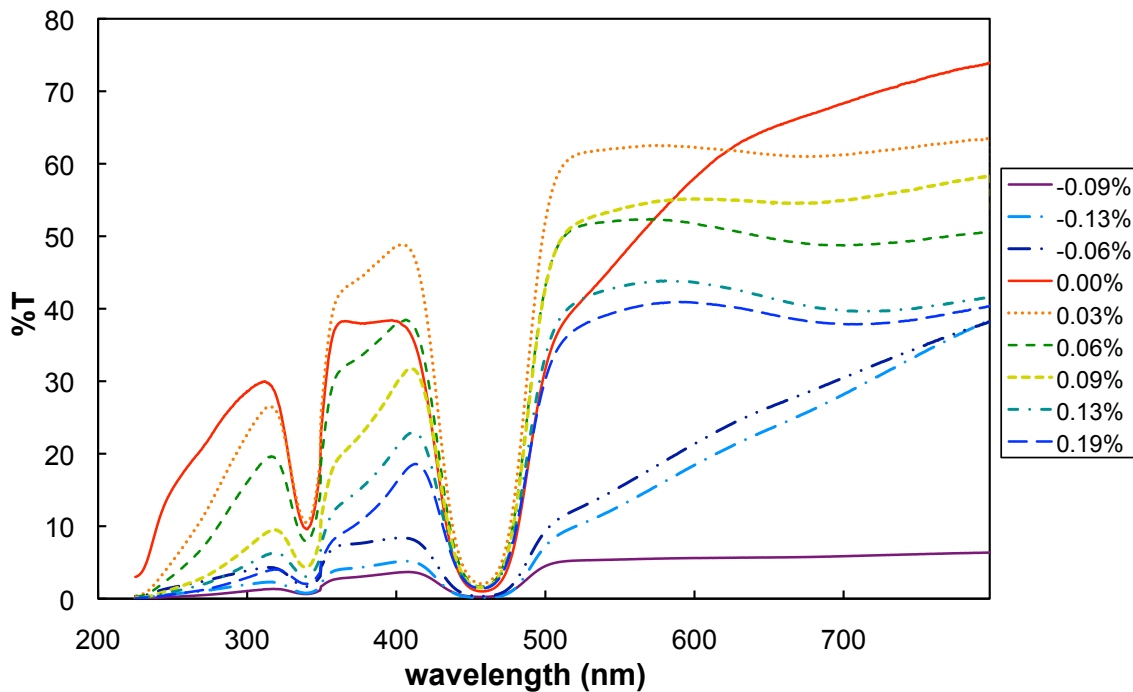


Figure 72: Optical transmission of Ce:YAG ceramics with different cation ratios.

Al_2O_3 -rich samples showed a broad absorption band from 500 - 600 nm that overlaps in part with the longer wavelength Ce^{3+} absorption. Y_2O_3 -rich and the sample identified as stoichiometric showed a broad absorption band at 600 - 800 nm. These absorption bands account for the red and green coloration of the Al_2O_3 -rich and Y_2O_3 -rich samples, respectively, and may be associated with oxygen defects in the YAG matrix [140]. Neither of these absorption bands was observed in non-stoichiometric undoped YAG ceramics processed under identical conditions [138]. This indicates that these defect bands are somehow associated with the Ce-doping.

Figure 73 shows the calculated lattice parameters for Ce:YAG ceramics with varied cation ratios. Lattice parameters were calculated from X-ray diffraction patterns using nonlinear least-squares fitting and regression diagnostics. A sinusoidal fit was used to subtract zero peak shift, using LaB₆ as a standard.

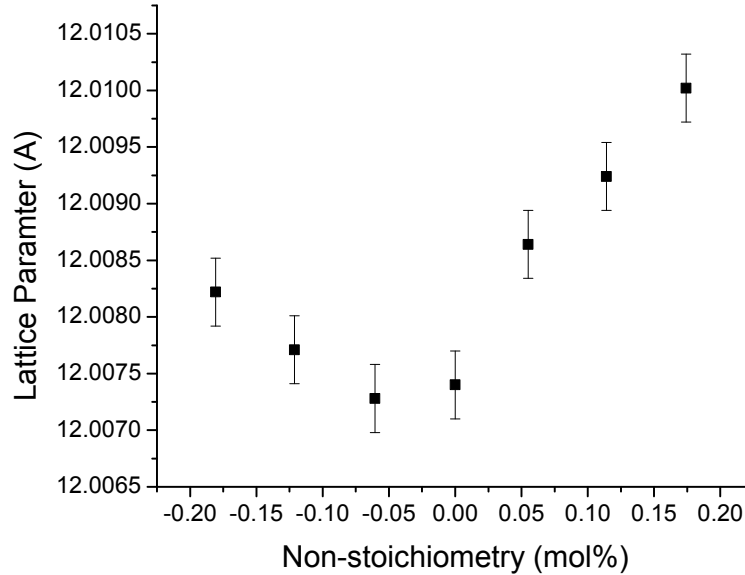
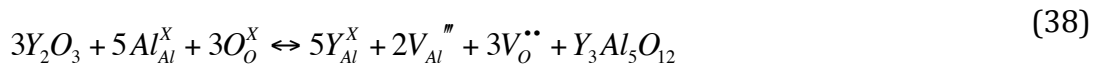


Figure 73: Lattice parameters of Ce:YAG ceramics with different cation ratios.

Lattice parameters were found to increase on either side of the stoichiometric concentration. This trend was also observed in undoped YAG ceramics [138], but here the lattice parameter increased more steeply with cation ratio with nearly double the slope. This slope corresponds to the defect reaction [138]:



This defect reaction is different from that in undoped YAG, where antisite defects form without additional vacancy formation. This may be due to the large atomic radius of Ce³⁺, which could lead to large lattice distortions that may be partially accommodated by these additional vacancies. The slope of lattice parameters of the aluminum-rich samples versus non-stoichiometry is the same for both Ce:YAG and undoped YAG samples, but the region for which the lattice parameter decreases is much narrower.

XRL spectroscopy under 40 keV excitation was used to characterize the Ce:YAG ceramics. The spectrum for the sample with -0.08 mol.% non-stoichiometry is shown in Figure 74(a). Both Ce³⁺ emission (peaking at 528 nm) and a UV emission (associated with the Y_{Al} antisite defects) are present [141,142]. Figure 74(b) and (c)

show the variation in XRL intensity of the Ce^{3+} and antisite defect emissions between samples. The antisite defect emission of the ceramic samples increased with increasing lattice parameter, verifying that the formation of antisite defects as the dominant mechanism for non-stoichiometric compensation. The ceramic with the lowest antisite defect emission intensity also had the highest Ce^{3+} emission intensity. These results indicate that the highest Ce^{3+} emission under X-ray irradiation is reached when the concentration of antisite defects is minimized. Therefore, in Ce:YAG, although there is a finite width to the single-phase region of the garnet structure, cation non-stoichiometry should be avoided in order to optimize scintillator light yield.

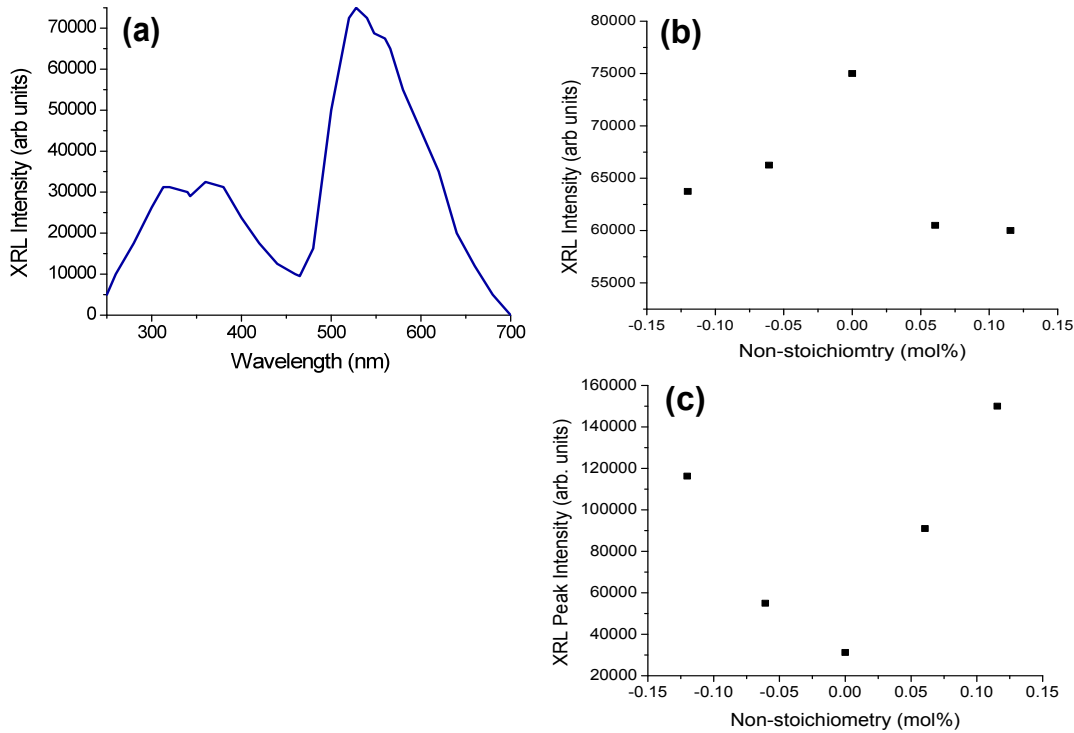


Figure 74: (a) XRL spectrum of most Al-rich Ce:YAG ceramic. XRL intensity of (b) Ce peak emission and (c) antisite defect emission of ceramics with varied cation ratios.

Based on these studies it is clear that knowing the exact stoichiometry of Ce:YAG and other garnet scintillators would also be important when comparing the scintillator properties of ceramics to single-crystals. Previous work investigating this comparison in Ce:YAG and Ce:LuAG did not discuss the cation stoichiometry of their samples [86,87,143,144]. While controlling the cation stoichiometry of YAG and LuAG crystals grown from a melt can be difficult because of non-constitutional cooling, the cation stoichiometry of ceramics can be controlled, as shown in these studies. However, the cation stoichiometry in ceramics is largely based on its value in the starting materials from which the ceramics were sintered, in the absence of

volatile species. Without careful control of the stoichiometry of starting materials—an often tedious process—and characterization of the cation stoichiometry of ceramics after sintering, the optimum performance of garnet ceramics will not be reached. This makes it difficult to accurately determine the role of grain boundary defect states on the properties of garnet scintillator ceramics.

4.6. SrI_2 and Eu:SrI_2 Ceramics: Effect of Grain Texturing on Optical Transmission in Translucent SrI_2 and Eu:SrI_2 Ceramics and Scintillation Properties

Highlights:

- *Developed the first highly translucent samples of SrI_2 and Eu:SrI_2 ceramics. Unlike the compounds described above, SrI_2 is a birefringent material, which typically exhibit grain boundary light scattering, thereby limiting transparency. The transparency of these SrI_2 ceramics was enhanced by pressure induced grain alignment.*
- *It was found that increased pressure led to increased grain texturing and higher optical transparency.*
- *Produce Eu:SrI_2 ceramics with a measured light yield of 25% of single-crystals and 55% of Tl:NaI .*

Experimental Details:

Ceramic Sintering

SrI_2 ceramics were produced from 99.99% nominally pure “anhydrous” powders from Alfa Aesar. This powder, however, is known to contain various hydrates and oxyiodides that can create second phase light scattering precipitates in crystals. SEM images of the powders used are shown in Figure 75. The Eu dopant was introduced by intermixing 5 wt.% “anhydrous” 99.9% EuI_2 from Sigma Aldrich with SrI_2 in an alumina mortar. Powders were stored and handled in a glove box with water vapor levels not exceeding 10 ppm. The low moisture containing nitrogen working gas originated from a liquid nitrogen supply. Powder compacts were formed by uniaxially pressing in a stainless steel die at 5.6 MPa. These compacts were then loaded into a high-density graphite die with graphite foil spacers to isolate the powder from the die walls. Undoped SrI_2 ceramics were sintered by uniaxial hot-pressing at 300°C, 350°C, and 400°C for either 30 minutes or 4 hours at 43 MPa.

Eu:SrI₂ ceramics were hot-pressed at either 350°C for 10 hours or 400°C for 4 hours. Samples sintered for 30 minutes were held at 100°C for 30 minutes to outgas the compacts before increasing the temperature to its maximum value and then applying pressure. Samples sintered for 4 hours were held at 200°C for 45 minutes while applying pressure, before ramping to the sintering temperature. Hot-pressing was carried out under vacuum with a nitrogen flow to maintain a baseline pressure of ~200 mtorr. A list of samples characterized in this study is given in Table 8. After pressing, the ceramics were stored in mineral oil to prevent samples from reacting with air.

Table 8: Processing Conditions of SrI₂ Ceramic Samples

Temperature (°C)	Time (hrs)	Doping
300	0.5	undoped
350	0.5	undoped
400	0.5	undoped
300	4	undoped
400	4	undoped
350	10	5 wt.% Eu
400	4	5 wt.% Eu

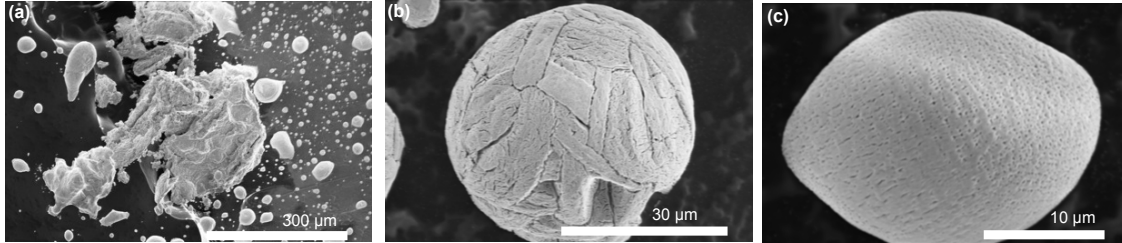


Figure 75: SEM Images of SrI₂ starting powders.

Sintering was carried out between 300 and 400°C, which was above the decomposition temperature of the hydrates of SrI₂ and EuI₂ found in the commercial powders, but substantially below the melting point and low enough to avoid exaggerated grain growth. In order to ensure that all the hydrates were decomposed at 300°C within 4 hours, thermogravimetric analysis (TGA) was carried out on powders following an identical temperature profile to the sintering program. All mass loss at 300°C was found to occur within 78 min.

The progression of relative density during hot-pressing as a function of time is given in Figure 76. The vast majority of densification occurred prior to reaching the soaking temperatures. Ceramics reached relative densities of ~0.98 by the end of the

temperature ramp, but only reached final density (~2% higher) after soaking at the maximum temperature. Figure 77 shows translucent samples of an undoped SrI_2 and a 5 wt.% Eu:SrI_2 ceramic produced by hot-pressing under the conditions used in this study.

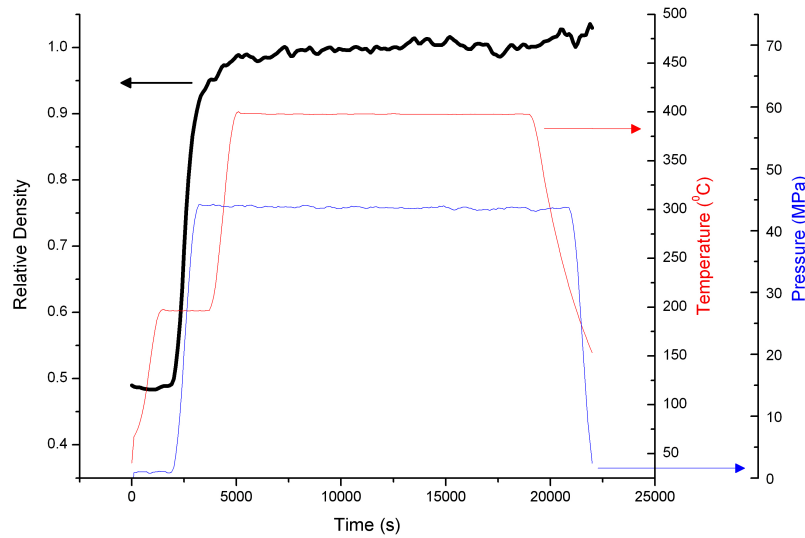


Figure 76: Hot-pressing schedule and evolution of the relative density of SrI_2 compacts.

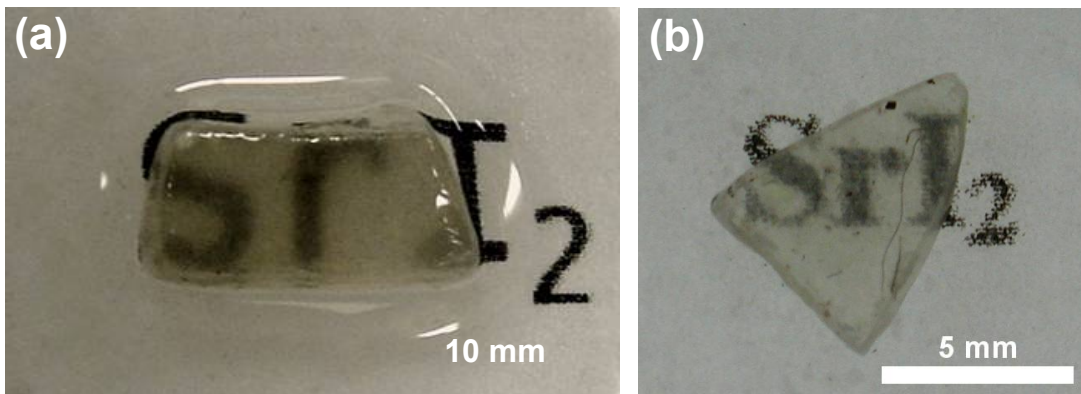


Figure 77: Translucent ceramics samples of (a) 1.75mm-thick SrI_2 front-lit and (b) 0.77mm-thick Eu:SrI_2 backlit. Samples are covered with a few drops of mineral oil to prevent exposure to air.

Microstructural Characterization and Grain Texturing

X-ray diffraction (XRD) measurements (with a Panalytical X'Pert Pro diffractometer and a Cu-K α source) were carried out on the SrI₂ starting powder and the ceramics pressed at 300°C and 400°C for 4 hours. Diffraction patterns were recorded under two experimental conditions: (1) in air with samples coated with a thick layer of petroleum jelly, and (2) in a nitrogen gas environment within a polyether ether ketone (PEEK) dome with samples coated with a thin layer of petroleum jelly. Before being mounted on glass slides, the ceramic samples were removed from the mineral oil in which they were being stored and rinsed in hexanes inside a glove box. The hexanes rinse was dehydrated by mixing it with a P₂O₅ desiccant for ~24 hours and then filtering it to remove the remnant P₂O₅ powder.

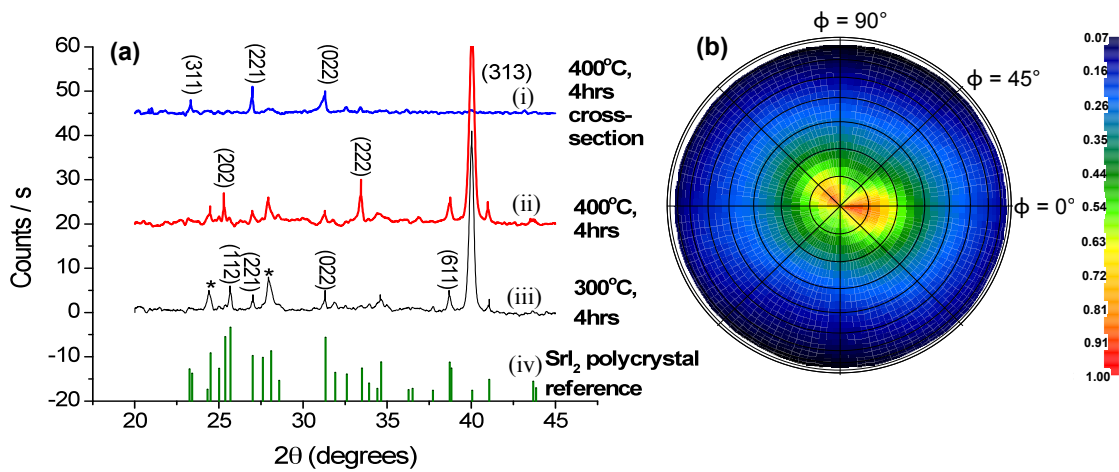


Figure 78: (a) X-ray diffraction patterns of SrI₂ ceramic sintered for 4 hrs at (i) 400°C and (ii) 300°C. (iii) Pattern of 400°C sample in cross-section and (iv) polycrystalline SrI₂ reference. Dominant SrI₂ peaks are labeled with indices. The (202), (112), and (022) planes diffract most intensely in an isotropically-oriented powder. SrI₂·H₂O peaks are identified by *. (b) Pole figure for (313) peak shown in (iii).

While the diffraction patterns of the SrI₂ starting powders contained all of the known low angle powder diffraction peaks for the SrI₂ P_{cab} crystal structure and its three hydrates, only SrI₂ and low intensity monohydrate peaks were observed in the SrI₂ ceramics, when analyzed in an enclosed dry nitrogen environment (Figure 78). The presence of the monohydrate peaks suggested the occurrence of a partial surface reaction. The intensities of the monohydrate peaks were found to decrease with surface grinding and increase with time (when the surface was coated with petroleum jelly and exposed to air). The diffraction patterns observed for the ceramic samples were not consistent with the ones expected for randomly oriented crystallites. Instead, when a SrI₂ sample pressed at 400°C was oriented so that the pressing direction was parallel to the normal of the diffractometer sample stage, the (313), (202), (222), and (611) planes of SrI₂ exhibited the strongest intensities.

However, the (311), (221), and (022) planes diffracted most strongly when a cross-section of the ceramic was analyzed (Figure 78). The dominant planes in the cross-section were at an angle of 73° to those of the planar sample. Variations in the relative intensity of the peaks of a single sample based on orientation may only arise from preferential alignment of crystallites along particular axes, indicating the presence of grain texture.

The (313) plane, a slip plane in the SrI_2 crystal structure, diffracted most heavily in both the 300 and 400°C samples sintered for 4 hrs. The 300°C sample was slightly more textured than the 400°C sample, with a Kearns' texture factor (f) of 0.67 and 0.53 for the (313) plane, respectively.

Scanning electron microscopy (SEM) was carried out on both powders and ceramics. Powders were loaded into a desiccator inside the glove box, where the powders were stored, during transport to the microscopy facility. Ceramics, which were stored in mineral oil, were washed with dehydrated hexanes, before coating with gold-palladium under vacuum and then immediately loaded into the SEM, with minimal air exposure. Optical microscopy in transmission mode was carried out at 250× magnification on 0.75mm-thick SrI_2 samples pressed at both 300°C and 400°C for 4 hours.

SEM micrographs of fracture surfaces in ceramic samples showed elongated grains in samples sintered at 300°C for 10 hrs and 350°C for 30 min (Figure 79), which may be related to the texturing observed with XRD analysis. Intra-granular cracking dominated in other samples, making it difficult to visualize the shape of individual grains. Grain sizes for samples were estimated from SEM and optical micrographs (Table 9).

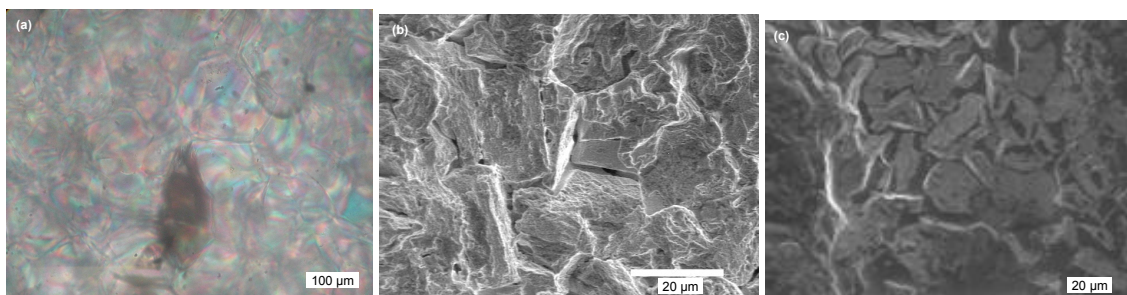


Figure 79: (a) Optical micrograph under cross-polarized light of 0.75 mm thick SrI_2 sample sintered at 400°C for 4 hrs. (b) SEM micrograph of SrI_2 sample sintered at 350°C for 30 min. (c) SEM micrograph of SrI_2 sample sintered at 400°C for 30 min. Darker regions in (a) show inclusions in sample that cause scattering. Darker regions in (c) show mineral oil pooled in the depressions of the fracture surface.

Table 9: Estimated Ceramic Grain Sizes

Temperature (°C)	Time (hrs)	Grain Size (μm)
350	0.5	25
400	0.5	70
300	4	80
400	4	120

Grain Texturing and Optical Transmission

Optical transmission measurements were made as a function of wavelength with a dual-beam Cary 500 spectrometer. Ceramic samples were ground to thicknesses of between 0.85 and 0.97 mm and polished on parallel faces with 1200 grit SiC paper. Samples were mounted inside a 1 mm deep cavity filled with mineral oil to prevent reaction with air. Transmission measurements on an oil-filled and empty cavity were used to determine their respective contributions to the total transmission.

SrI₂ ceramics sintered at 300°C for 30 min were found to be progressively more transmissive as the sintering pressure was increased, as shown in Figure 80. Pressure-induced deformation and texturing is common in alkali halides, and may account for the optical transmission of samples sintered under an applied pressure [145,146]. While texturing was found to be present in samples pressed at 43 MPa, no texturing was observed in samples sintered without pressure.

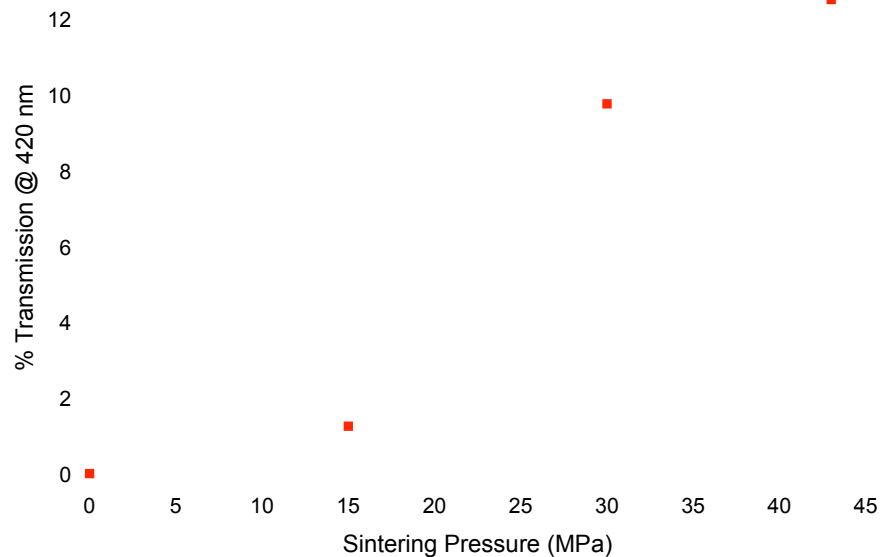


Figure 80: In-line optical transmission of 420 nm light in SrI₂ ceramics hot-pressed under different pressures.

SrI₂ ceramics sintered at 300°C for both 30 min and 4 hrs were found to be more transmissive than their counterparts sintered at 400°C. The samples sintered at 300°C are shown in Figure 81 to have had higher levels of grain alignment. Variations in optical transmission between ceramic samples may arise from either scattering or absorption of light. Because no obvious absorption bands exist in the spectral region probed here, as is apparent from Figure 81, variation in light scattering coefficients was the likely cause of these differences in transmission. In a birefringent ceramic, light may be scattered by residual porosity and secondary phases, as well as at grain boundaries of micron-sized grains, where a discontinuity in refractive index may exist. The fact that the shape of the transmission curves was consistent between ceramics sintered for the same time and had an inverse power law relationship with wavelength (Figure 82) indicates that scattering from porosity may be fairly consistent between samples. Therefore, scattering at grain boundaries may contribute most significantly to variations in the optical attenuation between samples.

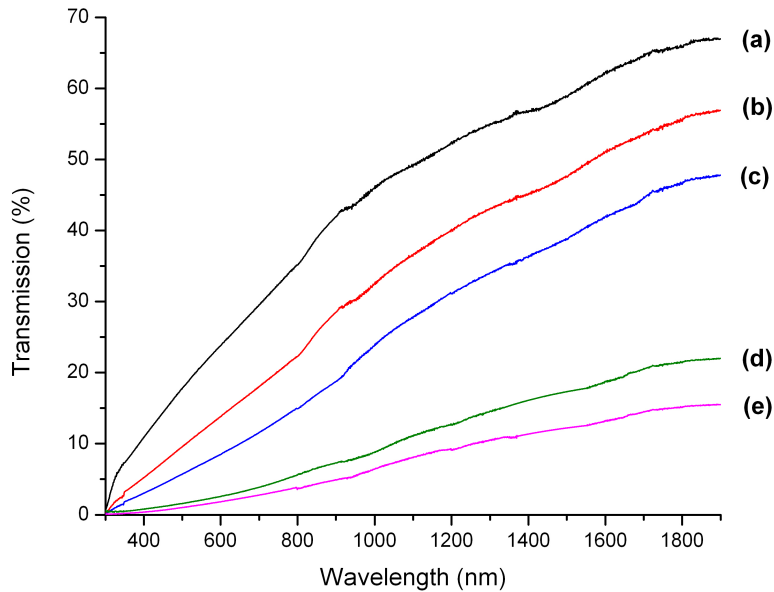


Figure 81: Optical transmission on 1mm-thick undoped SrI₂ ceramics sintered (a) for 30 min at 300°C, (b) for 30 min at 350°C, (c) for 30 min at 400°C, (d) for 4 hrs at 300°C, and (e) for 4 hrs at 400°C, showing improved transparency with decreasing temperature and time.

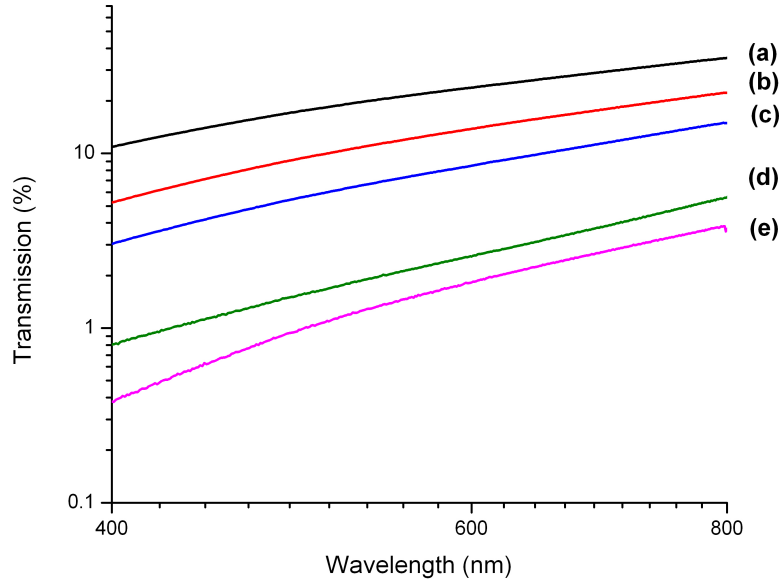


Figure 82: Log-log plot of optical transmission in the visible spectral range of Figure 81. The Fresnel limit of transmission for 420 nm light in SrI₂ is 75.6%.

In birefringent ceramics, two methods have been employed to improve optical transmission: (1) minimizing grain growth in order to maintain grain sizes at the nanometric scale and (2) inducing preferential texturing of grain orientations [147,148]. Although the grain sizes of samples sintered at 300°C were on average smaller than those of samples sintered at 400°C, all grain sizes were well into the tens of microns in size.

An idealized model developed by Raman, et al. [149,150] for diffraction-dominated light scattering in a birefringent polycrystalline body, given by

$$I = I_0 \exp(-v^2 \pi^2 \Delta n^2 K l d) \quad (39)$$

was used to evaluate the extent to which texture may play a role in the levels of optical transmission observed for ceramics in this study. Here, v is the wave-number and d is the grain size. The filling-factor, $0 \leq K \leq 1$, describes the probability of each of the primary axes being oriented in the direction of light propagation. A value of $K=0$ would characterize a fully-textured ceramic (or single-crystal), whereas a $K=1$ would describe a ceramic with a random grain orientation.

Values of K were calculated from levels of optical attenuation measured in SrI₂ ceramics. For randomly oriented ceramics with $\Delta n_{\max}=0.02$, $l=1\text{mm}$, and with grain sizes found in this study, the % T predicted by the model for even fully-dense ceramics would be ≈ 0 . For the % T measured in this study (Figure 82), K was

calculated to be between 0.009 and 0.014. Likewise, the grain sizes estimated for actual samples were clearly much larger than those predicted with this model for theoretical non-textured SrI_2 ceramics when using the levels of optical transmission measured in this study (on the order of $\sim 1 \mu\text{m}$). Therefore, the grain orientation of these ceramics appears to contribute greatly to the levels of optical transmission observed here and the variation in transmission between various processing conditions.

Scintillation Properties

Some of the scintillation properties of the SrI_2 and Eu:SrI_2 ceramics produced during this research project were measured and compared with single-crystals. As will be shown below, the ceramics did not have the excellent light yields of single crystals but there is potential for making significant improvements in their performance with more extended studies.

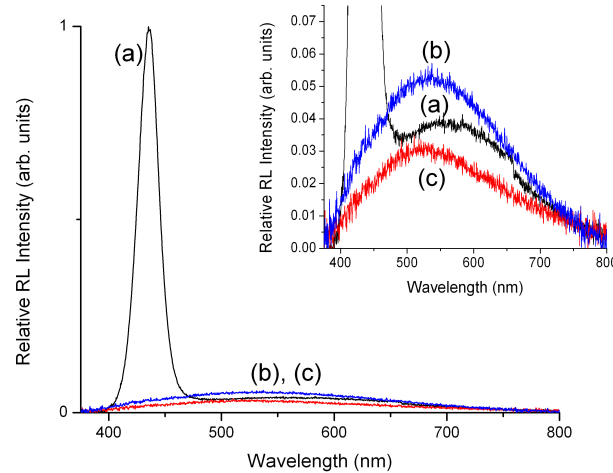


Figure 83: X-ray radioluminescence spectra of (a) 5 wt% Eu:SrI_2 and undoped SrI_2 ceramics sintered for 4 hrs (b) at 400°C and (c) 300°C under 50 keV excitation. (inset) X-ray radioluminescence of samples scaled $\times 29$. Spectra are normalized to the maximum intensity of the Eu^{2+} emission in (a).

X-ray radioluminescence (XRL) spectra under 50 keV excitation of 5 wt.% Eu:SrI_2 and undoped SrI_2 under different conditions are presented in Figure 83. The luminescence spectrum of Eu:SrI_2 shows the characteristic emission band of Eu^{2+} in a SrI_2 matrix, peaking at 435 nm [151,152]. A very broad emission over the entire visible spectrum was also present in all samples with a peak intensity $\sim 5\%$ of the Eu^{2+} emission. A similar broad-band emission, red shifted by $\sim 50 \text{ nm}$ with respect to the band observed here, was previously reported in Eu:BaI_2 single-crystals [152]. This emission was determined to originate from a defect-mediated recombination

process. A defect-induced emission at the same wavelengths as reported here was also observed in SrO [153].

Instrumental gas analysis was performed on the SrI₂ starting powders to determine their oxygen concentration. A value of 5100±255 ppm was measured during the analyses. The oxygen content was determined through the carbon monoxide level found in the gas stream, which was measured by non-dispersive infrared spectroscopy. Considering previous reports on alkaline earth iodides and oxides together with the broadness of the additional band, this emission is likely defect-mediated, and may be due to some form of oxidation or hydration of the iodide.

While the defect-mediated emission in Eu:BaI₂ showed a scintillation decay of 1.5 - 3 μs that was strongly dependent on the emission intensity [152], the longest components of scintillation decay in undoped SrI₂ were 433 ns and 445 ns for the 300°C and 400°C samples (under 2 keV excitation), respectively (Figure 84). This decay component is similar to the scintillation decay of 394 ns reported for SrI₂ powders in the literature [154]. The shorter decay components of the undoped sample sintered at 400°C contributed more heavily to the overall decay than for the sample sintered at 300°C. This indicates lower levels of charge carrier trapping in the sample sintered at 300°C.

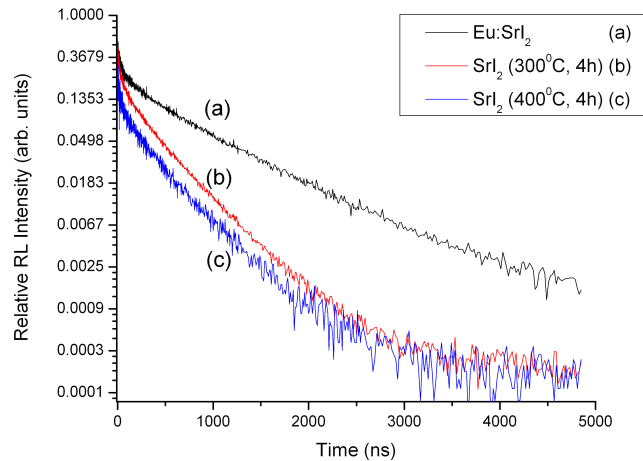


Figure 84: Scintillation decay of 5 wt.% Eu:SrI₂ and undoped SrI₂ from 2 keV pulsed excitation.

The combination of three exponential decay components with decay times of 93 ns, 197 ns, and 878 ns was a good fit to the decay behavior of Eu:SrI₂ ceramics. Eu:SrI₂ ceramics were also found to have very low afterglow with intensity falling to 0.5% of its maximum in 2.8 μs and to 0.25% of maximum within 4 μs. In 5 mol% Eu:SrI₂ single-crystals, the afterglow intensity fell to the same values at times of 2 ms and 20 ms, respectively [151]. The longest decay time in the Eu:SrI₂ ceramic was significantly shorter than the single component of 1.2 μs for 0.5 mol% Eu single crystals reported in the literature [151,152]. This decrease in scintillation decay

time may be due to an increased Eu concentration or other defects that cause quenching. The decay time of Eu^{2+} emission in BaI_2 was shown to decrease with increased defect-mediated emission [152], an emission that appears to be present in these ceramics and could be one factor in the shortened decay time observed here.

The scintillation light yield of the Eu:SrI_2 ceramic sintered at 350°C for 10 hrs was measured under γ -ray excitation using sealed isotopic sources. The measurement setup was a typical γ -ray spectroscopy arrangement, which included a photomultiplier tube (PMT), a preamplifier (Ortec 113), a pulse shaper (Ortec 572A), and a multichannel analyzer (Amptek, Inc., 8000A). The photomultiplier used was the 10-stage XP2060 from Photonis. The ceramic used in this test was a $5\times6\times0.77\text{ mm}^3$ polished slab, directly coupled to the entrance window of the PMT and kept immersed in a few drops of mineral oil to protect it from moisture and oxygen. A block of PTFE (Teflon) was used as a top reflector, and Teflon tape was wrapped around this assembly to increase light collection of diffuse reflections. The measurements were compared to a $10\times10\times3\text{ mm}^3$ BGO single-crystal purchased from SilvaCo, Inc. Full-absorption peaks were corrected for background noise with a computer program.

In the experimental setup utilized for these studies, the average PMT quantum efficiency was 29.5% at 420 nm, the emission wavelength of $\text{Eu}^{2+}:\text{SrI}_2$. This resulted in an average light yield of about 21,000 ph/MeV for the ceramic, assuming a light collection efficiency of 70%. The light yield results fall short of the reported light yield of $\sim 100,000$ ph/MeV for single-crystals [151]. This may in part be due to the non-optimized transparency and purity of the ceramic and the fact that the surface polish and size of our samples do not compare with that of the BGO standard. Pulse height spectroscopy on a thicker (1.75mm) segment of the same ceramic sample yielded no photopeak, suggesting that light yield is significantly degraded due to poor light propagation in the sample. Therefore, improvements in optical transmission should improve ceramic scintillator performance. Scattered light will trace out a longer distance and will therefore be attenuated to a greater extent in the presence of absorbers. Absorption may be caused by either impurities or the re-absorption and quenching at Eu^{2+} . In a completely textured and fully-dense ceramic, it should be possible to obtain nearly single-crystal-like optical transmission. However, even with a 50% decrease in the filling-factor, i.e., increased grain alignment, the optical attenuation coefficient should decrease by 50%. This level of optical attenuation will also allow for thicker samples that absorb radiation more efficiently, while still producing observable photopeaks. As these ceramics have been shown to be easily textured during pressure sintering, it may be possible to reach higher levels of grain orientation by pressing under higher pressures, while maintaining the moderate temperatures used in this study.

Pulse height spectra were obtained by exposing the ceramic to radiation from ^{241}Am , ^{109}Cd , ^{133}Ba , ^{57}Co , ^{22}Na and ^{137}Cs sources for one hour. At energies higher than 300 keV, less defined photopeaks were produced by the 0.77mm-thick sample due to insufficient stopping power. Figure 85 shows the spectrum obtained with an

^{241}Am source. The limited thickness of the sample caused the large escape-peak intensities.

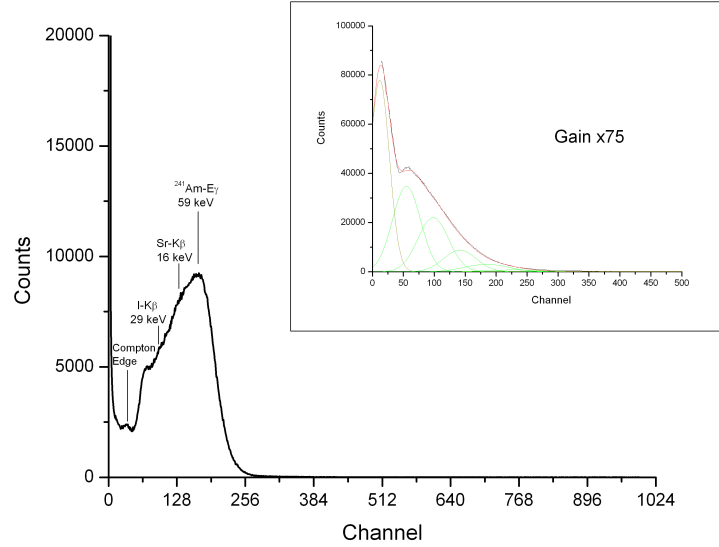


Figure 85: Pulse height spectrum obtained for a 0.77mm-thick $\text{Eu}^{2+}:\text{SrI}_2$ translucent ceramic exposed to the radiation of ^{241}Am . The full-absorption Gaussian peak at 59 keV was accompanied by K-escape peaks from K shell transitions in both strontium and iodine (electron binding energies of 16 and 29 keV respectively). The insert shows the single photoelectron spectrum used to calibrate the PMT used in this experiment. In this spectrum, the first peak on the left arose from electronic noise (ADC pedestal), and the broad peak to its right resulted from the overlap of single-, 2-, 3-, 4- and 5-photons peaks.

The uncertainties in light collection efficiency for the ceramic prevent a good estimate of the absolute light yields. However, because the ratio $\eta_{\text{BGO}}/\eta_{\text{SrI}_2}$ is constant in this series of experiments, the relative light yields obtained at various γ -ray energies with respect to that obtained at 661.7 keV can be compared, and the evolution of the ceramic response with γ -ray energy (Figure 86) can be determined. The number of photons per unit energy created by γ -rays in the scintillator typically depends on the γ -ray energy and is lower—in most cases—in the energy region below 100 keV and reaches a maximum at 100-200 keV. $\text{Eu}:\text{SrI}_2$, however, exhibits a very proportional response, and the result here on a ceramic sample confirms a characteristic already observed in single-crystals using the Compton-Coincidence Technique [155].

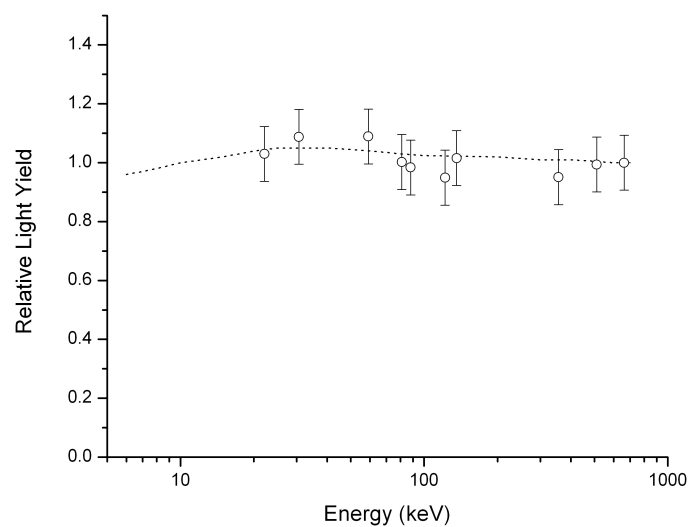


Figure 86: γ -ray energy response of a 0.77mm-thick $\text{Eu}^{2+}:\text{SrI}_2$ translucent ceramic. Dotted line is the response of the single-crystal from [155].

5. Deliverables

5.1. DTRA annual reports

Five annual reports for the fiscal years ending in 2007, 2008, 2009, 2010, and 2011.

5.2. Refereed journal publications

Stephen R. Podowitz, Romain Gaume, and Robert S. Feigelson, "Effect of Europium Concentration on Densification of Transparent Eu:Y₂O₃ Scintillator Ceramics using Hot Pressing." *J. Am Ceram. Soc.*, **93** 82-88 (2010).

Stephen R. Podowitz, Romain M. Gaume, Wesley T. Hong, Atlal Laouar, and Robert S. Feigelson. "Fabrication and Properties of Translucent SrI₂ and Eu:SrI₂ Scintillator Ceramics." *IEEE Trans. Nucl. Sci.*, **57** 3827 (2010).

Romain M. Gaume and Lydia M. Joubert. "Airtight Container for the Transfer of Atmosphere Sensitive Materials into Vacuum Operated Characterization Instruments." *Rev. Sci. Instrum.*, **82**[12] 123705 (2011).

Stephen R. Podowitz. Romain M. Gaume, and Robert S. Feigelson. "Probing Grain Boundaries in Ceramic Scintillators using X-Ray Radioluminescence Microscopy." *J. Appl. Phys.*, **111**[1] 013520 (2012).

Stephen R. Podowitz, Stephen M. Hanrahan, Edith Bourret-Courchesne, Nancy C. Giles, Romain M. Gaume, Robert S. Feigelson. "Effect of Grain Boundaries and Oxygen Stoichiometry on Light Yield and Charge Carrier Trapping in Eu:Y₂O₃ Transparent Ceramics" to be submitted shortly to *J. Appl. Phys.*

5.3. Inventions

Patent Disclosure: R. Gaume, *Airtight container for the transfer of atmosphere sensitive materials to characterization instruments*. Stanford University Ref No. 10-327.

5.4. Theses

Stephen R. Podowitz. *The Effect of Grain Boundaries on Scintillation in Rare-Earth Doped Transparent Ceramics*. Ph.D. Dissertation, Stanford University, Stanford, CA (2011).

Full text available at <http://purl.stanford.edu/mc738ct2500>.

5.5. Presentations

R. M. Gaume, Invited talk. "Ceramic Materials: A Promise for High-Power Lasers and Nuclear Detectors." *Frontiers in Optics* (Optical Society of America), San Jose (Jan. 2007).

S. R. Podowitz, R. M. Gaume, and R. S. Feigelson. "Effects of Processing Parameters on Transparency and Grain Structure of Eu: Y₂O₃ Scintillator Ceramics." *MRS Fall Meeting*, Boston (Nov. 2007).

S. R. Podowitz, R. M. Gaume, and R. S. Feigelson. "Effect of Europium Concentration on Densification of Transparent Eu:Y₂O₃ Scintillator Ceramics." *4th International Symposium on Transparent Ceramics for Photonic Applications*, Shanghai (Nov. 2008).

J. Rabeau, S. R. Podowitz, R. Gaume, and R. S. Feigelson. "Fabrication of Transparent Ce:La₂Hf₂O₇ by Hot-Pressing for Scintillation Applications." *4th International Symposium on Transparent Ceramics for Photonic Applications*, Shanghai (Nov 2008).

R. Gaume, Invited talk. "Control of Defects in Laser and Scintillator Ceramics" *Advances in Optical Materials* (Optical Society of America), San Jose (Oct. 2009).

S. R. Podowitz, S. Hanrahan, E. Bourret-Courchesne, N. Cherepy, R. M. Gaume, and R. S. Feigelson. "Effect of Grain Size and Processing on Light Yield of Eu:Y₂O₃ Transparent Ceramics" *SORMA*, Ann Arbor (May 2010).

S. R. Podowitz, W. T. Hong, A. Laouar, R. M. Gaume, and R. S. Feigelson. "Fabrication and Scintillation Properties of Translucent Eu:SrI₂ Ceramics" *SORMA*, Ann Arbor (May 2010).

R. S. Feigelson, Invited talk. "Single Crystals versus Transparent Ceramics for Use in Scintillation Devices." *International Conference on the Science and Technology for Advanced Ceramics (STAC)*, Yokohama, Japan (Jun. 2010).

S. R. Podowitz, N. Haegel, R. M. Gaume, and R. S. Feigelson. "Micro-scale Scintillation Characterization Across Grain Boundaries in Eu:Y₂O₃ Transparent Ceramics." *Stanford Photonics Research Center Annual Symposium*, Stanford, CA (Sep. 2010).

S. R. Podowitz, R. M. Gaume, and R. S. Feigelson. "X-ray Radioluminescence Microscopy for Scintillation Characterization across Boundaries in Transparent Ceramics" *MRS Spring Meeting*, San Francisco (Apr. 2011).

R. M. Gaume and S. R. Podowitz, Invited talk. "Effect of Grain Boundaries on Scintillation in Rare-Earth Doped Transparent Ceramics." *7th International*

Symposium on Transparent Ceramics for Photonic Applications, Singapore (Nov. 2011).

6. Personnel Supported

Dr. Robert S. Feigelson, PI
Dr. Stephen R. Podowitz, Ph.D. Graduate Student
Dr. Romain Gaume, Research Associate
Ye He, Ph.D. Graduate Student
Atlal Laour, M.S. Visiting Graduate Student
Jessica Rabeau, M.S. Visiting Graduate Student
Wesley Hong, Undergraduate Student
Clarissa Gutierrez, Undergraduate Student
Alice Che, Undergraduate Student
Ludwig Galambos, Engineering Technician

7. Interactions/Transitions

Consultative and Advisory functions to other laboratories, etc.

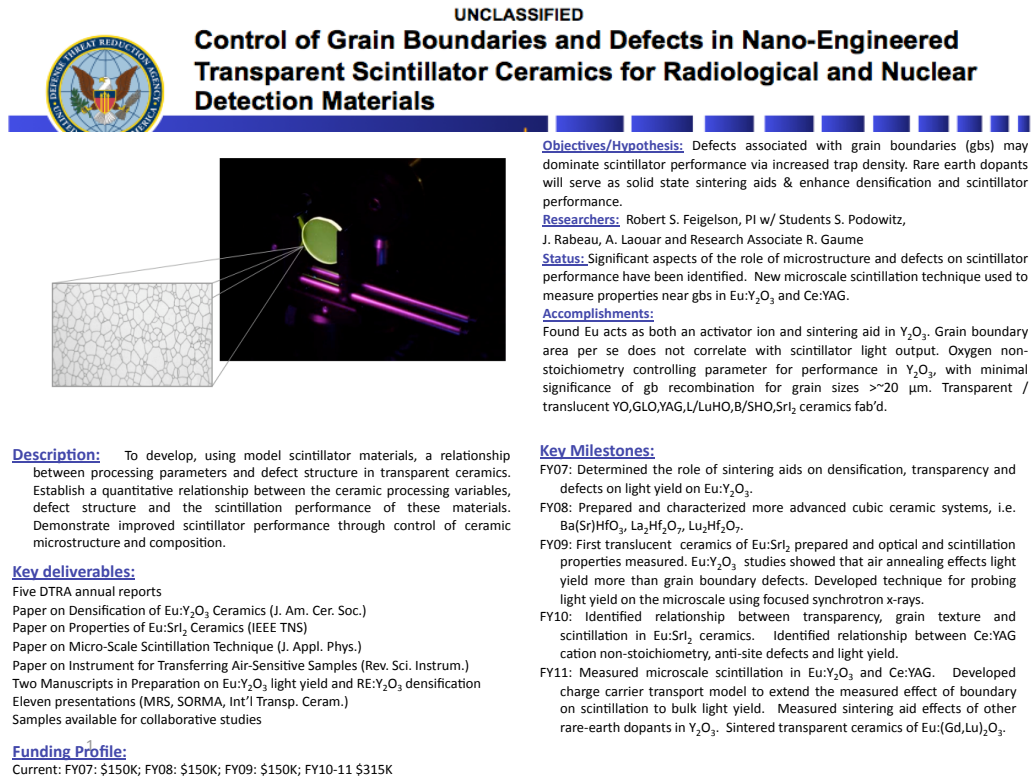
The team visited on separate occasions the Lawrence Livermore and Lawrence Berkeley National Laboratory, where technical discussions were carried out, research results reviewed and collaborative studies explored. We met with Drs. Nerine Cherepy and Steve Payne at Livermore on January 24, 2007. At the Berkeley National Laboratories we met with Drs. Edith Bourret-Courchesne and Stephen Derenzo on January 18, 2007 where we reviewed the facilities and set-up procedures for getting our ceramic samples measured. Since then we have been preparing and evaluating ceramic compositions of promising new scintillator materials being studied at LLNL and also are doing extensive characterization of our samples at the UC Berkeley Laboratories. We also collaborated with Prof. Nancy Haegel at the Naval Postgraduate School on the cathodoluminescence transport imaging characterization of micro-scale scintillation in Eu:Y₂O₃ ceramics and developed XRLM techniques at the Stanford Synchrotron Radiation Lightsource in conjunction with Sam Webb for the same purpose. Confocal fluorescence and Raman techniques to look at crystallinity were carried out in the laboratory of Prof. Mark Brongersma with Ed Bernard at Stanford's Materials Science Department. Thermoluminescence studies on some of our ceramic samples were carried out at the University of Tennessee-Knoxville in Prof. Chuck Melcher's laboratory with the assistance of Paul Cutler, and electron paramagnetic resonance studies were carried out at West Virginia University in the lab of Nancy Giles, who is now at the Air Force Institute of Technology.

8. Honors/Awards

On May 1, 2008, R. Gaume was nominated for the Stanford Mentoring Award. The Stanford Mentoring Award Program aims to raise awareness of the importance of quality mentoring and recognize faculty/senior scientists who are excellent mentors.

Dr. Stephen Podowitz won the student poster award at the 2008 annual DTRA Grantee's Review Conference in Washington DC.

9. Quad Chart



10. References

1. C. W. Wilson, E. V. van Loef, J. Glodo, N. Cherepy, G. Hull, S. Payne, W.-S. Choong, W. Moses, and K. S. Shah. "Strontium iodide scintillators for high energy resolution gamma ray spectroscopy." *Proc. of SPIE*, **7079** 7079171–7079177 (2008).
2. N. J. Cherepy, B. W. Sturm, O. B. Drury, T. A. Hurst, S. A. Sheets, L. E. Ahl, C. K. Saw, M. A. Pearson, S. A. Payne, A. Burger, L. A. Boatner, J. O. Ramey, E. V. van Loef, J. Glodo, R. Hawrami, W. M. Higgins, K. S. Shah, and W. W. Moses. "SrI₂ scintillator for gamma ray spectroscopy." *Proc. of SPIE*, **7449** 74490F (2009).
3. K. P. McKenna and A. L. Shluger. "Electron-trapping polycrystalline materials with negative electron affinity." *Nature Mater.*, **7** 859–867 (2008).
4. K. McKenna and A. Shluger. "The interaction of oxygen vacancies with grain boundaries in monoclinic HfO₂." *Appl. Phys. Lett.*, **95** 222111 (2009).
5. A. L. Shluger, K. P. McKenna, P. V. Sushko, D. Muñoz Ramo, and A. V. Kimmel. "Modelling of electron and hole trapping in oxides." *Modeling Simul. Mater. Sci. Eng.*, **17** 084004 (2009).
6. S. Siebentritt, M. Igalson, C. Persson, and S. Lany. "The electronic structure of chalcopyrites—bands, point defects and grain boundaries." *Prog. Photovolt: Res. Appl.*, **18** 390–410 (2010).
7. E. D. Bourret-Courchesne, G. Bizarri, R. Borade, Z. Yan, S. M. Hanrahan, G. Gundiah, A. Chaudhry, A. Canning, and S. E. Derenzo. "Eu²⁺-doped Ba₂CsI₅, a new high-performance scintillator." *Nucl. Instrum. Meth. Phys. Res. A*, **612**[1] 138–142 (2009).
8. R. Borade, E. Bourret-Courchesne, and S. Derenzo. "Scintillation properties of CsBa₂Br₅:Eu²⁺." *Nucl. Instrum. Meth. Phys. Res. A*, **652**[1] 260–263 (2011).
9. E. Bourret-Courchesne, G. Bizarri, S. M. Hanrahan, G. Gundiah, Z. Yan, and S. E. Derenzo. "BaBrI:Eu²⁺, a new bright scintillator." *Nucl. Instr. Meth. Phys. Res. A*, **613** 95–97 (2010).
10. D. Singh. "Structure and optical properties of high light output halide scintillators." *Phys. Rev. B*, **82**[15] 155145 (2010).
11. G. Busker, A. Chroneos, R. W. Grimes, and I.-W. Chen. "Solution mechanisms for dopant oxides in yttria." *J. Am. Ceram. Soc.*, **82**[6] 1553–1559 (1999).
12. C. R. Stanek, K. J. McClellan, B. P. Uberuaga, K. E. Sickafus, M. R. Levy, and R. W. Grimes. "Determining the site preference of trivalent dopants in bixbyite sesquioxides by atomic-scale simulations." *Phys. Rev. B*, **75**[13] 134101 (2007).
13. C. R. Stanek, K. J. McClellan, M. R. Levy, and R. W. Grimes. "Extrinsic defect structure of RE₃Al₅O₁₂ garnets." *Phys. Stat. Sol. (b)*, **243**[11] R75–R77 (2006).
14. F. Maglia, V. Buscaglia, S. Gennari, P. Ghigna, M. Dapiaggi, A. Speghini, and M. Bettinelli. "Incorporation of trivalent cations in synthetic garnets A₃B₅O₁₂ (A = Y, Lu–La, B = Al, Fe, Ga)." *J. Phys. Chem. B*, **110** 6561–6568 (2006).
15. C. R. Stanek, M. R. Levy, K. J. McClellan, B. P. Uberuaga, and R. W. Grimes. "Defect identification and compensation in rare earth oxide scintillators." *Nucl. Instr. Meth. Phys. Res. B*, **266** 2657–2664 (2008).

16. L. A. Brissette, P. L. Burnett, R. M. Spriggs, and T. Vasilos. "Thermomechanically deformed Y_2O_3 ." *J. Am. Ceram. Soc.*, **49**[3] 165–166 (1966).
17. S. K. Dutta and G. E. Gazza. "Transparent Y_2O_3 by hot-pressing." *Mater. Res. Bull.*, **4**[11] 791–796 (1969).
18. C. Greskovich and J. P. Chernoch. "Polycrystalline ceramic lasers." *J. Appl. Phys.*, **44**[10] 4599–4606 (1973).
19. J. Kong, D. Y. Tang, B. Zhao, J. Lu, K. Ueda, H. Yagi, and T. Yanagitani. "9.2-W diode-end-pumped $\text{Yb}:\text{Y}_2\text{O}_3$ ceramic laser." *Appl. Phys. Lett.*, **86**[16] 161116 (2005).
20. R. A. Lefever and J. Matsko. "Transparent yttrium oxide ceramics." *Mater. Res. Bull.*, **2** 865–869 (1967).
21. R. C. Anderson and J. Barker. "Sintering of $\text{ThO}_2\text{--Y}_2\text{O}_3$." *J. Opt. Spectra*, **3** 57 (1969).
22. D. J. Sordelet and M. Akinc. "Sintering of monosized, spherical yttria powders." *J. Am. Ceram. Soc.*, **71**[12] 1148–1153 (1988).
23. I.-W. Chen and X.-H. Wang. "Sintering dense nanocrystalline ceramics without final-stage grain growth." *Nature*, **404** 168–171 (2000).
24. J. Lu, J. Lu, T. Murai, K. Takaichi, T. Uematsu, and K. Ueda. " $\text{Nd}^{3+}:\text{Y}_2\text{O}_3$ ceramic laser." *Jpn. J. Appl. Phys.*, **40** L1277–L1279 (2001).
25. R. C. Rau. "The crystal structure of Eu_3O_4 ." *Acta Cryst.*, **20** 716–723 (1966).
26. G. Concas, J. K. Dewhurst, A. Sanna, S. Sharma, and S. Massidda. "Anisotropic exchange interaction between nonmagnetic europium cations in Eu_2O_3 ." *Phys. Rev. B*, **84**[1] 014427 (2011).
27. M. Drofenik, L. Golic, and D. Kolar. " Eu_2O_3 crystal growth from the flux." *J. Cryst. Growth*, **21** 170 (1974).
28. M. W. Shafer. "Preparation and crystal chemistry of divalent europium compounds." *J. Appl. Phys.*, **36**[3] 1145–1152 (1965).
29. M. N. Rahaman. *Ceramic Processing and Sintering*, section 9.7.1.1, pages 576–578. Marcel Dekker, New York, second edition (2003).
30. K. Majima, N. Niimi, M. Watanabe, S. Katsuyama, and H. Nagai. "Effect of LiF addition on the preparation and transparency of vacuum hot pressed Y_2O_3 ." *Mater. Trans.*, **35**[9] 645–650 (1994).
31. F. F. Lange. "Sinterability of agglomerated powders." *J. Am. Ceram. Soc.*, **67**[2] 83–89 (1984).
32. M. D. Sacks and J. A. Pask. "Sintering of mullite-containing materials: II. Effect of agglomeration." *J. Am. Ceram. Soc.*, **65**[2] 70–77 (1982).
33. C. D. Greskovich, D. A. Cusano, and F. A. DiBianca. "Preparation of yttria-gadolinia ceramic scintillators by sintering and gas hot isostatic pressing." U.S. Patent 4,518,546, May 21, 1985.
34. Z. Fu, S. Zhou, T. Pan, and S. Zhang. "Preparation and luminescent properties of cubic $\text{Eu}^{3+}:\text{Y}_2\text{O}_3$ nanocrystals and comparison to bulk $\text{Eu}^{3+}:\text{Y}_2\text{O}_3$." *J. Lumin.*, **124**[2] 213–216 (2007).
35. M. Nogami, T. Yamazaki, and Y. Abe. "Fluorescence properties of Eu^{3+} and Eu^{2+} in $\text{Al}_2\text{O}_3\text{--SiO}_2$ glass." *J. Lumin.*, **78** 63–68 (1998).

36. C. Brecher, G. C. Wei, and W. H. Rhodes. "Point defects in optical ceramics: high-temperature absorption processes in lanthana-strengthened yttria." *J. Am. Ceram. Soc.*, **73**[6] 473–488 (1990).
37. T. R. N. Kutty and M. Nayak. "Photoluminescence of Eu²⁺-doped mullite prepared by a hydrothermal method." *Mater. Chem. Phys.*, **65** 158–165 (2000).
38. P. B. W. Burmester, T. Ishii, G. Huber, M. Kurfiss, and M. Schilling. "Characterization of crystalline europium doped α -Y₂O₃ PLD-films grown on α -Al₂O₃." *Mater. Sci. Eng. B*, **105** 25–29 (2003).
39. Y. Nigara. "Measurement of the optical constants of yttrium oxide." *Jpn. J. Appl. Phys.*, **7**[4] 404–408 (1968).
40. C. D. Greskovich and C. R. O'Clair. "Transparent, sintered Y_{2-x}Sr_xO_{3-x/2} ceramics." *Adv. Ceram. Mater.*, **1**[4] 350–355 (1986).
41. K. Katayama, H. Osawa, T. Akiba, and H. Yanagida. "Sintering and electrical properties of CaO-doped Y₂O₃." *J. Eur. Ceram. Soc.*, **6** 39–45 (1990).
42. J. D. McClelland and E. H. Zehms. "End-point density of hot-pressed alumina." *J. Am. Ceram. Soc.*, **46**[2] 77–80 (1962).
43. A. S. Rao and A. C. D. Chaklander. "Plastic flow during hot-pressing." *J. Am. Ceram. Soc.*, **55**[12] 596–601 (1972).
44. R. L. Coble. "A model for boundary diffusion controlled creep in polycrystalline materials." *J. Appl. Phys.*, **34**[6] 1679–1682 (1963).
45. A. S. Helle, K. E. Easterling, and M. F. Ashby. "Hot-isostatic pressing diagrams: new developments." *Acta Metall.*, **33**[12] 2163–2174 (1985).
46. P.-L. Chen and I.-W. Chen. "Grain boundary mobility in Y₂O₃: defect mechanism and dopant effects." *J. Am. Ceram. Soc.*, **79**[7] 1801–1809 (1996).
47. G. Bernard-Granger, C. Guizard, and L. San-Miguel. "Sintering behavior and optical properties of yttria." *J. Am. Ceram. Soc.*, **90**[9] 2698–2702 (2007).
48. M. N. Rahaman. *Ceramic Processing and Sintering*, section 11.7, pages 739–754. Marcel Dekker, New York, second edition (2003).
49. C. Zhang, C.-J. Li, G. Zhang, X.-J. Ning, C.-X. Li, H. Liao, and C. Coddet. "Ionic conductivity and its temperature dependence of atmospheric plasma-spray yttria stabilized zirconia electrolyte." *Mater. Sci. Eng. B*, **137** 24–30 (2007).
50. H. Yoshida, S. Hashimoto, and T. Yamamoto. "Dopant effect on grain boundary diffusivity in polycrystalline alumina." *Acta Mater.*, **53** 433–440 (2005).
51. S. R. Podowitz, R. Gaum'e, and R. S. Feigelson. "Effect of europium concentration on densification of transparent Eu:Y₂O₃ scintillator ceramics using hot pressing." *J. Am. Ceram. Soc.*, **93**[1] 82–88 (2010).
52. N. M. Tallan and R. W. Vest. "Electrical properties and defect structure of Y₂O₃." *J. Am. Ceram. Soc.*, **49**[8] 401–404 (1966).
53. R. J. Gaboriaud. "Self-diffusion of yttrium in monocrystalline yttrium oxide: Y₂O₃." *J. Solid State Chem.*, **35** 252–261 (1980).
54. G. Busker, A. Chroneos, R. W. Grimes, and I.-W. Chen. "Solution mechanisms for dopant oxides in yttria." *J. Am. Ceram. Soc.*, **82**[6] 1553–1559 (1999).
55. L. B. Anderson and D. J. Macero. "The formal reduction potential of the europium(III)–europium(II) system." *J. Phys. Chem.*, **67**[9] 1942 (1963).

56. S. J. Duclos, C. D. Greskovich, R. J. Lyons, J. S. Vartuli, D. M. Hoffman, R. J. Riedner, and M. J. Lynch. "Development of the HiLightTM scintillator for computed tomography medical imaging." *Nucl. Instr. Meth. Phys. Res. A*, **505** 68–71 (2003).
57. K. Serivalsatit and J. Ballato. "Submicrometer grain-sized transparent erbium-doped scandia ceramics." *J. Am. Ceram. Soc.*, **93**[11] 3657–3662 (2010).
58. N. J. Cherepy, S. A. Payne, J. D. Kuntz, Z. M. Seeley, F. Nessi-Tedaldi, G. Dissertori, F. Pauss, R. Wallny, and D. Luckey. "Scintillating ceramic materials for the CERN large hadron collider." Retrieved from <http://indico.cern.ch/getFile.py/access?contribId=7resId=0materialId=slidesconfId=137102>, May 11, 2011.
59. J. D. Powers and A. M. Glaeser. "Grain boundary migration in ceramics." *Interface Sci.*, **6** 23–39 (1998).
60. S. J. Dillon, S. K. Behera, and M. P. Harmer. "An experimentally quantifiable solute drag factor." *Acta Mater.*, **56**[6] 1374–1379 (2008).
61. M. S. Islam, P. R. Slater, J. R. Tolchard, and T. Dinges. "Doping and defect association in AZrO₃ (A = Ca, Ba) and LaMO₃ (M = Sc, Ga) perovskite-type ionic conductors." *Dalton Trans.*, [19] 3061–3066 (2004).
62. A. Chroneos. "Isovalent impurity-vacancy complexes in germanium." *Phys. Stat. Sol. (b)*, **244**[9] 3206–3210 (2007).
63. C. R. Stanek, M. R. Levy, K. J. McClellan, B. P. Uberuaga, and R. W. Grimes. "Defect identification and compensation in rare earth oxide scintillators." *Nucl. Instr. Meth. Phys. Res. B*, **266** 2657–2664 (2008).
64. Y. Tsur, T. D. Dunbar, and C. A. Randall. "Crystal and defect chemistry of rare earth cations in BaTiO₃." *J. Electroceram.*, **7**[1] 25–34 (2001).
65. T. O. Mason, G. B. Gonzalez, D. R. Kammler, N. Mansourian-Hadavi, and B. J. Ingram. "Defect chemistry and physical properties of transparent conducting oxides in CdO-In₂O₃-SnO₂ system." *Thin Solid Films*, **411** 106–114 (2002).
66. W. Gordy and W. J. O. Thomas. "Electronegativities of the elements." *J. Chem. Phys.*, **24**[2] 439–444 (1956).
67. J. Hinze, M. A. Whitehead, and H. H. Jaffe. "Electronegativity. II. Bond and orbital electronegativities." *J. Am. Chem. Soc.*, **85**[2] 148–154 (1963).
68. P. G. Shewmon. *Diffusion in Solids*, section 2.10, pages 81–82. McGraw-Hill, New York (1963).
69. K. Tanahashi, N. Inoue, and Y. Mizokawa. "Equilibrium concentration of vacancies under the anisotropic stress field around an impurity." *Physica B*, **308-310** 502–505 (2001).
70. A. Lempicki and R. H. Bartram. "Effect of shallow traps on scintillation." *J. Lumin.*, **81** 13–20 (1999).
71. S. Mukherjee, V. Sudarsan, R. K. Vatsa, S. V. Godbole, R. M. Kadam, U. M. Bhatta, and A. K. Tyagi. "Effect of structure, particle size and relative concentration of Eu³⁺ and Tb³⁺ ions on the luminescence properties of Eu³⁺ co-doped Y₂O₃:Tb nanoparticles." *Nanotechnol.*, **19** 325704 (2008).
72. G. R. Wagner, J. Murphy, and D. W. Feldman. "Paramagnetic resonance studies of Y₂O₃, CeO₂, and ThO₂." Aerospace Research Laboratories Report ARL 72-0026, Westinghouse Research Labs, Feb. 1972.

73. E. Zych, C. Brecher, and J. Glodo. "Kinetics of cerium emission in a YAG:Ce single crystal: the role of traps." *J. Phys.: Condens. Matter*, **12** 1947–1958 (2000).
74. J. C. Fisher. "Calculation of diffusion penetration curves for surface and grain boundary diffusion." *J. Appl. Phys.*, **22**[1] 74–77 (1951).
75. R. T. P. Whipple. "Concentration contours in grain boundary diffusion." *Philos. Mag.*, **45** 1225–1236 (1954).
76. T. Suzuoka. "Lattice and grain boundary diffusion in polycrystals." *Trans. Jpn. Inst. Met.*, **2** 25–33 (1961).
77. H. S. Levine and C. J. MacCallum. "Grain boundary and lattice diffusion in polycrystalline bodies." *J. Appl. Phys.*, **31**[3] 595–599 (1960).
78. [A. D. Le Claire. "The analysis of grain boundary diffusion measurements." *Brit. J. Appl. Phys.*, **14** 351–356 (1963).
79. J. Crank. *The Mathematics of Diffusion*. Oxford University Press (2001).
80. K. Bedu-Amissah, J. M. Rickman, H. M. Chan, and M. P. Harmer. "Impact of microstructure on grain-boundary diffusion in polycrystals." *J. Appl. Phys.*, **98**[6] 063511 (2005).
81. M. F. Berard, C. D. Wirkus, and D. R. Wilder. "Diffusion of oxygen in selected monocrystalline rare earth oxides." *J. Am. Ceram. Soc.*, **51**[11] 643–647 (1968).
82. K. Ando, Y. Oishi, H. Hase, and K. Kitazawa. "Oxygen self-diffusion in single-crystal Y_2O_3 ." *J. Am. Ceram. Soc.*, **66**[12] C222–C223 (1983).
83. N. M. Tallan and R. W. Vest. "Electrical properties and defect structure of Y_2O_3 ." *J. Am. Ceram. Soc.*, **49**[8] 401–404 (1966).
84. J. Schieltz, J. W. Patterson, and D. R. Wilder. "Electrolytic behavior of yttria." *J. Electrochem. Soc.*, **118**[7] 1140–1144 (1971).
85. V. Swamy, H. J. Seifert, and F. Aldinger. "Thermodynamic properties of Y_2O_3 phases and the yttrium–oxygen phase diagram." *J. Alloys Compd.*, **269** 201–207 (1998).
86. E. Zych, C. Brecher, A. J. Wojtowicz, and H. Lingertat. "Luminescence properties of Ce-activated YAG optical ceramic scintillator materials." *J. Lumin.*, **75** 193–203 (1997).
87. E. Mihokova, M. Nikl, J. A. Mares, A. Beitlerova, A. Vedda, K. Nejezchleb, K. Blazek, and C. D'Ambrosio. "Luminescence and scintillation properties of YAG:Ce single crystal and optical ceramics." *J. Lumin.*, **126** 77–80 (2007).
88. R. H. Bartram, A. Lempicki, L. A. Kappers, and D. S. Hamilton. "Hole traps in Lu_2O_3 :Eu ceramic scintillators. II. Radioluminescence and thermoluminescence." *J. Lumin.*, **106** 169–176 (2004).
89. S. Webb. "Applications of microscale XAS and XAS imaging." In *Structural Molecular Biology Low-Z XAS Summer School*, SLAC National Accelerator Laboratory, Menlo Park, California, July 20, 2010.
90. N. M. Haegel, T. J. Mills, M. Talmadge, C. Scandrett, C. L. Frenzen, H. Yoon, C. M. Fetzer, and R. R. King. "Direct imaging of anisotropic minority-carrier diffusion in ordered GaInP." *J. Appl. Phys.*, **105** 023711 (2009).
91. C. D. Greskovich, D. A. Cusano, and F. A. DeBianca. "Preparation of yttria-gadolinia ceramic scintillators by sintering and gas hot isostatic pressing." U.S. Patent 4,571,312, Feb. 18, 1986.

92. M. I. Peters and I. E. Reimanis. "Grain boundary grooving studies of yttrium aluminum garnet (YAG) bicrystals." *J. Am. Ceram. Soc.*, **86**[5] 870–872 (2003).
93. V. V. Nagarkar, J. S. Gordon, T. K. Gupta, S. Vasile, P. Gothoskar, M. R. Squillante, and G. Entine. "CCD-based high resolution digital radiography system for non destructive evaluation." *IEEE Trans. Nucl. Sci.*, **44**[3] 885–889 (1997).
94. B. L. Abrams and P. H. Holloway. "Role of the surface in luminescent processes." *Chem. Rev.*, **104**[12] 5783–5801 (2002).
95. M. O. Ramirez, J. Wisdom, H. Li, Y. L. Aung, J. Stitt, G. L. Messing, V. Dierolf, Z. Liu, A. Ikesue, R. L. Byer, and V. Gopalan. "Three-dimensional grain boundary spectroscopy in transparent high power ceramic laser materials." *Opt. Express*, **16**[9] 5965–5973 (2008).
96. I. Dawson, P. D. Bristowe, M.-H. Lee, M. C. Payne, M. D. Segall, and J. A. White. "First-principles study of a tilt grain boundary in rutile." *Phys. Rev. B*, **54**[19] 13727–13733 (1996).
97. S.-D. Mo, W. Y. Ching, and R. H. French. "Electronic structure of a near $\Sigma 11$ a-axis grain boundary in α - Al_2O_3 ." *J. Am. Ceram. Soc.*, **79**[3] 627–633 (1996).
98. S.-D. Mo, W. Y. Ching, M. F. Chisholm, and G. Duscher. "Electronic structure of a grain-boundary model in SrTiO_3 ." *Phys. Rev. B*, **60**[4] 2416–2424 (1999).
99. M. Kohyama, R. Yamamoto, Y. Ebata, and M. Kinoshita. "The atomic and electronic structure of a $\langle 001 \rangle$ tilt grain boundary in Si." *J. Phys. C*, **21** 3205–3215 (1988).
100. T. Kizuka, M. Iijima, and N. Tanaka. "Atomic process of electron-irradiation-induced grain boundary migration in a MgO tilt boundary." *Phil. Mag. A*, **77**[2] 413–422 (1998).
101. K. P. McKenna and A. L. Shluger. "Electron-trapping polycrystalline materials with negative electron affinity." *Nature Mater.*, **7** 859–867 (2008).
102. S. R. Podowitz, R. M. Gaume, and R. S. Feigelson. "Probing Grain Boundaries in Ceramic Scintillators using X-Ray Radioluminescence Microscopy." *J. Appl. Phys.*, **111**[1] 013520 (2012).
103. S. J. Rosner, E. C. Carr, M. J. Ludowise, G. Girolami, and H. I. Erikson. "Correlation of cathodoluminescence inhomogeneity with microstructural defects in epitaxial GaN grown by metalorganic chemical-vapor deposition." *Appl. Phys. Lett.*, **70**[4] 420–422 (1997).
104. C. D. Greskovich, D. A. Cusano, and F. A. DiBianca. "Preparation of yttria-gadolinia ceramic scintillators by sintering and gas hot isostatic pressing." U.S. Patent 4,518,546, May 21, 1985.
105. W. Shockley, G. L. Pearson, and J. R. Haynes. "Hole injection in germanium—quantitative studies and filamentary transistors." *Bell Syst. Tech. J.*, **28** 344–366 (1949).
106. V. Liuolia, S. Marcinkevičius, Y.-D. Lin, H. Ohta, S. P. DenBaars, and S. Nakamura. "Dynamics of polarized photoluminescence in m-plane InGaN/GaN quantum wells." *J. Appl. Phys.*, **108** 023101 (2010).
107. A. R. Vasconcellos, M. J. S. P. Brasil, R. Luzzi, A. A. P. Silva, and A. H. S. Leite. "Ambipolar diffusion and spatial and time-resolved spectroscopies in semiconductor heterostructures." *J. Appl. Phys.*, **106** 043503 (2009).

108. X. Liu and D. E. Aspnes. "Thickness inhomogeneities in the organometallic chemical vapor deposition of GaP." *Appl. Phys. Lett.*, **93** 203104 (2008).
109. S. Yu. Karpov and Yu. N. Makarov. "Dislocation effect on light emission efficiency in gallium nitride." *Appl. Phys. Lett.*, **81**[25] 4721–4723 (2002).
110. F. Cao, G. Oskam, G. J. Meyer, and P. C. Searson. "Electron transport in porous nanocrystalline TiO₂ photoelectrochemical cells." *J. Phys. Chem.*, **100** 17021–17027 (1996).
111. P.-T. Hsiao, Y.-L. Tung, and H. Teng. "Electron transport patterns in TiO₂ nanocrystalline films of dye-sensitized solar cells." *J. Phys. Chem. C*, **114** 6762–6769 (2010).
112. J. Bisquert. "Chemical diffusion coefficient of electrons in nanostructured semi-conductor electrodes and dye-sensitized solar cells." *J. Phys. Chem. B*, **108** 2323–2332 (2004).
113. D. R. Luber, F. M. Bradley, N. M. Haegel, M. C. Talmadge, M. P. Coleman, and T. D. Boone. "Imaging transport for the determination of minority carrier diffusion length." *Appl. Phys. Lett.*, **88** 163509 (2006).
114. M. Lax. "Junction current and luminescence near a dislocation or a surface." *J. Appl. Phys.*, **49**[5] 2796–2810 (1978).
115. M. Nikl. "Energy transfer phenomena in the luminescence of wide band-gap scintillators." *Phys. Stat. Sol. (a)*, **202**[2] 201–206 (2005).
116. [55] S. E. Derenzo, M. J. Weber, and M. K. Klintenberg. "Temperature dependence of the fast, near-band-edge scintillation from CuI, HgI₂, PbI₂, ZnO:Ga, and CdS:In." *Nucl. Instrum. Meth. Phys. Res. A*, **486** 214–219 (2002).
117. D. Drouin, A. R'éal Couture, D. Joly, X. Tastet, V. Aimez, and R. Gauvin. "CASINO V2.42—a fast and easy-to-use modeling tool for scanning electron microscopy and microanalysis users." *Scanning*, **29** 92–101 (2007).
118. K. Zhang, A. K. Pradhan, G. B. Loutts, U. N. Roy, Y. Cui, and A. Burger. "Enhanced luminescence and size effects of Y₂O₃:Eu³⁺ nanoparticles and ceramics revealed by X-rays and Raman scattering." *J. Opt. Soc. Am. B*, **21**[10] 1804–1808 (2004).
119. D. K. Williams. *Particle Size Dependence on the Luminescence Spectra of Eu³⁺:Y₂O₃ and Eu³⁺:CaO*. PhD thesis, Virginia Polytechnic Institute and State University, Blacksburg, Virginia, U.S.A., 2002.
120. D. E. Burk, S. Kanner, J. E. Muyshondt, D. S. Shaulis, and P. E. Russell. "Determination of surface recombination velocity at a grain boundary using electron-beam-induced current." *J. Appl. Phys.*, **54**[1] 169–173 (1983).
121. S. A. Bukesov and D. Y. Jeon. "Determination of recombination parameters of phosphors from cathodoluminescent characteristics." *Appl. Phys. Lett.*, **81**[12] 2184–2186 (2002).
122. Y. Rosenwaks, L. Burstein, Y. Shapira, and D. Huppert. "Effects of reactive versus unreactive metals on surface recombination velocity at CdS and CdSe(110) interfaces." *Appl. Phys. Lett.*, **57**[5] 458–460 (1990).
123. M. Passlack, M. Hong, E. F. Schubert, J. R. Kwo, J. P. Mannaerts, S. N. G. Chu, N. Moriya, and F. A. Thiel. "In situ fabricated Ga₂O₃–GaAs structures with low interface recombination velocity." *Appl. Phys. Lett.*, **66**[5] 625–627 (1995).

124. L. W. Tu, W. C. Kuo, K. H. Lee, P. H. Tsao, C. M. Lai, A. K. Chu, and J. K. Sheu. "High-dielectric-constant $\text{Ta}_2\text{O}_5/n\text{-GaN}$ metal-oxide-semiconductor structure." *Appl. Phys. Lett.*, **77**[23] 3788–3790 (2000).
125. K. P. McKenna and A. L. Shluger. "Electron-trapping polycrystalline materials with negative electron affinity." *Nature Mater.*, **7** 859–867 (2008).
126. K. McKenna and A. Shluger. "The interaction of oxygen vacancies with grain boundaries in monoclinic HfO_2 ." *Appl. Phys. Lett.*, **95** 222111 (2009).
127. A. L. Shluger, K. P. McKenna, P. V. Sushko, D. Muñoz Ramo, and A. V. Kimmel. "Modelling of electron and hole trapping in oxides." *Modeling Simul. Mater. Sci. Eng.*, **17** 084004 (2009).
128. S. Siebentritt, M. Igalson, C. Persson, and S. Lany. "The electronic structure of chalcopyrites—bands, point defects and grain boundaries." *Prog. Photovolt: Res. Appl.*, **18** 390–410 (2010).
129. I. Warshaw and R. Roy. "Polymorphism of the rare earth sesquioxides." *J. Phys. Chem.*, **65** 2048–2051 (1961).
130. A. V. Shevchenko, B.S. Nigmanov, Z.A. Zaitseva, and L.M. Lopato. "Interaction of samarium and gadolinium oxides with yttrium oxide." *Russ. J. Inorg. Chem. (Engl. Trans.)*, **22**[5] 681–685 (1986).
131. R. J. Brook. "Pore-grain boundary interactions and grain growth." *J. Am. Ceram. Soc.*, **52**[1] 56–57 (1969).
132. V.S. Venkataramani *et al.*, SCINT conference (2002).
133. L. N. Komissarova, W. K. Shih, and V. I. Spitsyn. "Reaction of hafnium hydroxide with the hydroxides of yttrium, lanthanum, neodymium and ytterbium." *Izvestiya Akademii Nauk SSSR, Seriya Khimicheskaya*, **1** 3–11 (1965).
134. S. V. Ushakov and A. Navrotsky. "Energetics of defect fluorite and pyrochlore phases in lanthanum and gadolinium hafnates." *J. Am. Ceram. Soc.*, **90** [4] 1171–1176 (2007).
135. A.V. Shevchenko, L.M. Lopato, and Z.A. Zaitseva. "Reactions of HfO_2 with lanthana, preaeodymia and neodymia at high temperatures." *Izv. Akad. Nauk SSSR, Neorg. Mater.*, **20** [9], 1530–1534 (1984).
136. G. Blasse, W. Schipper, and J. J. Hamelink. "On the Quenching of the Luminescence of the Trivalent Cerium Ion." *Inorg. Chim. Acta.*, **189** 77–80 (1991).
137. E. V. Van Loef, Y. Wang, J. Glodo, C. Brecher, A. Lempicki, and K. S. Shah. "Recent Advances in Ceramic Scintillators." *Mater. Res. Soc. Symp. Proc.*, **1038** 006–02 (2007).
138. A. P. Patel, M. R. Levy, R. W. Grimes, R. M. Gaume, R. S. Feigelson, K. J. McClellan, and C. R. Stanek. "Mechanisms of nonstoichiometry in $\text{Y}_3\text{Al}_5\text{O}_{12}$." *Appl. Phys. Lett.*, **93** 191902 (2008).
139. A. J. Stevenson, X. Li, M. A. Martinez, J. M. Anderson, D. L. Suchy, E. R. Kupp, E. C. Dickey, K. T. Mueller, and G. L. Messing. "Effect of SiO_2 on densification and microstructure development in Nd:YAG transparent ceramics." *J. Am. Ceram. Soc.*, **94**[5] 1380–1387 (2011).
140. K. Mori. "Transient colour centres caused by UV light irradiation in yttrium aluminum garnet crystals." *Phys. Stat. Sol. (a)*, **42**[1] 375–384 (1977).

141. V. Babin, K. Blazek, A. Krasnikov, K. Nejezchleb, M. Nikl, T. Savikhina, and S. Zazubovich. "Luminescence of undoped LuAG and YAG crystals." *Phys. Stat. Sol. (c)*, **2**[1] 97–100 (2005).
142. Y. Zorenko. "Luminescence of isoelectronic impurities and antisite defects in garnets." *Phys. Stat. Sol. (c)*, **2**[1] 375–379 (2005).
143. M. Nikl, J. A. Mares, N. Solovieva, H.-L. Li, X.-J. Liu, L.P.Huang, I. Fontana, M. Fasoli, A. Vedda, and C. D'Ambrosio. "Scintillation characteristics of $\text{Lu}_3\text{Al}_5\text{O}_{12}:\text{Ce}$ optical ceramics." *J. Appl. Phys.*, **101**[3] 033515 (2007).
144. N. J. Cherepy, J. D. Kuntz, T. M. Tillotson, D. T. Speaks, S. A. Payne, B. H. T. Chai, Y. Porter-Chapman, and S. E. Derenzo. "Cerium-doped single crystal and transparent ceramic lutetium aluminum garnet scintillators." *Nucl. Instr. and Meth. Phys. Res. A*, **579** 38–41 (2007).
145. L. A. Davis and R. B. Gordon. "Plastic deformation of alkali halide crystals at high pressure: Work-hardening effects." *J. Appl. Phys.*, **40**[11] 4507–4513 (1969).
146. W. Skrotzki and P. Welch. "Development of texture and microstructure in extruded ionic polycrystalline aggregates." *Tectonophysics*, **99** 47–61 (1983).
147. P. Yang, T. J. Boyle, N. S. Bell, M. R. Sanchez, L. A. M. Ottley, and C. F. Chen. "Fabrication of large-volume, low-cost ceramic lanthanum halide scintillators for gamma ray detection." Sandia Report SAND2008-6978, Sandia National Laboratories, Oct. 2008.
148. R. Apetz and M. P. B. van Bruggen. "Transparent alumina: A light-scattering model." *J. Am. Ceram. Soc.*, **86**[3] 480–486 (2003).
149. C. V. Raman and K. S. Viswanathan. "The theory of the propagation of light in polycrystalline media." *Proc. Indian Acad. Sci.*, **A41** 37–44 (1955).
150. M. D. Julian and F. Luty. "Light scattering and infrared-transmission spike in multidomain birefringent solids (KCN and NaCN)." *Phys. Rev. B*, **21**[4] 1647–1652 (1980).
151. C. W. Wilson, E. V. van Loef, J. Glodo, N. Cherepy, G. Hull, S. Payne, W.-S. Choong, W. Moses, and K. S. Shah. "Strontium iodide scintillators for high energy resolution gamma ray spectroscopy." *Proc. of SPIE*, **7079** 7079171–7079177 (2008).
152. N. J. Cherepy, G. Hull, A. D. Drobshoff, S. A. Payne, E. van Loef, C. M. Wilson, K. S. Shah, U. N. Roy, A. Burger, L. A. Boatner, W.-S. Choong, and W. W. Moses. "Strontium and barium iodide high light yield scintillators." *Appl. Phys. Lett.*, **92**[8] 35081–35083 (2008).
153. Y. Chen, M. M. Abraham, T. J. Turner, and C. M. Nelson. "Luminescence in deformed MgO, CaO, and SrO." *Philos. Mag.*, **32**[1] 99–112 (1975).
154. S. E. Derenzo, W. W. Moses, J. L. Cahoon, T. A. DeVol, and L. Boatner. "X-ray fluorescence measurements of 412 inorganic compounds." *Proc. Nucl. Sci. Symp. Med. Imag. Conf.*, **1** 143–147 (1991).
155. L. Ahle, G. Bizarri, L. Boatner, N. J. Cherepy, W.-S. Choong, W. W. Moses, S. A. Payne, K. Shah, S. Sheets, and B. W. Sturm. "Studies of non-proportionality in alkali halide and strontium iodide scintillators using SLYNCI." *Mater. Res. Soc. Symp. Proc.*, **1164** 1164–L07–04 (2009).

**DISTRIBUTION LIST
DTRA-TR-13-7**

DEPARTMENT OF DEFENSE

DEFENSE TECHNICAL
INFORMATION CENTER
8725 JOHN J. KINGMAN ROAD,
SUITE 0944
FT. BELVOIR, VA 22060-6201
ATTN: DTIC/OCA

DEFENSE THREAT REDUCTION
AGENCY
8725 JOHN J. KINGMAN ROAD
STOP 6201
FT. BELVOIR, VA 22060-6201
ATTN: D. PETERSEN

**DEPARTMENT OF DEFENSE
CONTRACTORS**

EXELIS, INC.
1680 TEXAS STREET, SE
KIRTLAND AFB, NM 87117-5669
ATTN: DTRIAC